Theoretical and Experimental Investigation of Particle Interactions in Pharmaceutical Powder Blending

Yu Pu

B.S. Chemical Engineering
Tsinghua University, 1999

M.S. Chemical Engineering
Tsinghua University, 2002

M.S. Chemical Engineering Practice
Massachusetts Institute of Technology, 2005

Submitted to the Department of Chemical Engineering
in Partial Fulfillment of the Requirements for the Degree of
Doctor of Philosophy in Chemical Engineering
at the
Massachusetts Institute of Technology

April 12, 2007
[June 2007]

Author: .....
Yu Pu
Department of Chemical Engineering
April 12, 2007

Certified by: .....
Charles L. Cooney
Professor of Chemical and Biochemical Engineering
Thesis supervisor

Accepted by: .....
William Deen
Chairman, Committee for Graduate Students

Theoretical and Experimental Investigation of Particle Interactions in Pharmaceutical Powder Blending

Yu Pu

Submitted to the Department of Chemical Engineering on April 12, 2007
in Partial Fulfillment of the Requirements for
the Degree of Doctor of Philosophy in Chemical Engineering

Abstract

In pharmaceutical manufacturing practices, blending of active pharmaceutical ingredient (API) with excipients is a crucial step in that homogeneity of active ingredient after blending is a key issue for the quality assurance of final products. Inadequate knowledge of the interdependence between raw material properties and their impact on the blending process often gives rise to product variance and failure and therefore higher manufacturing costs. Since particles are the basic unit of powder flow, a fundamental understanding of the crucial particle characteristics and particle interactions is essential for a good prediction and control of the blending process.

In this work, inter-particle adhesion forces including van der Waals force, capillary force and electrostatic force of lactose monohydrate and microcrystalline cellulose were measured by the atomic force microcopy and other techniques. Their correlations with particle properties and environmental variables were elucidated quantitatively through mathematical modeling, and their impacts on powder blending homogeneity were investigated experimentally. It was found that surface roughness, electrostatic surface charges, moisture sensitivity as well as relative humidity are crucial parameters to determine inter-particle adhesion forces. By controlling these factors, the inter-particle adhesion forces can be optimized to improve final blend homogeneity. For instance, using excipient particles processed with surface-smoothing method reduced the blending time to reach endpoint. It was also found that enhancing electrostatic attractive interactions between excipient and API particles resulted in better blend homogeneity. In addition, the mathematical force models developed in this study allowed us to predict the magnitudes of inter-particle adhesion forces, which can be later used as an important input parameter in simulating the powder blending process of different scales.

The mechanistic knowledge of particle interactions and their dependence on particle properties through this study provides a theoretical foundation for a successful linkage between the micro-scale particle level and the macro-scale bulk powder flow behavior, enhances process understanding, and opens opportunities for process improvement.

Thesis Supervisor: Charles L. Cooney
Title: Professor of Chemical & Biochemical Engineering

Acknowledgement

If time, like an old Chinese proverb saying, eclipses like a wide river flowing rapidly ahead day and night without stop, I would see myself as a sailor traveling along the water from one land to another. The past five years I spent at MIT is only a short period in my whole lifetime, however, it left me with so many valuable and unforgettable memories which I would treasure for my life. Here I would like to take the opportunity to extend my gratitude to the people who shared with me all my tears and laughter, my success and failure, and my dreams and hopes over these years. Without them, my journey would not have been so enjoyable and achievable.

First and foremost, I would like to thank my thesis advisor, Professor Charles Cooney. It is he who led me into the world of pharmaceutical manufacturing science, a challenging and exciting field which I am very passionate about. He has been a great mentor not only in supporting and guiding my research, but also in encouraging and instructing me to improve my communication skills and to broaden my horizons in my career development. His good sense of humor and kindness brought a lot pleasure to my stressful and tedious research work.

I would also like to thank my collaborators, Professor Christine Ortiz, for letting me use the atomic force microscopy in her lab and giving me many useful recommendations, and Professor Malay Mazumder, for offering me great help in electrostatic charging apparatus setup and all the constructive discussions. The other two of my thesis committee members, Professor Patrick Doyle and Professor Alan Hatton, also provided me with many comments and suggestions which kept my research on the right track.

I am especially grateful for the help and friendship of my labmates, Reuben Domike, Samuel Ngai, Mridula Pore, Lakshman Pernenkil, Daniel Weber, Steven Hu, Brian Mickus, Matt Abel and Erin Bell. I learned a lot from them and my lab life was made more interesting by working with them.

During my research, I received a lot of help and support from many other sources. They include: Steven Kooi of the Institute of Soldier Nanotechnology, John Tedesco of the Veeco Inc., Maciej Noras of the Trek Inc., Patrick Boisvert and Tim McClure of the MIT Center for Materials Science and Engineering, and Andrew Gallant and Peter Morley of the MIT Central Machine Shop. Their expertise in instrumentation saved me from struggling in the lab desperately. Also I would like to acknowledge the financial support from the Consortium for the Advancement of Manufacturing of Pharmaceuticals (CAMP) as well as the discussions and communications from Dr. San Kiang of Bristol-Myers Squibb.

Finally, I would like to dedicate my thesis to my parents and my sister. Their love and trust has given me strength to conquer the barriers and difficulties I met in my life. It is the greatest regret for me that I could not go back home to attend my father's funeral during my PhD study in US. I wish that he could be comforted by the accomplishment of my thesis and be proud of my achievement. Thanks to my husband Weimin for his patience in teaching me the statistical analysis software tools, for helping me go through my father's death, and for his love and encouragement all along.

TABLE OF CONTENTS

1 INTRODUCTION 11

1.1 MOTIVATION 11
1.2 BACKGROUND 13
1.2.1 Powder blending theory 13
1.2.2 Particle interaction force and its measurement 15
1.3 OBJECTIVES 17
1.4 RESEARCH METHODOLOGY 17
1.5 REFERENCES 18

2 MEASUREMENT AND MODELING OF INTER-PARTICLE VAN DER WAALS FORCE 20

2.1 INTRODUCTION 20
2.2 CHARACTERIZATION OF PARTICLE SURFACE MORPHOLOGIES 22
2.2.1 Qualitative description of particle surface morphology by ESEM 22
2.2.2 Quantitative description of particle surface roughness by AFM 24
2.3 MEASUREMENT OF INTER-PARTICLE VAN DER WAALS FORCE 29
2.3.1 Tip and sample preparation 29
2.3.2 Force measurement by the AFM 30
2.4 MODELING OF INTER-PARTICLE VAN DER WAALS FORCE 32
2.4.1 Simulation of particle surfaces with defined roughness 33
2.4.2 Calculation of van der Waals force by surface element integration method 36
2.5 RESULTS 39
2.5.1 Comparison between the calculated and the measured van der Waals force 39
2.5.2 Parametric study based on the modeling results 43
2.6 DISCUSSIONS 47
2.7 REFERENCES 49

3 ELECTROSTATIC FORCE 51

3.1 INTRODUCTION 51
3.2 MEASUREMENT OF SURFACE CHARGE AND CHARGE DISTRIBUTION 54
3.2.1 Charge measurement on bulk powders 55
3.2.2 Charge measurement on single particles 57
3.3 MEASUREMENT OF INTER-PARTICLE ELECTROSTATIC FORCE 59
3.4 MODELING OF INTER-PARTICLE ELECTROSTATIC FORCE 61
3.4.1 Introduction 61
3.4.2 Modeling of electrostatic force between two dielectric particles 63
3.4.3 Results and discussion of the electrostatic force modeling 66
3.5 DISCUSSIONS 69
3.6 REFERENCES 70

4 CAPILLARY FORCE 73

4.1 INTRODUCTION 73
4.2 HYGROSCOPICITY CHARACTERIZATION OF EXCIPIENT POWDERS 74
4.3 MEASUREMENT OF INTER-PARTICLE CAPILLARY FORCE 76
4.3.1 Experimental 76
4.3.2 Results 76
4.3.3 Discussions 79
4.4 MODELING OF INTER-PARTICLE CAPILLARY FORCE 80
4.4.1 Theory of capillary force 80

4.4.2 Capillary force model for two interacting spheres with surface roughness 83
4.4.3 Sensitivity of capillary force to the surface contact geometry 87
4.5 SUMMARY 91
4.6 REFERENCES 92

5 RELATIVE IMPORTANCE OF INTER-PARTICLE VAN DER WAALS FORCE, CAPILLARY FORCE AND ELECTROSTATIC FORCE 94

5.1 COMPARISON OF THE MAGNITUDE OF THEORETICAL INTER-PARTICLE FORCE 94
5.2 COMPARISON OF THE MAGNITUDE OF EXPERIMENTALLY MEASURED INTER-PARTICLE FORCES 96
5.3 REFERENCES 99

6 EFFECT OF SURFACE ROUGHNESS ON POWDER BLENDING PROCESS 100

6.1 INTRODUCTION 100
6.2 EXPERIMENTAL 100
6.2.1 Surface treatment of lactose particles 100
6.2.2 Surface characterization of lactose particles 101
6.2.3 Measurement of inter-particle adhesion force 101
6.2.4 On-line monitoring of blending kinetics of lactose-caffeine system 101
6.3 RESULTS AND DISCUSSIONS 102
6.3.1 Surface modification of lactose particles 102
6.3.2 Evaluation of inter-particle adhesion force 105
6.3.3 Evaluation of blending performance of lactose-caffeine system 106
6.4 SUMMARY 108
6.5 REFERENCES 108

7 EFFECT OF ELECTROSTATIC FORCE ON POWDER BLENDING PROCESS 110

7.1 INTRODUCTION 110
7.2 EXPERIMENTAL 111
7.2.1 Blending process with uncontrolled electrostatic charges 111
7.2.2 Blending process with electrostatic charge neutralization 112
7.2.3 Blending process with controlled corona charging 113
7.3 RESULTS 116
7.3.1 Blending homogeneity with uncontrolled electrostatic charges 116
7.3.2 Blending homogeneity with electrostatic charge neutralization 119
7.3.3 Blending homogeneity with electrostatic corona charging 121
7.4 DISCUSSIONS 124
7.5 REFERENCES 125

8 EFFECT OF RELATIVE HUMIDITY ON POWDER BLENDING PROCESS 127

8.1 INTRODUCTION 127
8.2 EXPERIMENTAL 127
8.2.1 Characterization of moisture sensitivity of particles 127
8.2.2 Blending with relative humidity control 128
8.3 RESULTS AND DISCUSSION 128
8.3.1 Moisture sensitivity of lactose and MCC 128
8.3.2 Blend homogeneity at different relative humidity level 131
8.4 REFERENCES 132

9 CONCLUSION AND IMPACT 133

9.1 CONCLUSION 133
9.2 IMPACT 135

10 FUTURE WORK 136

10.1 SUGGESTED WORK IN PARTICLE CHARACTERIZATION 136
10.2 SUGGESTED WORK IN INTER-PARTICLE FORCE MEASUREMENT 137
10.3 SUGGESTED WORK IN FORCE MODELING 137
10.4 SUGGESTED WORK IN INNOVATION OF BLENDING PROCESS 138

11 APPENDIX: AN EXAMPLE ON THE APPLICATION OF THE MATERIAL CHARACTERIZATION IN INDUSTRIAL PRACTICE 140

LIST OF FIGURES

Figure 1-1 Illustration of relationship between particle properties, ... 12
Figure 1-2 Schematic of research methodology framework 18
Figure 2-1 A Schematic of Rumpf's model for the interaction between a particle and a rough surface 21
Figure 2-2 ESEM pictures of MCC particles: (a) Celphere®; (b) Avicel® 23
Figure 2-3 ESEM pictures of a single particle of: (a) glass bead; (b) polystyrene bead; (c) MCC; (d) lactose 24
Figure 2-4 AFM height images of a lactose particle: 25
Figure 2-5 AFM 3-D surface image of (a) glass bead ; (b) polystyrene bead ; (c) MCC particle ; (d) lactose particle 27
Figure 2-6 Height contour of a scanned lactose particle surface 28
Figure 2-7 ESEM pictures of a single lactose particle (left) and a single MCC particle (right) 29
Figure 2-8 Typical approach and retract force curves between a single lactose particle and another lactose particle adhered on a silicon nitride cantilever, drawn: (a) directly from the AFM raw data regarding the tip deflection (LSB) of all the 128 data pointed collected on one single scan line; (b) from the converted data regarding the actual inter-particle force (nN) variation with the tip-to-sample distance (nm)..... 31
Figure 2-9 Surface images of: (a) actual lactose particle surface; (b) simulated particle surface; 35
Figure 2-10 Illustration of two simulated particle surfaces getting into contact 35
Figure 2-11 Schematic of surface element segmentation between two rough surfaces 36
Figure 2-12 Comparison between calculated vdW force and experimental data: 41
Figure 2-13 Comparison between the experimental data and 42
Figure 2-14 Calculated vdW force vs. particle diameter 44
Figure 2-15 Calculated vdW force vs. asperity diameter 44
Figure 2-16 Calculated vdW force vs. asperity height 45
Figure 2-17 Calculated vdW force vs. standard deviation of asperity height 45
Figure 2-18 Calculated vdW force vs. Hamaker constant 46
Figure 2-19 Calculated vdW force vs. fractional coverage of asperities 46
Figure 2-20 Calculated vdW force vs. radius of contact area 47
Figure 3-1 Electrostatic charge build-up with the blending time for lactose particles 56
Figure 3-2 Electrostatic charge build-up with the blending time for MCC particles 56
Figure 3-3 The height image (top) and the surface potential image (bottom) 59
Figure 3-4 AFM Force curve of a lactose particle carrying surface charges brought into contact with another single lactose particle adhered on the silicon nitride cantilever 61
Figure 3-5 Schematic of point charge method between two dielectric spheres 64
Figure 3-6 AFM approach force curve fitted by the electrostatic force model 66
Figure 3-7 Electrostatic charge distribution over the scan area of particle surface 69
Figure 3-8 Surface map of cohesion force distribution (left) and charge distribution (right) .. 69
Figure 4-1 Dynamic vapor sorption curve: (a) lactose DCL11; (b) MCC particles 75
Figure 4-2 Cohesion force variation with the relative humidity for different lactose particles 78
Figure 4-3 Cohesion force variation with the relative humidity for different MCC particles . 78

Figure 4-4 The cohesion behaviors corresponding to three scenarios of surface contact geometry[20] 79
Figure 4-5 Illustration of liquid bridge growth with the elevated relative humidity 80
Figure 4-6 Schematic of sphere-substrate contact with liquid meniscus present 81
Figure 4-7 Radius of liquid meniscus as a function of relative humidity 83
Figure 4-8 Schematic illustration of the model for capillary force between two asperities 84
Figure 4-9 Comparison between the experimental and theoretical capillary forces of lactose particles 86
Figure 4-10 Surface contact geometry of hemispherical asperites 87
Figure 4-11 Capillary force vs. Relative humidity for spherical asperity contact 88
Figure 4-12 Surface contact geometry of asperities with boundary function $y=px^m$ and the corresponding capillary force profile: (a1-a2) p=0.4, m=1; (b1-b2) p=500, m=1.5; 90
Figure 5-1 Comparison of the magnitude of theoretical inter-particle forces for single-point contact between equal spheres in air (dashed lines indicate asperity-to-plane contact) [2] 95
Figure 5-2 Sketch of relative important between van der Waals force, capillary force 98
Figure 6-1 Configuration of lab-scale V-type blender 102
Figure 6-2 X-ray powder diffraction spectrum of lactose particles (from top to bottom: unprocessed, processed for 10 min, processed for 20 min and processed for 30 min) 103
Figure 6-3 RMS frequency distribution of unprocessed and processed lactose particles 104
Figure 6-4 ESEM pictures of surface morphologies of lactose particles 104
Figure 6-5 Cohesion/adhesion force for unprocessed and processed lactose particles 105
Figure 6-6 Blending kinetic curves of unprocessed and processed lactose mixed with caffeine 107
Figure 7-1 Schematic of rotating blender with ionized air flowing through 112
Figure 7-2 Experiment setup for the blending with charge neutralization 113
Figure 7-3 Schematic of corona charging apparatus 114
Figure 7-4 Experimental setup of corona charging 115
Figure 7-5 Concentration variation for lactose-caffeine blend with different charge-to-mass ratio (a) 2 wt% caffeine in blend; (b) 5 wt% caffeine in blend; (c) 10 wt% caffeine in blend 117
Figure 7-6 Average concentration variation vs. Average charge-to-mass ratio 118
Figure 7-7 Concentration variation vs. Charge-to-mass ratio for three different blend system 118
Figure 7-8 API concentration variation distribution of blending with and without charge neutralization: (a) 2% caffeine with lactose; (b) 5% caffeine with lactose; (c) 10% caffeine with lactose 120
Figure 7-9 Comparison of blend homogeneity between blending with and without charge neutralization 121
Figure 7-10 Comparison of API concentration variation between blending with and without charge control: (a) 2% caffeine blending with lactose; (b) 5% caffeine blending with lactose; 123
Figure 8-1 Surface morphologies of lactose at different relative humidity levels under ESEM 129

Figure 8-2 Surface morphologies of MCC at different relative humidity levels under ESEM 130
Figure 8-3 Effect of relative humidity on the blend homogeneity for lactose blending with 2 wt% caffeine 131
Figure 8-4 Effect of relative humidity on the blend homogeneity, ... 132
Figure 11-1 ESEM pictures of three types of BMS sample particles 141
Figure 11-2 Cumulative frequency distribution of particle cohesion forces for BMS Sample A, B and C 142

LIST OF TABLES

Table 2-1 Typical parameters characterizing the particle surface morphology 28
Table 2-2 Hamaker constant of different materials 37
Table 2-3 Young's modulus and poisson ratio of different materials 38
Table 3-1 Dielectric constants of materials used in research 53
Table 5-1 Comparison of the magnitude of the vdW and capillary forces at RH=45% 98
Table 6-1 *p* value of statistical T-test for lactose-lactose cohesion force data 106
Table 6-2 *p* value of statistical T-test for lactose-caffeine adhesion force data 106
Table 6-3 *p* value of statistical T-test for time of blend homogeneity of lactose-caffeine system 107
Table 6-4 Surface roughness, cohesion/adhesion force and the time required 108

1 Introduction

1.1 Motivation

Pharmaceutical manufacturing processes consist of a series of unit operations. In direct-compression formulation of drug products, dry blending of active pharmaceutical ingredient (API) with excipients is a crucial step in that homogeneity of active distribution after blending is a key issue for the quality assurance of final products. Since 1993, a series of rules have been set out to regulate the sampling and homogeneity of pharmaceutical blend[1]. However, due to the fact that the drug substance and excipients rarely demonstrate comparable particle properties, the existing theory and mechanism of powder mixing has only limited applications to various pharmaceutical systems. Most powder blending processes in industrial practices are still based on trial-and-error and empirical approaches. In a recent report[2], lack of adequate potency and/or content uniformity was cited as the primary reason for the recall of solid dosage forms.

In fact, in pharmaceutical manufacturing practices, inadequate knowledge of the interdependence between the raw material properties and their impact on the process performance often gives rise to product failure and therefore longer time to market and higher manufacturing cost. The importance of identifying and understanding relevant multi-factorial relationships among material, manufacturing process, and environmental variables and their effects on product quality was emphasized in the Process Analytical Technology (PAT) initiative launched by the Food and Drug Administration (FDA) in 2004. It is also encouraged by the FDA that in the future state of pharmaceutical manufacturing product and process specifications are based on a mechanistic understanding of how formulation and process factors affect product performance[3].

Since particles are the basic unit of powder flow, and the dry powder blending process is essentially mutual interactions between numerous fine particles from a microscopic perspective, a fundamental understanding of the crucial physical and chemical properties of

individual particles and their mutual interactions is critical for a good prediction and control of the blending process. It has been confirmed in Domike and Ngai's work[4, 5] that, the microscopic particle cohesion and friction interactions have close relationship with the macroscopic bulk powder behaviors such as flowability and compressibility. It also showed that, with particle cohesion and friction data as the main input parameters, the blending kinetics can be simulated computationally. One limitation of their work, though, is that the force data was purely obtained by experimentally measuring a small number of particles without identifying the corresponding particle properties. The limited sample size is insufficient to represent the whole particle population.

It is believed that a profound exploration of the mechanism of particle interactions and their dependence on particle properties will provide a theoretical foundation for a successful linkage between the micro-scale particle level and the macro-scale process performance. The gained mechanistic knowledge can be applied to enhance process understanding and facilitate formulation and process design. Figure 1-1 illustrates the big picture of this research work.

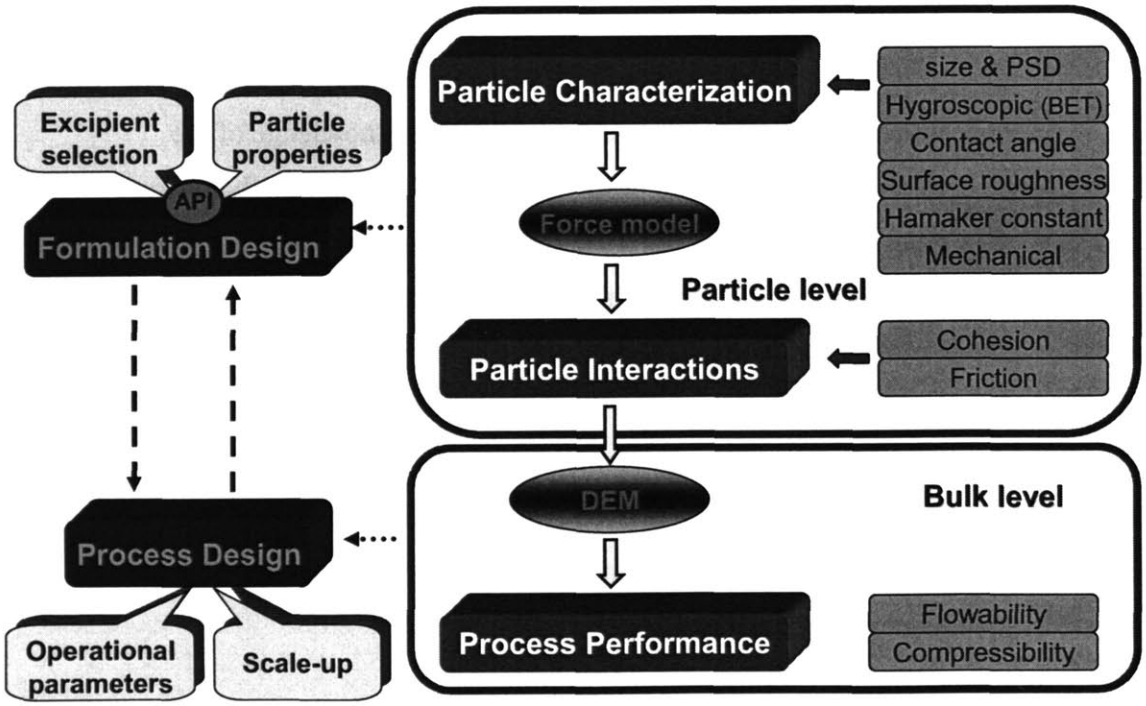

Figure 1-1 Illustration of relationship between particle properties, particle interactions and process performance

1.2 Background

1.2.1 Powder blending theory

Powder blending phenomena have been extensively studied for decades. In early times, the study was mainly focused on non-cohesive particulate system. The concept of *randomized mixing* was put forward for the operation which was carried out with particles of the same material, with identical size, shape, surface texture and no interaction between the particles or between the particles and the container[6], for example, mixing of particles of sand or glass beads, distinguished only by color. Hogg[7] has described the kinetics of the mixing process of two identical powders using the equation of diffusion. In such a system, there will be an equal probability of a particle of either ingredient being found at any particular position in the mixture.

Other than the non-cohesive randomized mixing, the performance of a powder composed of fine particles is often determined by the relative importance of the inter-particle forces to the gravitational forces acting upon the interacting particles. Because of these attraction forces, fine particles are highly sticky, cohesive and have poor flowabilily, resulting in poor particle mobility and a powder with high structural strength which increases with compaction. The bulk flow in this case is described as cohesive or 'stick-slip' flow[6]. When inter-particle forces of either attraction or repulsion are introduced within the mixtures, the mixing of cohesive powders becomes complex and cannot be explained fully by simple random mixing theory. This type of mixing is best described by *ordered mixing*[6]. The rate of ordered mixing follows first-order kinetics, since the rate of mixing is proportional to the number of fine particles remaining to adhere onto the larger particles. For a given particulate system, the rate of mixing will be proportional to the concentration of unmixed fine particles[8]. Ordered systems can only be achieved in the case of 'ordered adhesion' where an identical number of mono-sized fine particles must adhere to each individual particle of a mono-sized carrier. In some literature it is suggested that particles below 100 μm are nearly always cohesive; particles above 400 μm are generally free-flowing. The presence of particles of less than 100 μm in a wide distribution of particles of larger sizes may make the whole powder cohesive[9].

The quality of a mixture is usually measured by the standard deviation of the concentration of some constituent in the mixture. In a randomized mixing, the mixing homogeneity will obey the laws of probability and will be governed by the pure statistical distribution of the components. The theoretical standard deviation σ_R can be calculated as[10]:

$$\sigma_R = \sqrt{\frac{X(1-X)}{n}} \tag{1.2-1}$$

where X is the proportion of one ingredient and n is the total number of particles in the blend. Traditionally the terms *ordered* ($\sigma<\sigma_R$), *random* (($\sigma=\sigma_R$) and *incomplete* ($\sigma>\sigma_R$) are in use to define the level of homogeneity[11]. For a mixture formed by adhesion of cohesive fine particles to coarser carrier particles, the sample standard deviation s is the method of choice used as a measure of the mixture's homogeneity, expressed as[12]:

$$s = \sqrt{\frac{\sum(X_i - \overline{X})^2}{n-1}} \tag{1.2-2}$$

where X_i is the concentration of the minor component in each of the n spot samples taken from the mixture and $\overline{X}$ is the average of all X_i values. Sometimes the coefficient of variation ($s/\overline{X}$) is also used to investigate the mixture's homogeneity of cohesive powders.

In industry the specification for the required state of mixing consists of a sample size (scale of scrutiny), limits on the percentage of the component present in the samples and the frequency with which samples must lie within these limits. The means is by taking samples from various spots in the assembly, assaying these, and judging the degree of mixing by way of comparing the results with the theoretical mean, x, of the mixture, and the standard deviation[13]. For a particular product, a 'scale of scrutiny' is defined as "that maximum size of regions of segregation in the mixture which would cause it to be regarded as imperfectly mixed"[14]. It fixes the scale of the sample size at which the mixture should be examined. In pharmaceutical industry, the sample size should be comparable to a dosage unit (e.g. the weight of a tablet). In examining the quality of a mixture by extracting samples the reliability of the result depends on the number of samples taken. The larger the number of samples the better the estimate. From a statistical point of view, the number of samples should be no less than 20, preferably 30[10]. Another important point is the selection of the point at which samples are collected. In some cases segregation takes place in emptying a mixer or in the subsequent

handling of the mixture. In industry the interest is in the quality of the mixture leaving the mixer, and in general samples should be obtained from the outlet stream[15].

The degree of homogeneity required for pharmaceutical final blend has been underlined in a court decision, *United States vs. Barr Laboratories*, known as the Barr Decision. Assuming the distribution of tablet contents to be normal, then content variations of all (or 99.7%, using the 3× standard deviation level) individual samples should lie within ten percent of the desired composition[16].

1.2.2 Particle interaction force and its measurement

Unlike free-flowing systems, the excipients and active particulate ingredients used in drug solid dosage forms are mostly on the scale of microns, cohesive powders. Particles interact with each other throughout all the powder handling process from comminution, through mixing and compaction, to storage, due to the ubiquitous attraction and/or repulsion forces. Particle interactions can be broadly classified into two classes, namely cohesive and adhesive. Cohesion usually refers to interactions between particles of the same chemical structure and of similar particle size, whereas adhesion refers to interactions between particles of different materials[6]. Either cohesion or adhesion becomes significant when the dimensions of the pharmaceutical powders are small enough that the gravitational forces acting upon these particles are negligible. For the sake of simplicity, these two types of interactions are not distinguished strictly in this paper. Inter-particle frictional interaction, although playing an important role in particle movement, is usually a function of cohesion force and will not be addressed here.

Bulk powder properties, such as flowability, mixing, aggregation, dispersion, compression and drug dissolution, are affected by the particle-particle interaction between solids. Due to its importance, research on particle cohesion interaction has drawn more and more attention in recent years. Various techniques have been developed and applied in the particle cohesion measurements. For instance, centrifugal detachment and electrical field detachment[17] characterized cohesive force distribution of bulk powders with the aid of centrifugal forces or electric fields; Vibration method[18] was applied to quantify the cohesive forces between a

particle and a vertical vibrating wall; and direct separation method[19] was used to measure the cohesive force between single particles with a resolution of approximately 2 nN.

Compared to the methods mentioned above, the atomic force microscope (AFM) is a more powerful tool to investigate the interactions between individual particles. It has been widely used in pharmaceutical research by virtue of its ability to determine high-resolution surface morphology and to sense intermolecular forces with high sensitivity. In such experiments the deflection of an AFM cantilever is recorded as it approaches and retracts from the surface. With knowledge of the cantilever stiffness, cantilever deflections can be converted to force data using Hooke's law. This allows the cohesion forces to be determined.

AFM was used to investigate the interaction forces between individual particles qualitatively as well as quantitatively, e.g. cohesion force between two single silica aerogel powder particles[20], or between a single particle of crystalline lactose and a tablet of lactose[21]. It has also been applied in the dry powder inhaler (DPI) studies to measure the interaction between a lactose (carrier) particle and a zanamivir (drug) crystal[22], and between a drug particle and a substrate of different materials[23]. The measured inter-particle forces are generally in the magnitude of nanonewtons.

Generally speaking, particle cohesion force consists of three force components: van der Waals force, capillary force and electrostatic force. Several theories have been developed to describe each force component. However, most of them are based on the model of ideal smooth surfaces and failed to be extended to pharmaceutical particle system. In addition, although previous studies provided valuable information of the magnitudes of forces between micron-sized particles, none of them discussed systematically the factors which affect the cohesion forces, and few examined the relative contributions of individual force components including van der Waals force, capillary force and electrostatic force in their experiments. Ouyang[24] presented a method to measure these three forces separately for lamellar materials such as mica and graphite, which is, unfortunately, unsuitable for pharmaceutical powder systems due to the distinct solubility. In this work we investigated the role of each force component in

particle cohesion interactions experimentally and theoretically. The results are presented in the following chapters.

1.3 Objectives

The ultimate goal of the proposed work is to gain a fundamental understanding of the relationship between particle properties and particle interactions as well as their effects on the pharmaceutical powder blending process. Specifically, the objectives are:

- Elucidate the crucial particle characteristics and environmental factors that affect particle cohesion forces
- Determine the relative importance of individual force components contributing to particle cohesion interactions
- Establish theoretical force models to quantitatively correlate the particle cohesion interactions with particle properties and environmental factors
- Experimentally investigate the impacts of particle properties and particle cohesion on the powder blending homogeneity

1.4 Research Methodology

The proposed work consists of theoretical and experimental parts. The experimental work includes particle characterization, particle cohesion force measurement and pharmaceutical blend uniformity analysis. In terms of particle characterization, the particle size, shape, surface morphology, surface roughness, hygroscopicity and the electrostatic charging property were measured by means of microscopy and other techniques. Meanwhile, the cohesion interaction between individual particles was measured by the atomic force microscopy (AFM) and the electric force microscopy (EFM). By controlling the experimental conditions, the contribution of each force component including van der Waals force, capillary force and electrostatic force to the total cohesion force were evaluated. The blending experiments were conducted with different types of blenders and under controlled conditions. The blend kinetics was monitored in real time by the light induced fluorescence (LIF) and the blend homogeneity was analyzed off-line by the UV spectroscopy. The impact of characterized particle properties

on particle cohesion forces and powder blending performance were investigated in both micro-scale particle level and macro-scale bulk powder level. On the other hand, the mathematical models were established through MALAB code to quantitatively describe each force component as a function of the particle properties and the environmental conditions. The next three chapters described the measurement and the modeling of van der Waals force, capillary force and electrostatic force, respectively, followed by chapters which presented the impacts of particle properties and particle interactions on blending process. The framework of the research methodology is illustrated in Figure 1-2.

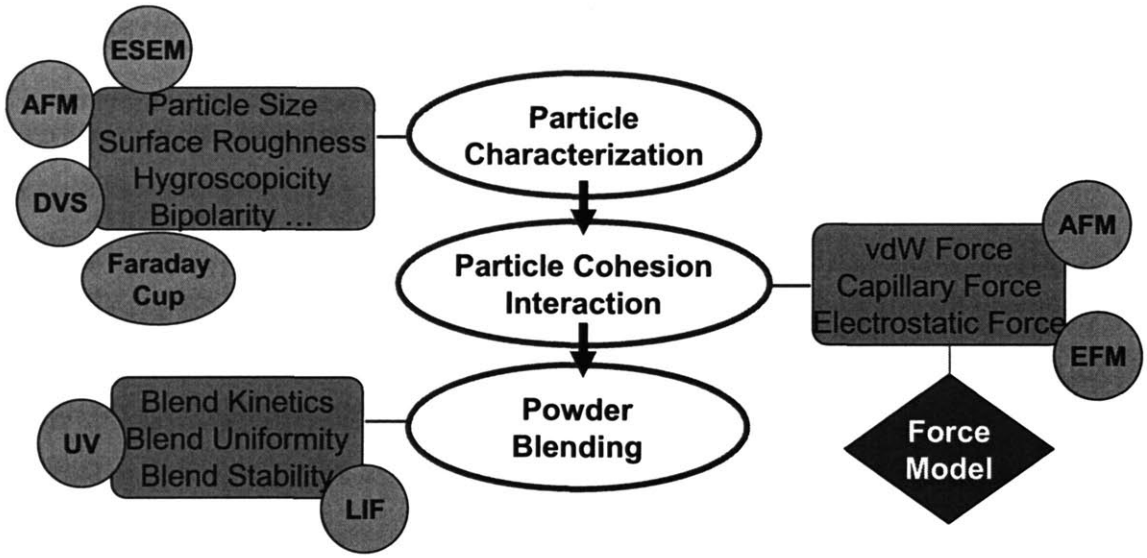

Figure 1-2 Schematic of research methodology framework

1.5 References

1. Berman, J., *The compliance and science of blend uniformity analysis.* Journal of Pharmaceutical Science and Technology, 2001, **55**(4): 209-222.
2. Prescott JK and G. TP, *A solid dosage and blend content uniformity troubleshooting diagram.* Pharmaceutical Technology, 2001, **25**(3): 68-88.
3. FDA, *PAT-A Framework for Innovative Pharmaceutical Manufacturing and Quality Assurance, Guidance for Industry*. 2004.
4. Domike, R., *Pharmaceutical Powders in Experiment and Simulation*, Department of Chemical Engineering, Massachusetts Institute of Technology, 2003, Doctoral Thesis
5. Ngai, S.S., *Multi-Scale Analysis and Simulation of Powder Blending in Pharmaceutical Manufacturing*, Department of Chemical Engineering, Massachusetts Institute of Technology, 2005, Doctoral Thesis

6. Xian Ming Zeng, Gary P. Martin, and C. Marriott, *Particulate Interactions in Dry Powder Formulations for Inhalation.* 2001: Taylor & Francis Inc., London, UK.
7. R. Hogg, D.S.C., T. W. Healy, and D. W. Fuerstenau, *Diffusional mixing in an ideal system.* Nature(London), 1966, **209**: 494-496.
8. Hersey, J.A., *Ordered Mixing - New Concept in Powder Mixing Practice.* Powder Technology, 1975, **11**(1): 41-44.
9. P.J.Loid, P.C.M.Y., *Mxing of Powders.* Chemical and Process Engineering, October 1967: 57-61.
10. Russell J.Lantz, J.B.S., *Pharmaceutical Dosage Forms: Tablets, volume 2*, ed. E.b.H.A.L.a.L. Lachman. 1981: Marcel Dekker, Inc. New York and Basel.
11. Egermann, H. and N.A. Orr, *Ordered Mixtures - Interactive Mixtures.* Powder Technology, 1983, **36**(1): 117-118.
12. Fan, L.T., Y.M. Chen, and F.S. Lai, *Recent Developments in Solids Mixing.* Powder Technology, 1990, **61**(3): 255-287.
13. Carstensen, J.T., *Advanced Pharmaceutical Solids.* 2001: Marcel Dekker, Inc. New York, US.
14. Poux, M., et al., *Powder Mixing - Some Practical Rules Applied to Agitated Systems.* Powder Technology, 1991, **68**(3): 213-234.
15. J.C.Williams, *The mixing of dry powders.* Powder Technology, 1968/69, **2**: 13-20.
16. Berman, J., *The compliance and science of blend uniformity analysis.* Pda Journal of Pharmaceutical Science and Technology, 2001, **55**(4): 209-222.
17. Mizes, H., et al., *Small particle adhesion: measurement and control.* Colloids and Surfaces a-Physicochemical and Engineering Aspects, 2000, **165**(1-3): 11-23.
18. Hein, K., et al., *Analysis of adhesion forces between particles and wall based on the vibration method.* Particle & Particle Systems Characterization, 2002, **19**(4): 269-276.
19. Shimada, Y., Y. Yonezawa, and H. Sunada, *Measurement and evaluation of the adhesive force between particles by the direct separation method.* Journal of Pharmaceutical Sciences, 2003, **92**(3): 560-568.
20. Weth, M., et al., *Measurement of attractive forces between single aerogel powder particles and the correlation with powder flow.* Journal of Non-Crystalline Solids, 2001, **285**(1-3): 236-243.
21. Sindel, U. and I. Zimmermann, *Measurement of interaction forces between individual powder particles using an atomic force microscope.* Powder Technology, 2001, **117**(3): 247-254.
22. Berard, V., et al., *Affinity scale between a carrier and a drug in DPI studied by atomic force microscopy.* International Journal of Pharmaceutics, 2002, **247**(1-2): 127-137.
23. Eve, J.K., et al., *A study of single drug particle adhesion interactions using atomic force microscopy.* International Journal of Pharmaceutics, 2002, **238**(1-2): 17-27.
24. Ouyang, Q., K. Ishida, and K. Okada, *Investigation of micro-adhesion by atomic force microscopy.* Applied Surface Science, 2001, **169**: 644-648.

2 Measurement and modeling of inter-particle van der Waals Force

2.1 Introduction

van der Waals force, also known as dispersive force, is essentially electrostatic, arising from the dipole field of an atom 'reflected back' by a second atom that has been polarized by this field. It plays a central role in particle adhesions for it is present under all environmental conditions[1]. For fine particles, it is expected to be a dominant force contributing to the particle cohesion under low humidity conditions. For two spherical, incompressible particles, the van der Waals force can be calculated as[2]:

$$F_{vdw} = \frac{A}{6H_0^2} \cdot \frac{R_1 R_2}{R_1 + R_2} \tag{2.1-1}$$

where A is the Hamaker constant; R_1 and R_2 are the radii of the two particles, respectively; and H_0 is the distance between the two particles. The formula is applicable only if the radii of the particles are much larger than the separation distance.

From the equation (2.1-1) it can be seen that the van der Waals force increases proportionally with particle size. Meanwhile, the van der Waals force decreases as a function of increased distance of separation between the particles. Hence, any means of increasing this distance would reduce the force. As a matter of fact, the van der Waals force between molecules decays so rapidly with distance that it is essentially a contact force only.

Due to its intrinsic short-range characteristic, van der Waals (vdW) force is very sensitive to the surface morphology variation of particles. The nanoscale surface roughness of micron-sized particles may lead to several order of magnitude decreases in vdW force value compared to that of perfectly smooth particles of the same size. For example, for micron-sized particles, the van der Waals force calculated based on the equation (2.1-1) is in the range of 10^{-6} Newton. However because of the existence of nanoscale asperities on the particle surface, the actual van der Waals force may go down to a few nanoNewtons. Real particle surfaces are

rarely ideally smooth. When particles have small surface asperities, typical contacts from the rough particle presents a smaller radius of curvature to the surface and the radii of the asperities may determine the van der Waals force[3]. In a study on packing of dry fine spheres where the dominant force is the van der Waals force, it was found that there is a significant decrease in dry adhesion force for a variety of surfaces with only an increase of surface roughness of a nanometer or two[4].

One of the most commonly used models of van der Waals force taking account of the effect of surface roughness is Rumpf's model[5], which is based on contact of a single hemispherical asperity centered at the surface and interacting with a much larger spherical particle along a line normal to the surface connecting their centers, as shown schematically in Figure 2-1.

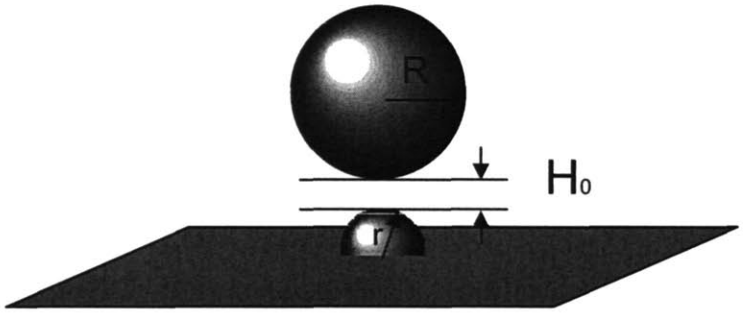

Figure 2-1 A Schematic of Rumpf's model for the interaction between a particle and a rough surface

The model consists of two terms that describe the total van der Waals interaction. The first represents the interaction of the adhering particle in contact with the asperity, while the second describes the 'noncontact' force between the adhering particle and the flat surface separated by the height of the asperity. The equation is in the form of:

$$F_{vdw} = \frac{AR}{6H_0^2}\left[\frac{r}{r+R} + \frac{H_0^2}{(H_0+r)^2}\right] \qquad (2.1\text{-}2)$$

where R is the radius of the adhering particle, r is the radius of the asperity, H_0 is the separation distance.

Based on Rumpf's formula, Rabinovich proposed a modified model to describe the interaction between a spherical particle and a surface with nanoscale roughness[6]. When the surface

roughness is fairly small, the radius of the asperity actually increases. In this case, the center of the asperity must be located some distance below the surface. Consequently, the height of the asperity and its breadth are both incorporated in the model.

$$F_{vdw} = \frac{AR}{6H_0^2}\left[\frac{1}{1+58R\cdot rms/\lambda^2} + \frac{1}{(1+1.817rms/H_0)^2}\right] \quad (2.1\text{-}3)$$

Where λ is the peak-to-peak distance between two asperities, and *rms* is the value obtained directly from the AFM measurement to represent the surface roughness.

Rabinovich's model is applicable only if $\lambda >> 14.5$rms, which means that the model is not suitable for high aspect ratio or jagged surfaces. Besides, the model did not take account of the surface roughness of the adhering particle. These limitations make it inaccurate to describe the interaction between two rough particles, in which case, the surfaces of both particles are covered with asperities and interact with multiple contact points due to the irregular surface morphologies.

As mentioned above, for particles of rough surfaces, nanoscale roughness turns out to be a critical parameter in quantifying van der Waals force. The characterization of particle surface roughness is thus a requisite step for the study of inter-particle van der Waals force. In this research it was implemented by the advanced microscopy techniques. The method will be described in the next section, followed by the experimental measurement and the modeling of the van der Waals force between two particles with rough surface.

2.2 Characterization of particle surface morphologies

2.2.1 Qualitative description of particle surface morphology by ESEM

With the aid of the Environmental Scanning Electron Microscopy (ESEM), the size and the shape of one or more micron-sized particles can be observed clearly under the microscope. Figure 2-2 shows the ESEM pictures of microcrystalline cellulose (MCC) particles obtained from two sources: Celphere® (Asahi Kasei Corporation, Tokyo, Japan) and Avicel® (FMC Corporation, Delaware, USA). The two types of particles have quite different shapes and surface morphologies despite the same material. Celphere® displays a smoother particle

surface and more spherical particle shape than Avicel®. To reduce the variation caused by the shape effect, Celphere® was used in our experiments. In the following chapters the general term MCC refers to MCC Celphere®, if not stated otherwise.

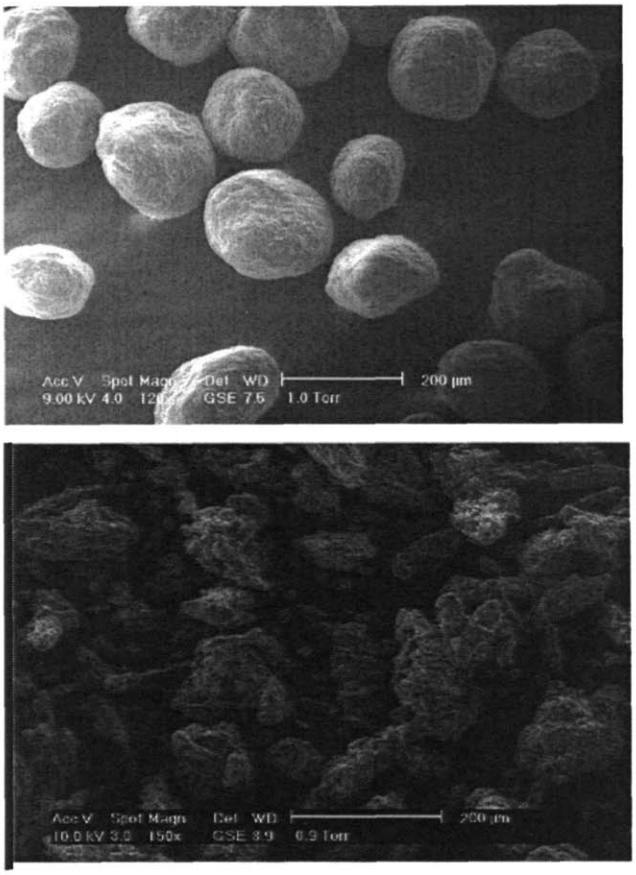

Figure 2-2 ESEM pictures of MCC particles: (a) Celphere®; (b) Avicel®

In addition, qualitative information on the particle surface roughness also can be obtained from the ESEM pictures. As shown in Figure 2-3, the surface morphologies of four particles of different materials were displayed in detail in ESEM images. In contrast to relatively smooth surfaces of glass bead and polystyrene bead (Duke Scientific Corp., California, USA), pharmaceutical particles such as MCC and lactose (Pharmatose® DCL11, DMV International, the Netherlands) have rough surfaces fully covered by small and large asperities. It was observed from the ESEM image that lactose has much rougher surfaces than MCC.

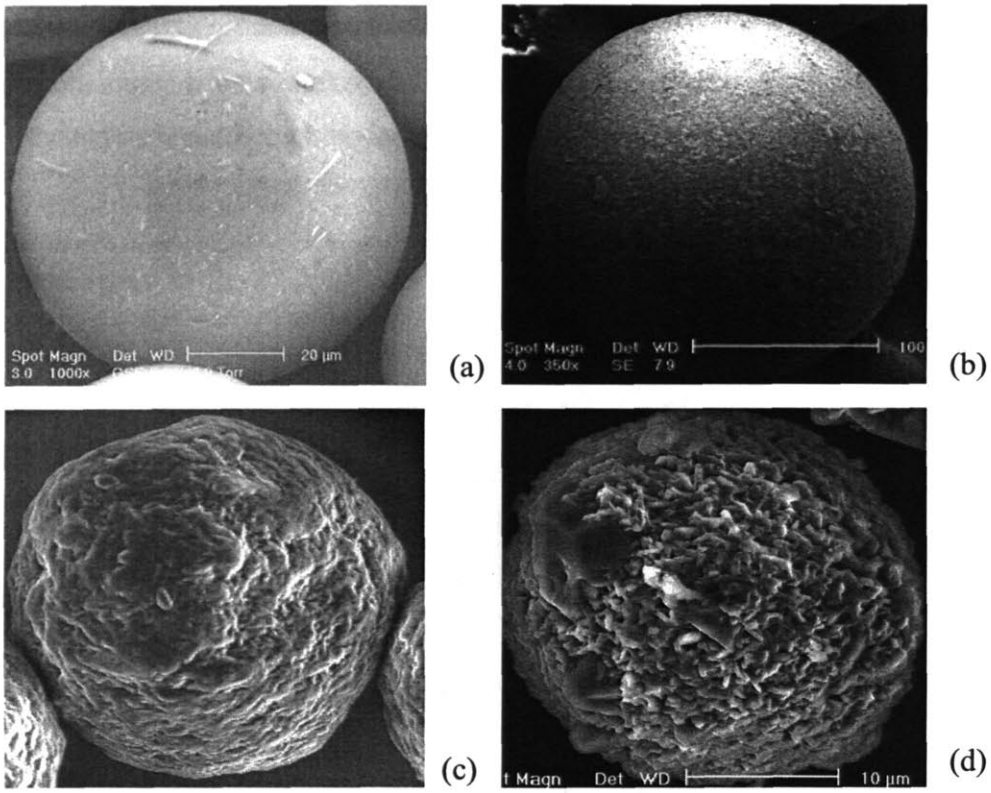

Figure 2-3 ESEM pictures of a single particle of: (a) glass bead; (b) polystyrene bead; (c) MCC; (d) lactose

2.2.2 Quantitative description of particle surface roughness by AFM

AFM allows measurements of the surface profiles at the nanometer scale. In this research we utilized a Multimode AFM (Nanoscope® IIIa, Digital Instruments, California, USA) in its contact mode, where the probe's tip scans across the surface of a single particle to map the surface topography. A bare triangular silicon nitride cantilever (DNP-20, Veeco Probes, California, USA) was chosen as the probe because it is robust and relatively inexpensive.

The AFM surface imaging was made for individual particles of different materials. The AFM scanning area is 7×7 µm for glass bead and polystyrene bead and 5×5 µm for MCC and lactose. The scan rate is 10µm/s. A relatively high gain value is set to get height images of higher resolution. For each particle, three repeated measurements were conducted at three different spots on the surface.

From the 2-D AFM height images of the scanned surface area, the corresponding surface profile along an arbitrary scan line can be displayed (see Figure 2-4).

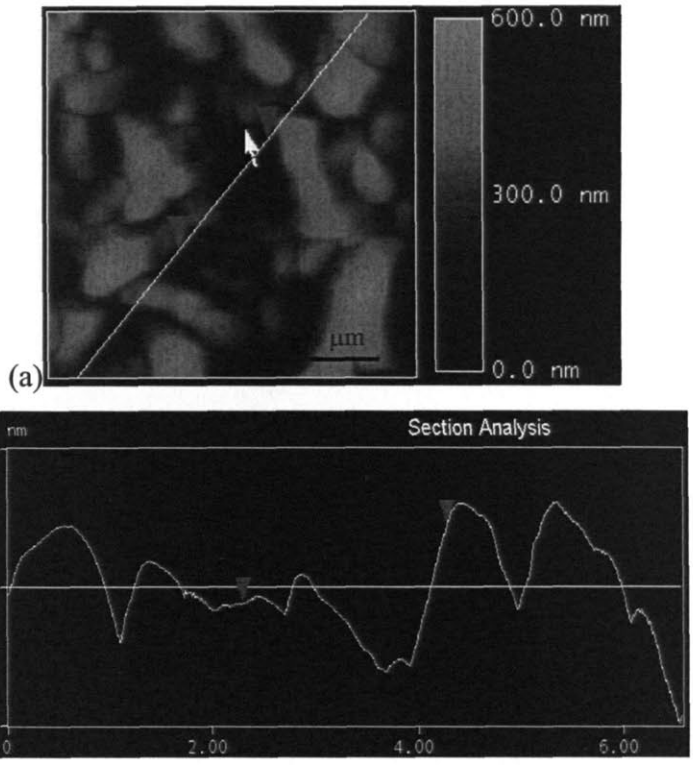

Figure 2-4 AFM height images of a lactose particle:
(a) 2-D surface topography; (b) Section analysis of the surface profile

In addition, to view the surface feature in a more intuitive way, the 2-D map can be converted to a 3-D image. Figure 2-5 shows the 3-D AFM surface images of four different particle materials. The difference in the degree of surface roughness of four particles corresponded well with our observation in Figure 2-3. All the 3-D images were scaled to the same Z (height) dimension and flattened to avoid the surface curvature effect.

To quantitatively describe the roughness of the surface, the AFM height image was analyzed by the Nanoscope III software off-line. Generally particle surface roughness includes two attributes: roughness heights and lateral dimensions. Lateral dimension describes how frequently the surface height changes[7], while roughness heights were used to represent surface roughness. These include arithmetic mean surface roughness, root mean square roughness, average peak to valley height between five highest peaks and five deepest valleys

within the sampling length, and skewness. Among them the root mean square (RMS) value is most commonly used to represent the surface roughness. RMS value is calculated by the software as:

$$RMS = \sqrt{\frac{\sum (Z_i)^2}{N}} \tag{2.2-1}$$

where Zi is the height value at point i and N is the number of points within the analyzed surface area. In a typical AFM surface image, N is set as 128×128. A higher value of 256×256 or 512×512 is applicable as well but associated with a longer scanning time.

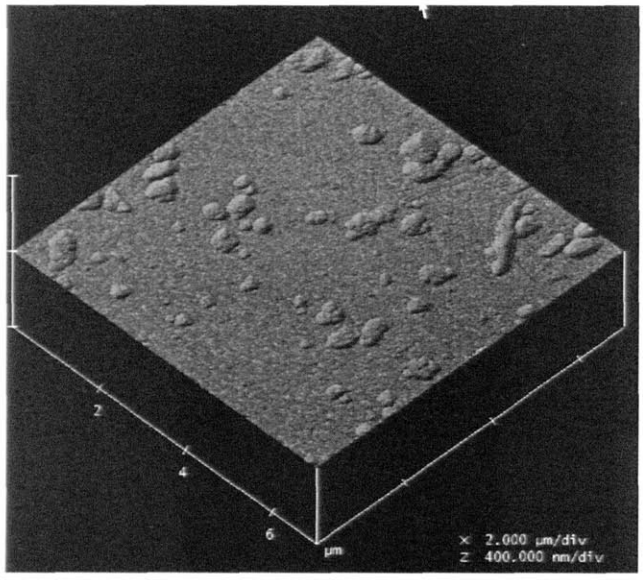

(a)

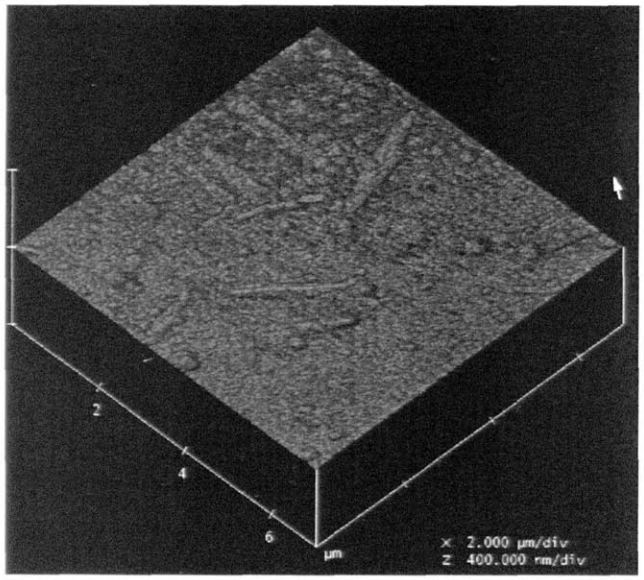

(b)

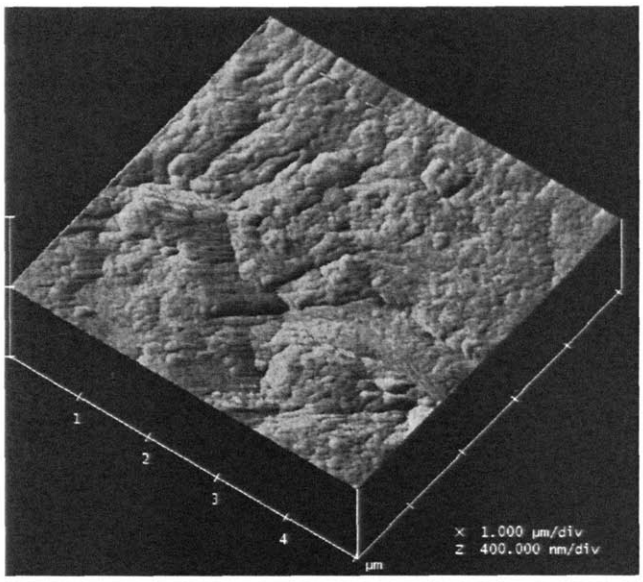

(c)

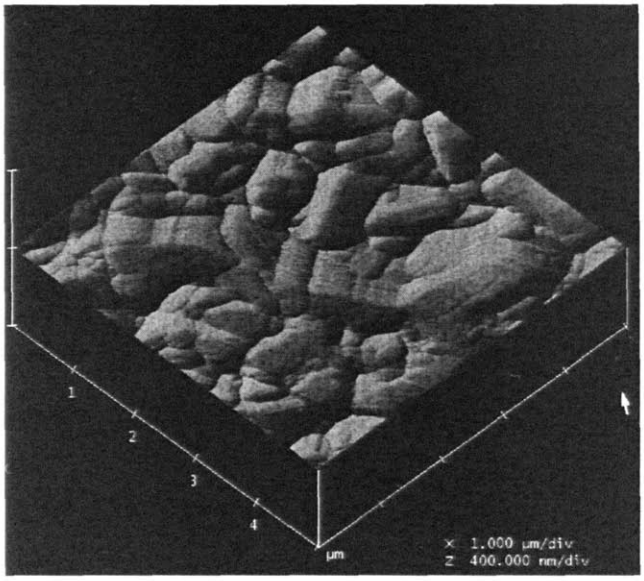

(d)

Figure 2-5 AFM 3-D surface image of (a) glass bead ; (b) polystyrene bead ; (c) MCC particle ; (d) lactose particle

Other than the RMS value, additional information was collected from the AFM surface images with respect to asperity shape, asperity size and asperity density distribution. By drawing a height contour map with MATLAB, we estimated the maximum length of the projection of each asperity on the surface, which was denoted as the asperity diameter, and the ratio of the area occupied by asperities to the total scanned area, denoted as the fractional coverage. One typical height contour of the particle surface is shown in Figure 2-6.

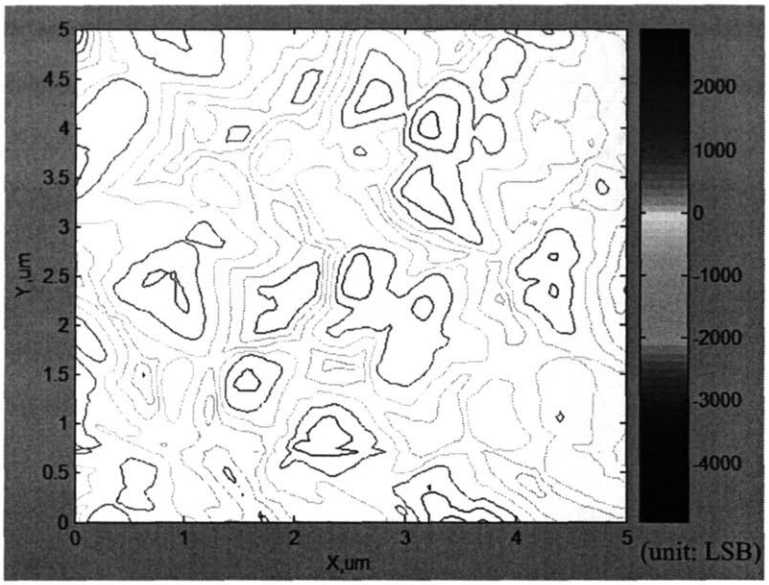

Figure 2-6 Height contour of a scanned lactose particle surface

As a result, the surface roughness, the asperity size and the asperity distribution over the scan area were characterized. All this information put together gave us a more complete depiction of the particle surface morphology. Table 2-1 listed those parameters derived from the AFM image analysis of particle samples of different materials. All the values are the average of three repeated measurements from one single particle. In addition to the sample particles, the surface roughness of the particle adhered on the tip was also measured in the same way.

Table 2-1 Typical parameters characterizing the particle surface morphology

Material	Particle Diameter (μm)	RMS (nm)	Asperity Diameter (μm)	Fractional coverage
Glass bead	70	12±1	0.4±0.1	0.2
Polystyrene bead	30	3±1	0.4±0.1	0.1
Polystyrene bead	280	37±6	0.5±0.2	0.5
MCC	100	70±7	0.8±0.2	0.3
Lactose DCL11	108	96±20	1.3±0.2	0.7
Lactose DCL22	84	118±10	0.7±0.2	0.8

2.3 Measurement of inter-particle van der Waals force

2.3.1 Tip and sample preparation

Triangular silicon nitride cantilever (DNP-20, Veeco Probes, California, USA) was used for the AFM force measurement. Using the AFM piezotube as the micromanipulator, the cantilever was dipped into a tiny droplet of epoxy resin adhesive gently, then brought into contact with a single particle lying on the sample plate and held in air for about 5 minutes till the glue got dry. Care must be taken for the amount of glue used in the tip preparation to prevent the particle surface from undesired contamination. The ESEM pictures of particle-adhered cantilevers were shown in Figure 2-7.

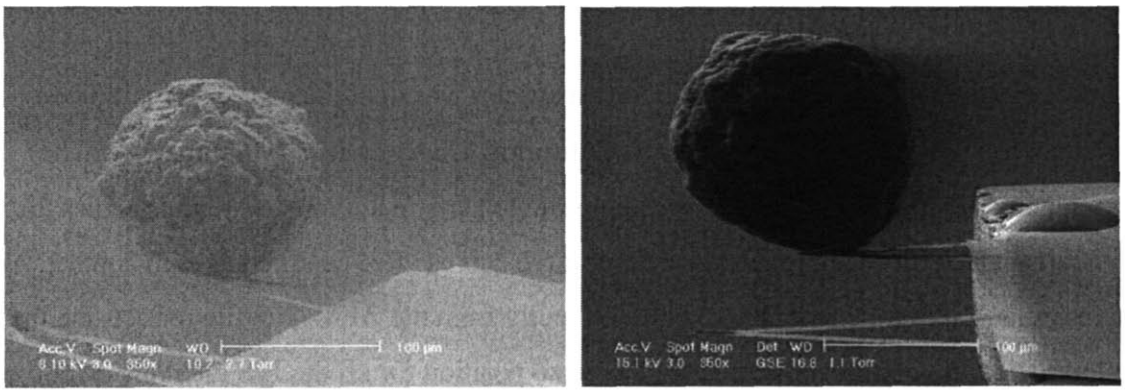

Figure 2-7 ESEM pictures of a single lactose particle (left) and a single MCC particle (right) adhered on an AFM cantilever

In order to convert the AFM data to the real force values, the cantilever stiffness must be known beforehand. In this work the normal spring constant of each cantilever was experimentally determined by the Molecular Force Probe (Asylum Research, Santa Barbara, CA) prior to the adhesion of any particle to the tip. The instrument analyzes the time average of the thermally excited vibration amplitude of the cantilever, which is proportional to the normal spring constant. The thermal fluctuation was measured three times for each cantilever. The average and standard deviations of the spring constant for each cantilever were achieved. The spring constant values of cantilevers used in the measurement are in the range of 0.34-0.49 N/m.

10-15 sample particles were randomly picked up from the powder population with a sterile disposable needle (Products CO. Inc., Vineland, NJ, USA) under an optical microscopy, and

then fixed onto a sample plate with a double-side tape. All the selected sample particles were labeled in order for the convenience of later surface roughness measurement and force measurement.

All the prepared cantilevers and the sample particles to be measured were stored in a vacuum desiccator with P_2O_5 as desiccant for a couple of days before the measurement. The temperature and the relative humidity inside the chamber are 22°C and 5%, respectively. This storage step is meant to minimize the electrostatic charges on the surface and to eliminate the water vapor absorption on the surface.

2.3.2 Force measurement by the AFM

The force measurement between two individual particles was implemented by a multimode AFM (Nanoscope® IIIa, Digital Instruments, California, USA) in force volume mode. The particle-adhered tip moves into contact with one single particle at regular intervals across the scanning area. One pair of approach and retract force curves were captured at each contact. As shown in Figure 2-8(a), the raw data exported directly from the AFM data file reflects the tip deflection variation with the movement of the piezo position for all the 128 intervals on one single sample line. Given the sensitivity of deflection, the Z size range, the spring constant and all other necessary information in the parameter list of the AFM data file, the raw data can then be converted mathematically to the actual force value versus the tip-to-sample distance, as shown in Figure 2-8(b). The difference between the lowest point and the non-contact region of the retract force curve represents the cohesion force, also called the separation or pull-off force, between the two particles. In the force volume mode, an array of 16×16 cohesion force data were collected over a scanning area of 5×5 μm in one measurement. For each pair of particles, three repeated measurements were conducted at three different spots on the particle surface. The reported inter-particle force is the average of these 16×16×3 = 768 data points. The reported standard deviation refers to the 3 repeated measurements, if not stated otherwise.

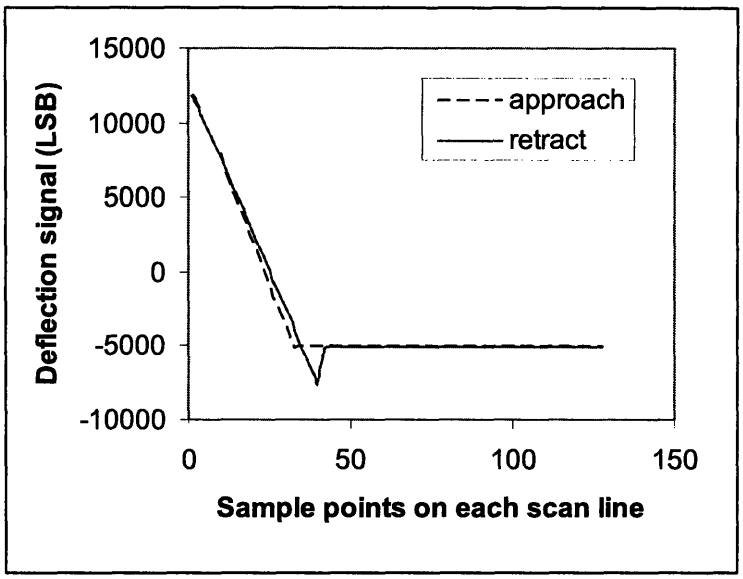

(a)

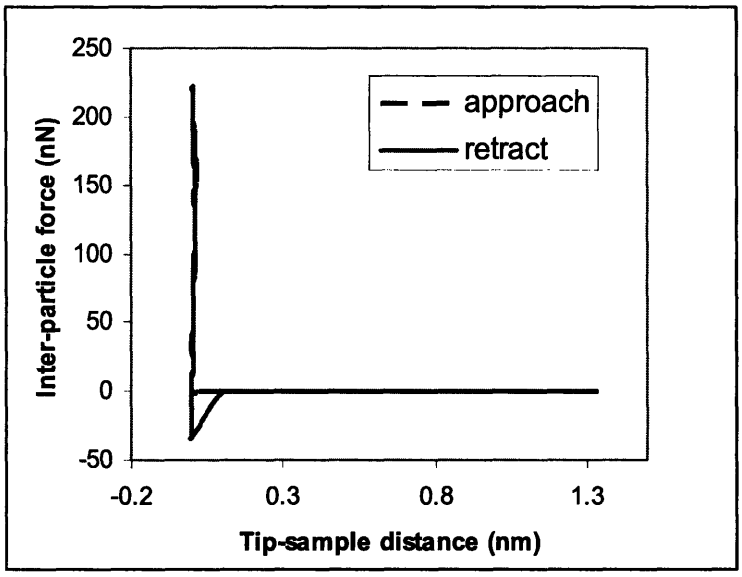

(b)

Figure 2-8 Typical approach and retract force curves between a single lactose particle and another lactose particle adhered on a silicon nitride cantilever, drawn: (a) directly from the AFM raw data regarding the tip deflection (LSB) of all the 128 data pointed collected on one single scan line; (b) from the converted data regarding the actual inter-particle force (nN) variation with the tip-to-sample distance (nm).

To exclude the effect of capillary force during the measurement, the AFM experiments were carried out in a humidity-controlled chamber. The relative humidity inside the chamber was kept at 2% or less by dry nitrogen gas. The effect of electrostatic force also is neglected in our experiments, assuming the electrostatic charges on the particle surface, if there is any, have been dissipated sufficiently during the sample storage period before each measurement. As a

matter of fact, no obvious evidence of presence of electrostatic force such as the distortion of the curve shape was found from the captured approach force curves.

Particle interactions of five different materials were investigated in our experiments. The five materials were glass beads, polystyrene beads, lactose DCL11, lactose DCL22 and MCC. For each material, both surface roughness measurement and force measurement were conducted on 7-10 sample particles.

2.4 Modeling of inter-particle van der Waals force

In previous studies, different models have been put forward to illuminate the effect of surface roughness on the van der Waals (vdW) force. Most of them are mainly focused on the interaction between a sphere and a rough substrate. Rabinovich and his colleagues depicted surface roughness as close-packed hemispherical asperity caps and troughs with their centers below the surface[6]. Unfortunately the model is valid only for surfaces with small asperity amplitude and sparse asperity distribution. Meanwhile, it fails to account for the possibility of multiple contact points and the deformation occurring at the contact region. As shown in the work done by Beach et al[8], the adhesion force between pharmaceutical particles with irregular geometry and rough polymeric surfaces is underestimated using Rabinovich's model when deformation at the interface is not negligible. In Forsyth's work, the effects of the asperity and the deformation on the vdW force of a particle to a wall were discussed.[9] However, the simplified model in which the asperity was depicted as a small sphere intersected with the large spherical particle always overestimates the force. An absorbed layer model was built based on Lifshitz's theory by Gotzinger et al.[10], in which the thickness of the absorbed water layer on the surface had to be incorporated as a fitting parameter to predict the metal particle-substrate vdW interactions.

Inspired by Cooper's work[11, 12], a model is developed in our study to simulate the interaction between two individual particles with rough surfaces. The vdW force between two particles is predicted by the model and the correlation between the vdW force and the particle characteristics investigated.

The basic procedures for our model simulation involve generating two surfaces with specific asperity properties and calculating the vdW force between the two surfaces in contact with each other by the surface element integration method. All the modeling work is implemented using a MATLAB code developed by our lab. The details of the algorithm are described below.

2.4.1 Simulation of particle surfaces with defined roughness

One disadvantage of all the force models noted above is that the morphological heterogeneities are not well characterized due to the oversimplification of asperity size and shape. In reality the surface morphologies of the actual particles are often very irregular and complicated. To improve the predictability of the force model, it is critical to make the simulated particle surface morphology close to the real case.

Various approaches for modeling surface roughness have been proposed. Recently, Eichenlaub compared three different methods to simulate particle surface roughness[13]. Each method has its advantages and disadvantages. In fractal method some parameters are difficult to determine and must be assumed, which limits its application. The fast Fourier transform method seems to be the most accurate way to reproduce a rough surface, at the cost of the complicated algorithm. Compared to these two methods, hemispherical asperity method is fast and simple, although it requires well-defined asperity characteristics and fails to simulate asperities with complex shapes. The roughness model Cooper developed in the earlier stage represented asperities as hemispheres with constant radius and uniform spacing around a sphere[14]. Later Bhattacharjee and his coworkers developed a new model in which rough surfaces are generated by randomly placing hemispherical asperities on a smooth planar surface, given the mean size and the density of the asperities[15]. The same idea was used for reference in our work to simulate the particle surface roughness.

First of all, the contact regions of the two particles were simulated as two circular plates, respectively. Each plate had a defined diameter equivalent to the scan size in the AFM measurement, which, in our experiments, was 5 μm. Since the scan size is comparatively

small to the whole particle diameter (>70 μm), it is reasonable to neglect the effect of curvature.

Subsequently, the asperities were simulated as oblate hemispheroids with the center located on the planar surface. Two parameters were used to define the size of one spheroid: the diameter of the bottom area and the height of the asperity peaks. As described in Section 2.2.2, the asperity diameter and the asperity height of each particle were determined from the AFM measurement, so was the fractional coverage of the asperities on the surface. Assuming that the diameters of all the asperities on a single particle are normally distributed, we can generate an array of random numbers given the mean and the standard deviation of the asperity diameter. Likewise we can get another array of random numbers to represent the distribution of asperity height on the particle surface. In the simulation, each hemispheroid was generated through picking one asperity diameter value and one asperity height value from these two arrays respectively. All the simulated hemispheroids are positioned randomly on the surface in such a way that only a maximum of 20% overlapping is allowed between any two hemispheroids. Every time when one asperity is located, the fractional coverage of the surface area was calculated. The placement of the new hemispheroids continues till the fractional coverage attains the given value. The surface image of a real lactose particle and the simulated surface based on the measured asperity characteristics are shown in Figure 2-9 (a) and (b).

To mimic the interaction between two particles, another rough surface was generated in the same way. The two simulated surfaces were placed some distance in between, with the hemispheroid asperities on each surface facing each other, as shown in Figure 2-10 .

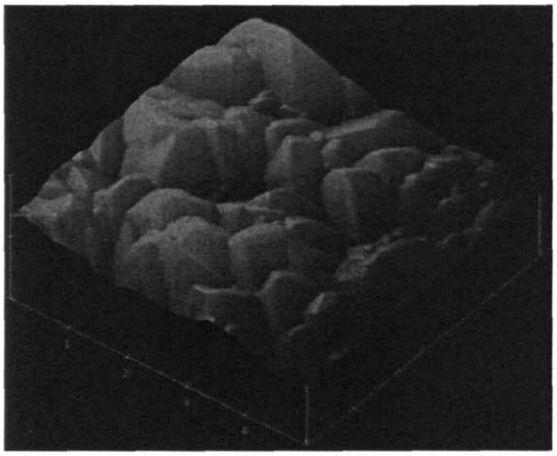

(a)

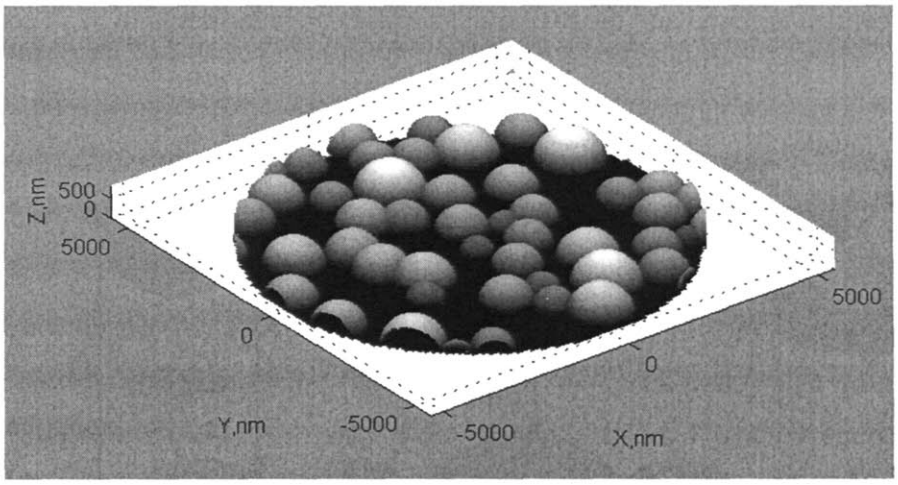

(b)

Figure 2-9 Surface images of: (a) actual lactose particle surface; (b) simulated particle surface;

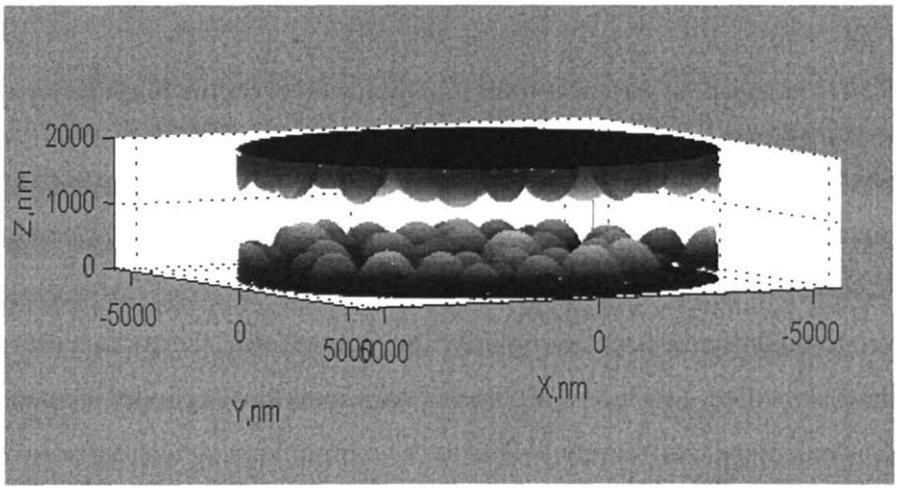

Figure 2-10 Illustration of two simulated particle surfaces getting into contact

2.4.2 Calculation of van der Waals force by surface element integration method

The generated two rough surfaces were both segmented into numbers of volume elements. Each element is a cylinder whose diameter is only one thousandth of the surface diameter. The length of each cylinder L_i and the distance between two opposite cylinders D_i are varied with the surface morphological profile, as shown in Figure 2-11. The vertical distance between the two surfaces H is determined in such a way that the minimum distance between any pair of opposite elements D_{min} is 0.4 nm (atomic distance). As a consequence, at least one single point of contact is found and the two rough surfaces are considered to be in contact with each other.

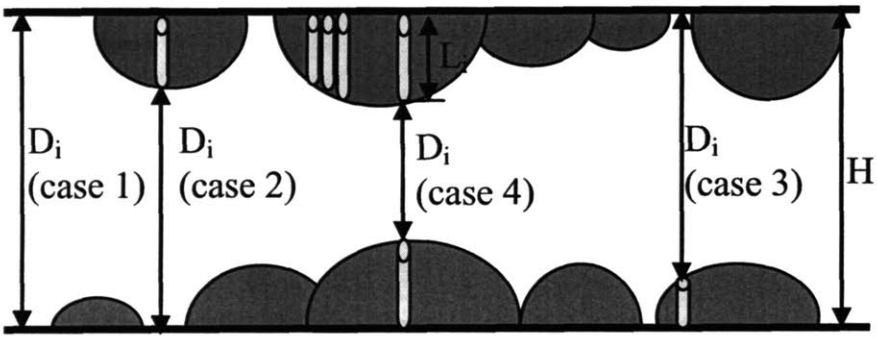

Figure 2-11 Schematic of surface element segmentation between two rough surfaces

The vdW force between two rough particles consists of two components. One is the contribution from asperity-asperity interaction and the other from surface-surface interaction.

In our simulation, to quantify the asperity-asperity interaction force, the surface element integration method is applied, i.e., the vdW force of each individual cylinder element to the opposite surface is calculated and summed. Due to the morphological heterogeneity of the two surfaces, there are four possible cases during the calculation, schematically shown in Figure 2-11: (1) both elements are located at areas without any asperities; (2) only the element at the upper surface is located within a hemispheroid; (3) only the element at the bottom

surface is located within a hemispheroid; (4) both elements are located within a hemispheroid at their respective surfaces. In the first case, the length of each element becomes zero and the interaction is thus attributed later to the surface-surface interaction part. In case 2 and 3, since the diameter of the element is much smaller than the length scale of the whole planar surface, the vdW force between the element and the opposite surface is simplified as the vdW force between a cylinder and an infinite plane. The force equation is expressed as:

$$F_{element,i} = \frac{Ar_0^2}{3} \cdot \left[\frac{1}{(2D_i)^3} - \frac{1}{(2D_i + L_i)^3} \right] \qquad (2.4\text{-}1)$$

where A is the Hamaker constant of the particle material, r_0 is the radius of the cylinder, D_i is the distance between the cylinder i and the opposite surface, L_i is the height of the cylinder itself.

In the last case, the force equation is the same as in case 2 and 3. The only difference is that D_i is defined as the distance between the two cylinders, and L_i is the larger one of the height values of the two cylinder elements. The longer cylinder was chosen as the integration element because its height value is more representative of asperity effect in the sense of surface roughness.

In the calculation, the values of r_0, D_i and L_i were determined based on the simulated surface asperity profile. The Hamaker constant value of different materials was found from literatures and listed in Table 2-2. The detailed measuring approach of each cited data was not addressed in the literatures. Generally the Hamaker constant is calculated from Litshitz theory using full spectra data of the material in vacuum, or calculated using force vs. separation data from surface force apparatus and atomic force microscopy studies[25].

Table 2-2 Hamaker constant of different materials

Material	Glass	Polystyrene	Lactose	MCC
A (10^{-20} J)	6.5[16]	7.9[17]	7.2[18]	18.5[19]

The surface-surface interaction can be calculated directly by the equation for ideal sphere-sphere interaction, as shown below.

$$F_{vdw} = \frac{A}{6H_0^2} \cdot \frac{R_1 R_2}{R_1 + R_2} \tag{2.4-2}$$

where R_1, R_2 are the radii of the two spherical particles, respectively; H is the distance between the two particles. In our model H equals to the distance between the two generated surfaces.

The total vdW force between the two rough particles can be expresses as:

$$F_{vdw} = \sum_{case2,3,4} F_{element,i} + F_{s-s} \tag{2.4-3}$$

If the two surfaces are perfectly smooth, the vdW force is completely dependent on the surface-surface interaction. In the presence of asperities, the surface-surface interaction will decrease dramatically with the increase of the asperity height because of the enlarged H value. The asperity-asperity interaction will become dominant accordingly.

The area of the actual contact region between the two particles is another important parameter to affect the vdW force. However, it is difficult to precisely measure the actual contact area which, as studied in previous work, depends on the applied load, the modulus of elasticity of the material, and the surface roughness. To simplify the problem, here we use Hertz's theory to identify the apparent contact area A_c between two interacting spherical particles that undergo elastic deformation without considering the asperity contact effect:

$$A_c = \pi[0.75 \frac{d_1 d_2}{d_1 + d_2} F_p (\frac{1-\mu_1^2}{E_1} + \frac{1-\mu_2^2}{E_2})]^{2/3} \tag{2.4-4}$$

Where d_1 and d_2 are the diameters of two particles respectively; F_p is the pull-off force measured by AFM; E_1 and E_2 are the Young's modulus of the two particles, respectively; μ_1 and μ_2 are the poisson ratios of the two particles. The values of both Young's modulus and poisson ratio of different materials were obtained from the literatures and are listed in Table 2-3.

Table 2-3 Young's modulus and poisson ratio of different materials

Material	Glass[20]	Polystyrene[21]	Lactose[22]	MCC
Young's modulus (GPa)	71	4.7	3.57	25[23]
Poisson ratio	0.22	0.33	0.12	0.30[24]

In fact, the contact surface area and the interaction force applied on the contact point affect each other simultaneously. Contact area will be enlarged upon a higher interaction force and in turn the interaction force will elevate with a larger contact area. Since the contact area and the vdW force are the two variables coupled with each other, and neither of them is known before the calculation, a loop is used in our simulation, starting with an initial value of contact radius equal to the scan size. If the calculated force value and the contact area do not satisfy Equation (2.4-4), the contact area value is updated and the vdW force recalculated till the code converges.

2.5 Results

2.5.1 Comparison between the calculated and the measured van der Waals force

To test the validity of the proposed vdW force model, the van der Waals forces calculated from the proposed model were compared with the force data measured from AFM experiments.

For a pair of particles in contact with each other, the surface morphology of each particle was firstly characterized by the AFM prior to the AFM force measurement. The corresponding particle asperity characteristics were input into the MATLAB code as parameters. The rough surfaces were generated computationally with random asperity distributions based on the given asperity features and renewed every time when the code was run. To be more representative of the real case, the code was run 30 times repeatedly for each pair of particles. Each time the vdW force was calculated by integrating the new simulated surface. In the end, the average and the standard deviation of this 30 calculated vdW force values were obtained and compared with the experimental force data.

Figure 2-12 (a-e) showed the comparison between the calculated vdW force and the experimental data for glass beads, polystyrene beads, lactose DCL11, lactose DCL22 and MCC. For each of the five different materials, the cohesion forces of 7-10 particles were measured by the AFM under dry nitrogen environment and the pull-off force was expected to

be inter-particle van der Waals force predominantly. As described in the section 2.4, the theoretical van der Waals force was calculated from the force model, in which the distance between the two contacting particles was 0.4nm. It can be seen that most of the experimental data points fell within the error bar of the corresponding calculated force and about one third of the experimental data points agreed well with the average value of the calculated results.

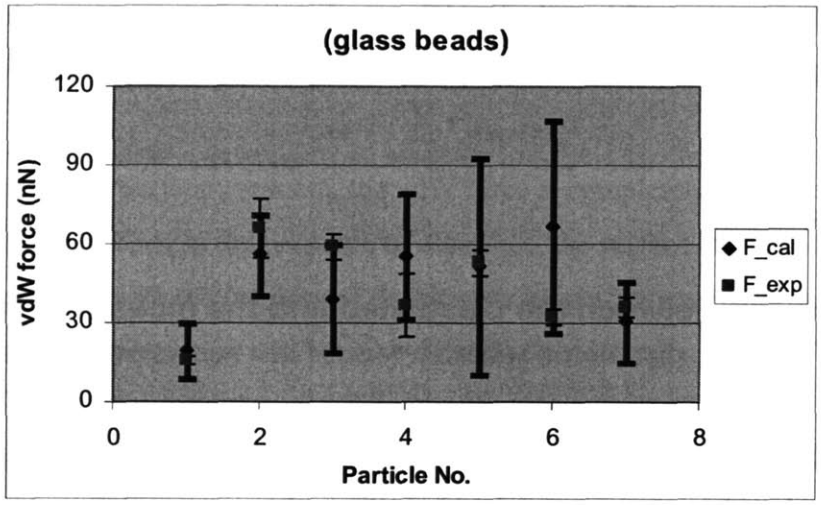

(a)

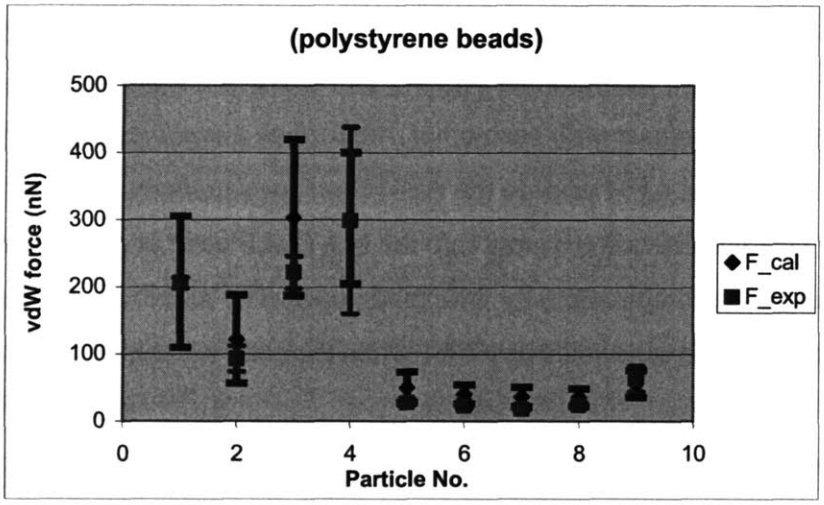

(b)

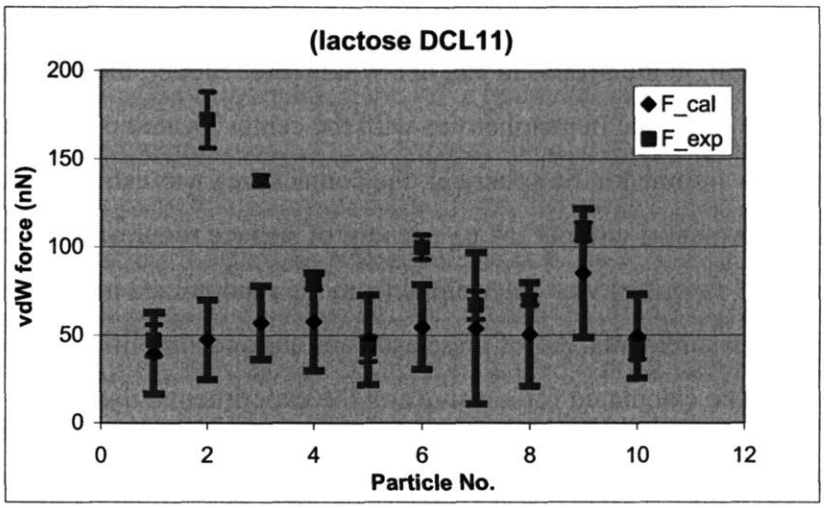

(c)

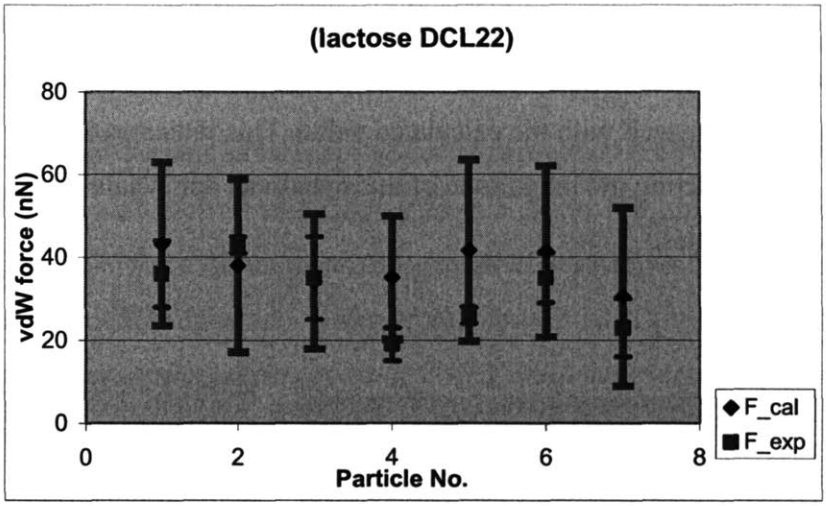

(d)

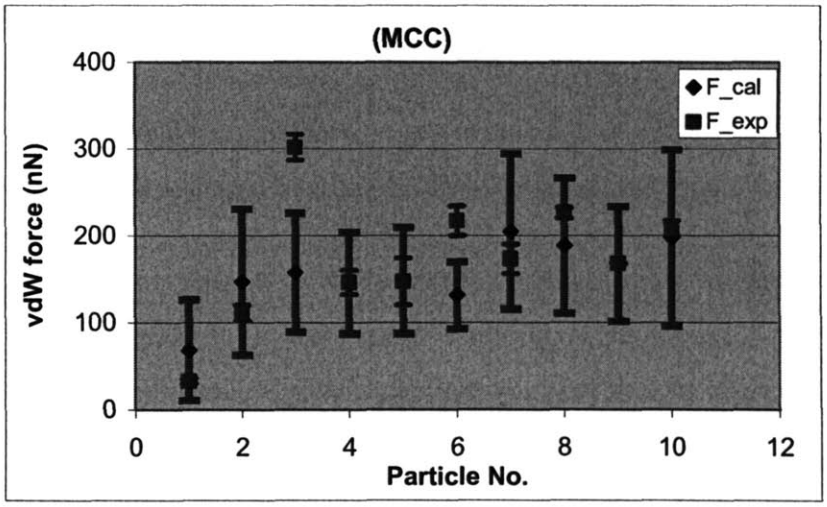

(e)

Figure 2-12 Comparison between calculated vdW force and experimental data: (a) glass beads; (b) polystyrene beads; (c) lactose DCL11; (d) lactose DCL22; (e) MCC

To simplify the problem, in the proposed van der Waals force model, the surface asperity shape was assumed to be oblate hemispheroids with the center located on the planar surface; the particle shape was assumed to be spherical; the contact area was estimated from Hertz's theory for elastic deformation without taking account of surface roughness effect; and the distribution of surface asperities was determined from the randomized modeling process instead of physical measurements. All of these assumptions and simplifications led to the discrepancy between the calculated force value and the experimental data.

Figure 2-13 is an assembly of all measured vdW force data. The solid blue line represents the average value of the calculated force value, and the two dash blue lines correspond to ±15% error of the average calculated force value. Most of the experimental data points were within this range and agreed very well with the calculated value. This indicates that the proposed model is capable of predicting the magnitude of the actual van der Waals force interaction between two rough particles.

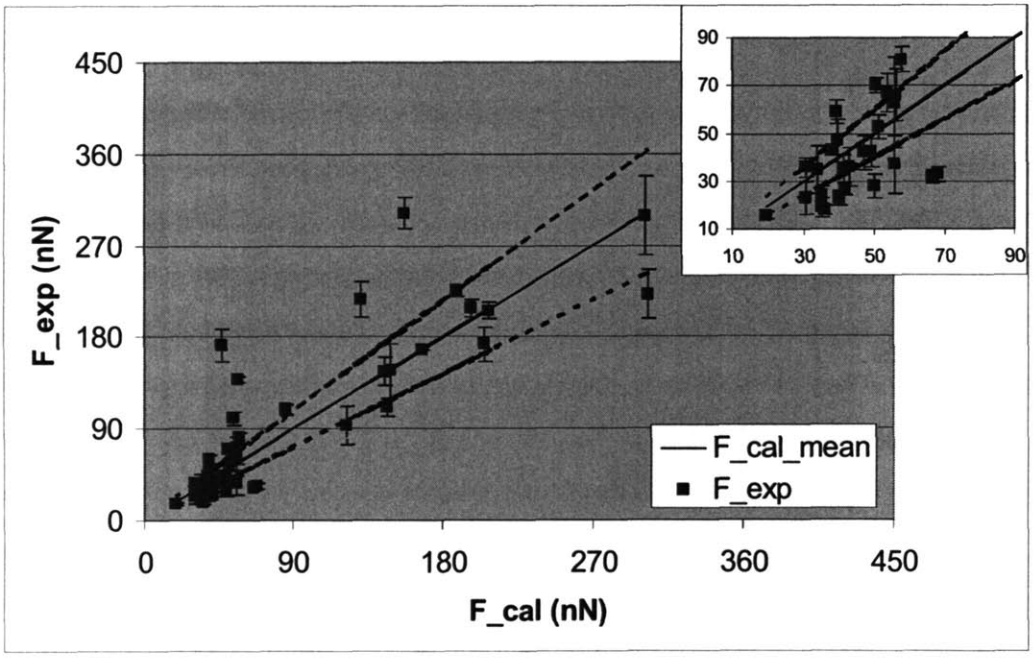

Figure 2-13 Comparison between the experimental data and the average of the calculated forces (inset: a close look at lower force region)

2.5.2 Parametric study based on the modeling results

In addition to its application in estimating the vdW interaction force between two particles, the particle simulation method enabled us to explore the correlation between the particle characteristics and the particle interaction force. There are many particle characteristic variables which may affect the particle interaction, such as particle size, asperity size and distribution, asperity height and distribution, and asperity fractional coverage on the particle surface. With the aid of the simulation, we are able to study the sensitivity of the vdW force to each specific particle characteristic parameter by setting other variables constant values in the code. As stated above, each reported force value was the average of thirty repeated simulations with respect of one set of particle characteristic parameters. This provides an opportunity for exploring the effect of material property specification on particle interaction.

The first particle characteristic to be investigated is particle size. Given the average asperity diameter of 500 nm, with particle size varying from 5 μm to 160 μm while other parameters kept constant, the vdW force between two rough particles was found to be apparently independent of the particle diameter, as shown in Figure 2-14. The same trend was observed when the average asperity diameter was set to 700 nm, but the average van der Waals force increased.

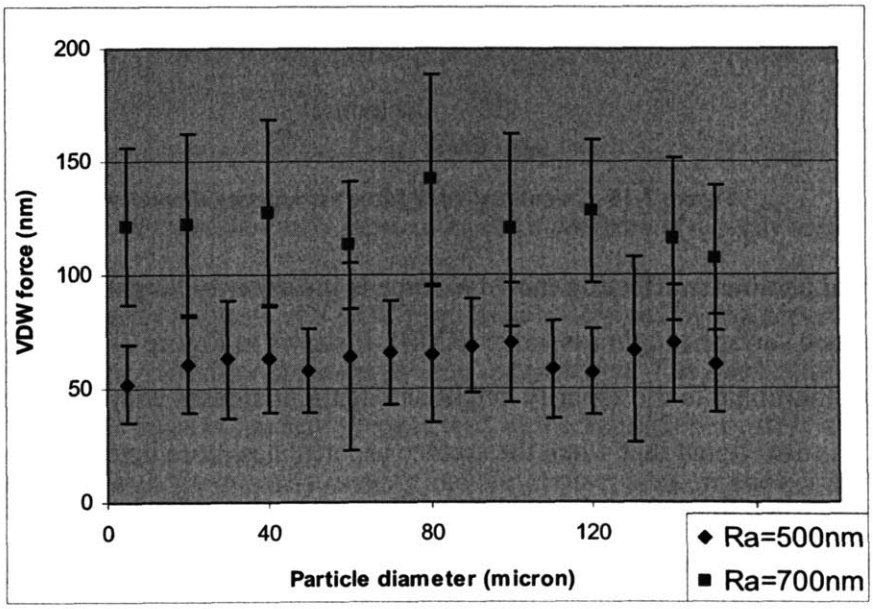

Figure 2-14 Calculated vdW force vs. particle diameter

This result is distinctive from the traditional Hertz's theory, which states that the vdW force is proportional to the particle diameter for two particles with smooth surfaces in contact with each other. It implies that for micron-sized particles with nanoscale roughness, the asperity-asperity interaction contribution plays a dominant role in the vdW force, in contrast to the surface-surface interaction. Therefore not surprisingly, it is the asperity size rather than the particle size that will influence the interaction. When the two particles are in contact, it is actually the asperities that are in contact and in many cases there is multiple-asperity contact. As seen from Figure 2-14 and Figure 2-15, the vdW force increases with the increase of the asperity diameter.

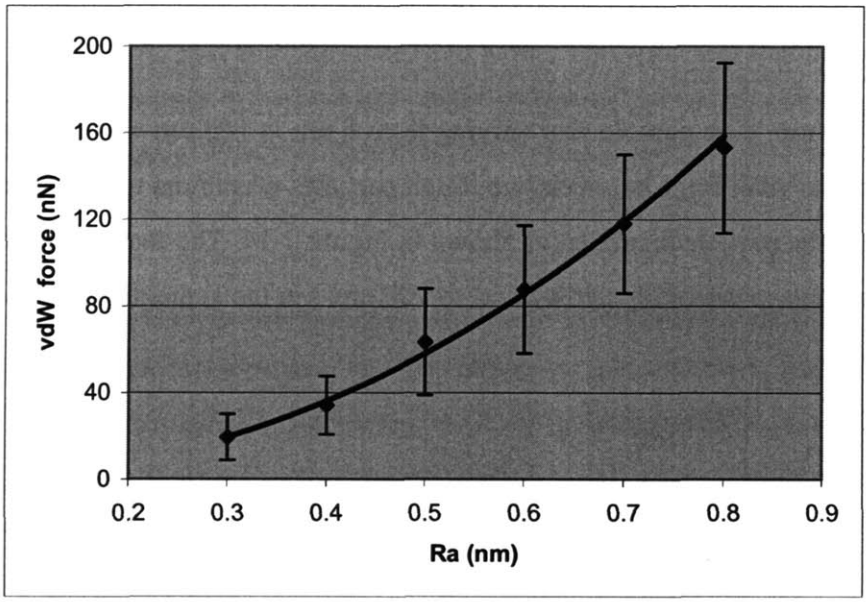

Figure 2-15 Calculated vdW force vs. asperity diameter

Another critical parameter affecting the vdW force is the asperity height, represented by the root-mean-square surface roughness value (RMS). It shows in Figure 2-16 that the vdW force is inversely proportional to the asperity height and again, increases with the asperity radius. Meanwhile, it is also found that when the surface asperity has more heterogeneous distribution, i.e. when the standard deviation of the asperity height increases, the vdW force decreases accordingly, as shown in Figure 2-17.

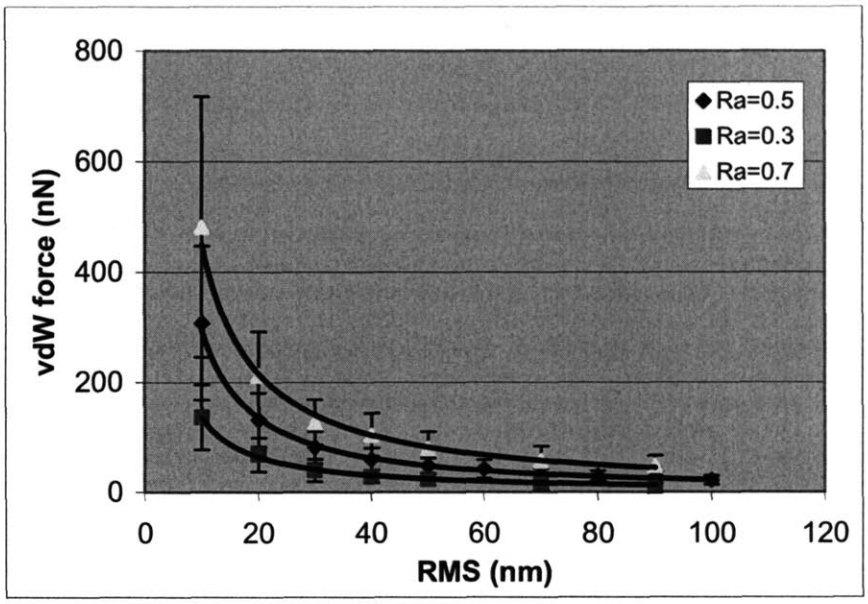

Figure 2-16 Calculated vdW force vs. asperity height

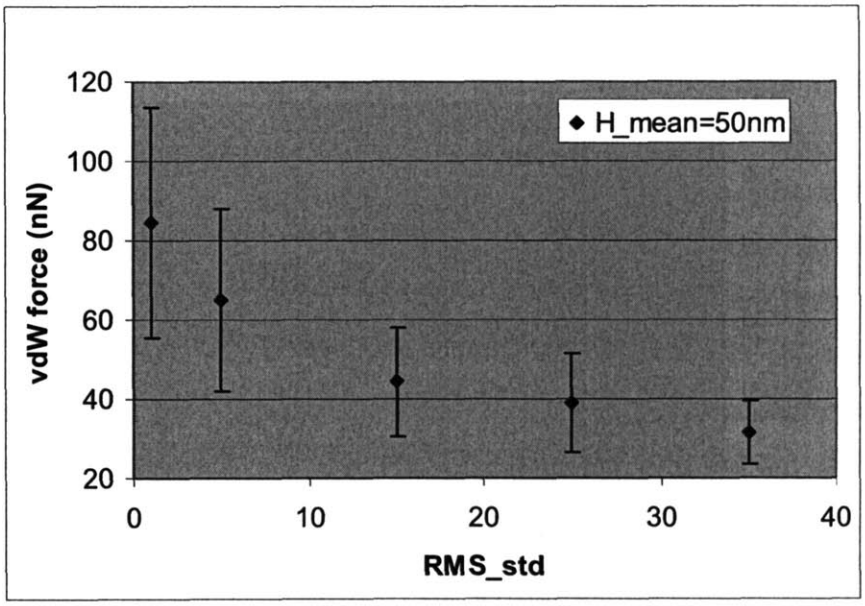

Figure 2-17 Calculated vdW force vs. standard deviation of asperity height

In addition to the asperity features, the vdW force also is affected by the asperity density on the particle surface, the Hamaker constant and the contact area. The simulation results indicates that the vdW force is linearly proportional to the Hamaker constant and also positively correlated with the asperity density and the contact area, as shown in Figure 2-18- Figure 2-20.

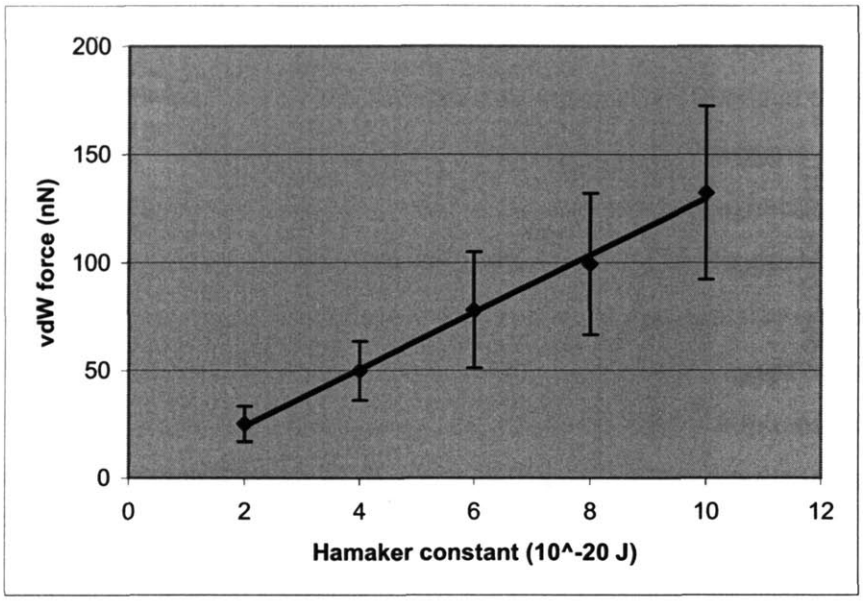

Figure 2-18 Calculated vdW force vs. Hamaker constant

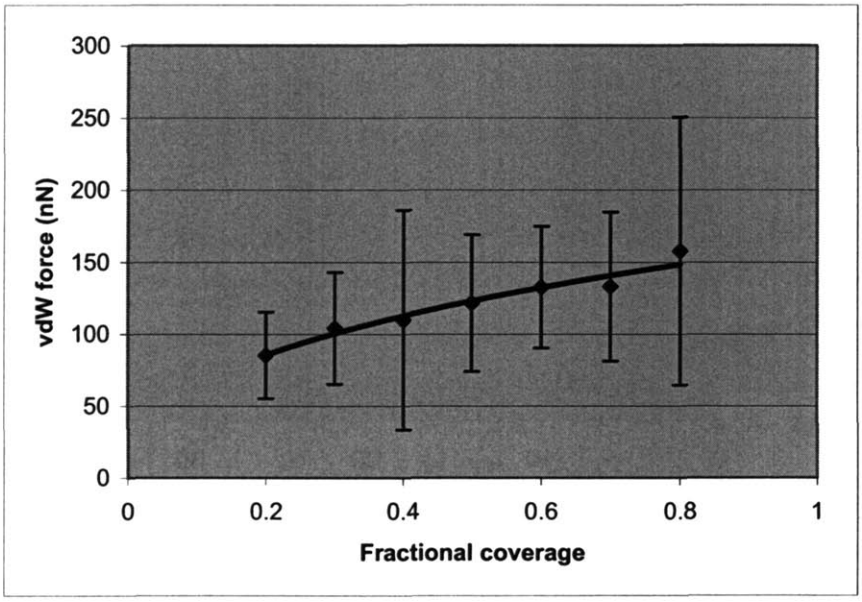

Figure 2-19 Calculated vdW force vs. fractional coverage of asperities

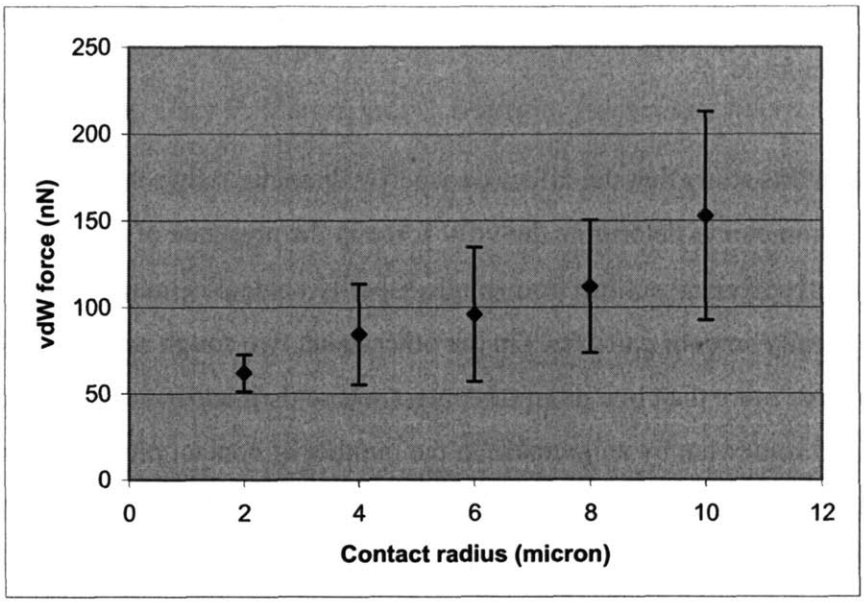

Figure 2-20 Calculated vdW force vs. radius of contact area

To summarize, for the particles with nanoscale roughness, the surface morphology has a significant effect on the van der Waals interaction forces. Given a set of surface morphological parameters, such as particle diameter, asperity radius, height and fractional coverage, etc., the vdW force between two single rough particles can be predicted by the surface element integration method. The calculated force value agrees well with the experimental results. In addition, from the parametric study based on the proposed van der Waals force model, it is found that the vdW force for rough particles is independent of the particle size at a certain size range. The key parameters which influence the vdW force are the asperity radius and height. The larger the asperity radius, the higher the vdW force is. The force is inversely proportional to the root-mean-square asperity height (RMS), and decreases as the asperity height distribution gets wider. Meanwhile, it is also positively correlated with the asperity density, the Hamaker constant and the contact area.

2.6 Discussions

Pharmaceutical powder particles normally are well covered by asperities. Because of the sensitivity of the van der Waals force to the surface geometry in the immediate neighborhood of the contact region, it is preferable to have the detailed surface features of any particle in the

contact region identified in order to obtain an accurate prediction of the magnitude of inter-particle adhesion force.

It is validated in this study that the effective asperity diameter rather than the particle diameter is the crucial parameter to determine the vdW force in the presence of this roughness. As a result, the attractive force resulting from single asperity contact is much smaller than that between two ideally smooth particles. On the other hand, two rough particles adhering to each other usually have more than one point of contact where their asperities meet. Thus the force may be elevated somewhat by an increase in the number of contact pints. Determining the net asperity effect requires characterization of the three-dimensional surface asperity features over the contact region, a task which is time consuming given the fact that no two powder particles have the same detailed surface morphology. The proposed model allows us to simulate as many contact surface geometries as necessary to achieve a statistical distribution of inter-particle van der Waals force. A lot of the tedious AFM surface characterization and force measurement can therefore be skipped.

Another factor to be considered is the surface change that takes place with processing. Due to the frictions and collisions between particles, especially for mixing process with intensive shear force, the attrition will occur to smooth out surface roughness of particles to some extent. To use the model to predict the effect of surface attrition on inter-particle vdW force will facilitate us to understand dynamics of powder flow behavior.

One limitation of the model is that particles in the simulation were assumed to be spherical or close to spherical. In fact, the effect of particle surface roughness on adhesion becomes more complex when the particle shape factor is taken into account. If interacting particles are angular or irregular in shape, physical inter-locking and/or mutual abrasion may take place, leading to change in surface morphologies. Mathematical models applicable for interactions of particles of any arbitrary shapes are desired in further studies.

2.7 References

1. Xian Ming Zeng, Gary P. Martin, and C. Marriott, *Particulate Interactions in Dry Powder Formulations for Inhalation.* 2001: Taylor & Francis Inc., London, UK.
2. H.C.Hamaker, *London-van der Waals Attraction between Spherical Particles.* Physica, 1937, **4**: 1058.
3. Howard Mizes, Mary OTT, and E. Eklund, *Small particle adhesion: measurement and control.* Colloids and Surface A: Physicochemical and Engineering Aspects, 2000, **165**: 11-23.
4. A.B.Yu, C.L.Feng, and R.P.Zou, *On the relationship between porosity and interparticle forces.* Powder Technology, 2003, **130**: 70-76.
5. Rumpf, H., *Particle Technology.* 1990: London; New York: Chapman and Hall.
6. Rabinovich, Y.I., et al., *Adhesion between nanoscale rough surfaces - I. Role of asperity geometry.* Journal of Colloid and Interface Science, 2000, **232**(1): 10-16.
7. Li, T.L. and K. Park, *Fractal analysis of pharmaceutical particles by atomic force microscopy.* Pharmaceutical Research, 1998, **15**(8): 1222-1232.
8. Beach, E.R., et al., *Pull-off force measurements between rough surfaces by atomic force microscopy.* Journal of Colloid and Interface Science, 2002, **247**(1): 84-99.
9. Forsyth, A.J. and M.J. Rhodes, *A simple model incorporating the effects of deformation and asperities into the van der Waals force for macroscopic spherical solid particles.* Journal of Colloid and Interface Science, 2000, **223**(1): 133-138.
10. Gotzinger, M. and W. Peukert, *Dispersive forces of particle-surface interactions: direct AFM measurements and modelling.* Powder Technology, 2003, **130**(1-3): 102-109.
11. Cooper, K., A. Gupta, and S. Beaudoin, *Simulation of particle adhesion - Implications in chemical mechanical polishing and post chemical mechanical polishing cleaning.* Journal of the Electrochemical Society, 2001, **148**(11): G662-G667.
12. Cooper, K., A. Gupta, and S. Beaudoin, *Simulation of the adhesion of particles to surfaces.* Journal of Colloid and Interface Science, 2001, **234**(2): 284-292.
13. Eichenlaub, S., A. Gelb, and S. Beaudoin, *Roughness models for particle adhesion.* Journal of Colloid and Interface Science, 2004, **280**(2): 289-298.
14. Cooper, K., et al., *Analysis of contact interactions between a rough deformable colloid and a smooth substrate.* Journal of Colloid and Interface Science, 2000, **222**(1): 63-74.
15. Bhattacharjee, S., C.H. Ko, and M. Elimelech, *DLVO interaction between rough surfaces.* Langmuir, 1998, **14**(12): 3365-3375.
16. K.J.Dong, R.Y.Y., R.P.Zou, et al. *Simulation of the cake formation and growth in sedimentation and filtration.* in *Third International Conference on CFD in the Minerals and Process Industries.* 10-12 December 2003. CSIRO, Melbourne, Australia.
17. Ahmadi, G., *Particle Transport, Deposition & Removal, On-line Curriculum.* http://www.clarkson.edu/projects/crcd/me437/notes/particle_adhesion/particle_adhesion_page6.html.
18. Beach ER, T.G., Drelich J, et al., *Pull-off force measurements between rough surfaces by atomic force microscopy.* Journal of Colloid and Interface Science, 2002, **247**(1): 84-99.

19. Ng, K.Y.F.a.K.M., *Product-centered Processing: Pharmaceutical Tablets and Capsules.* AICHE Journal, 2003, **49**(5): 1193-1215.
20. James T.Jenkins and M. Y.Louge, *Dense Inclined Flows: Theory and Experiments, Quarterly Technical Progress Report.* 1993.
21. A.N.Raegen, et al., *Measurement of adhesion energies and Young's modulus in thin polymer films using a novel axi-symmetric peel test geometry.* The European Physical Journal E, 2006, **19**: 453-459.
22. C.-Y.Wu, et al., *Modelling the mechanical behaviour of pharmaceutical powders during compaction.* Powder Technology, 2005, **152**: 107-117.
23. S.J.Eichhorn and R.J.Young, *The Young's modulus of a microcrystalline cellulose.* Cellulose, 2001, **8**(3): 197-207.
24. Roberts R.J., Rowe R.C., and Y. P., *The Poisson's ratio of microcrystalline cellulose.* International Journal of Pharmaceutics, 1994, **105**(2): 177-180.
25. Ackler, H. D., R. H. French, et al., *Comparisons of Hamaker constants for ceramic systems with intervening vacuum or water: From force laws and physical properties.* Journal of Colloid and Interface Science, **1996, 179**(2): 460-469

3 Electrostatic Force

3.1 Introduction

Most pharmaceutical powders are dielectric materials in nature and often are unavoidably charged during processing due to inter-particle and particle-wall collisions. The electrostatic force originated from the electrostatic charges is an important force component contributing to particle cohesion interactions.

When two dissimilar materials make and then break contact, charge transfer from one of the materials to the other occurs due to the difference in the work functions between the materials. Work function is defined as the minimum energy required to extract the weakest bound electron from a particle surface to infinity. For charge transfer of insulator/insulator contact to occur,electron donor or acceptor sites must exist at or near the insulator surface.

Basically there are three types of attractive electrostatic forces[1]: (1) Coulombic forces between particles of opposite charge, (2) polarization (image charge) forces between charged and induction-charged particles, and (3) electrostatic forces caused by contact potential differences because of different work functions. The last type of electrostatic force only occurs when two dissimilar and electrically conductive materials come into contact and a net flow of electrons arises. The electrostatic interactions between dielectric materials are usually described by the first two types. For insulators of any distance apart the electrostatic force can be calculated using Coulomb's formula as follows[2]:

1. Coulombic force

$$F_c = \frac{q_1 q_2}{4\pi\varepsilon_0 Z_0^{\ 2}} \tag{3.1-1}$$

2. Image charge force

$$F_i = \frac{q^2}{4\pi\varepsilon_0\varepsilon_r(d_p + 2Z_0)^2} \tag{3.1-2}$$

where q_1 and q_2 are the charges of the two particles in contact, ε_0 is the dielectric constant of free space, ε_r is the dielectric constant of the medium, d_p is the diameter of the particle and Z_0 the distance between the two charges.

Electrostatic charging due to triboelectrification is a stochastic and complicated process. Both polarities may arise randomly via charge exchange every time a particle makes contact with another. The electrostatic behavior is determined by both the intrinsic properties of materials/container surfaces and the external factors such as ambient relative humidity and the intensity and frequency of inter-particle collisions. Lots of work has been done in identifying various factors which affect the charging process. A summary of the most important particle properties of concern is given below:

1) Particle size and size distribution; Generally speaking, the work functions of large particles of a specific material will be lower than smaller particles and electron transfer from larger to smaller particles is favorable. Trigwell[3] and Cartwright[4] et al. found from their studies that fine particles tended to charge negatively while larger particles got positively charged. Thus a wide particle size distribution often resulted in bi-polar charging. In Murtomaa's experiments, charges were found always to be positive for samples of homogeneous particle size distribution[5, 6].
2) Relative permittivity or dielectric constant of the materials in contact; Materials having low values of permittivity (~2) tend to be electron acceptors and thus charge negatively when contacted by materials higher in the permittivity[7]. The dielectric constants of materials used in this research were found in literature and are listed in Table 3-1 for comparison.
3) Surface morphology; The rougher particles may acquire less surface charges due to the reduced surface contact area. However the charges concentrated on the peaks of asperities may cause a nonuniform distribution of surface charges and a high-localized electric field which results in a regional high interparticle force[1]. In contrast, homogeneous particle morphology show a good reproducibility in their specific charges[5, 6].

4) Surface composition or surface contamination of the material; for example, amino and hydroxyl group on the surface are usually electron donors while carbonyl and halogen group are electron acceptors. As mentioned later, water molecule absorbed on the surface sometimes also changed the charging behavior significantly.

Table 3-1 Dielectric constants of materials used in research

Material	Dielectric Constant
Air	1[8]
Polystyrene	2.6[8]
Glass	4.8[8]
Lactose	3.68[9]
Cellulose	3.9[8]
Caffeine	N/A
Water	80[8]
Steel	330[10]

5) Crystallinity of the material; Samples of high crystallinity show a good reproducibility in their specific charges, whereas amorphous samples tend to acquire higher charge in virtue of their larger surface area[5, 6].
6) Moisture sorption properties of particle materials. Generally the charge retention can be reduced by increasing the moisture to enhance the conductivity. Nonetheless experimental evidence showed that increase in moisture could increase, decrease, or have no effect on the charging of solids, depending on the moisture sorption properties of particle materials. For low hygroscopic materials such as lactose, the charge variation with relative humidity is not obvious, while for highly hygroscopic materials, the electrostatic charge behavior becomes more complex and less predictable, as found in Rowley's work[11].

In practice, the electrostatic charge is very difficult to measure and even more difficult to predict. The measurement and the modeling of electrostatic charges and electrostatic forces between particles will be presented in the following sections.

3.2 Measurement of surface charge and charge distribution

Measurement of triboelectrification is difficult and poorly reproducible for several reasons. First of all, being a very surface sensitive process, charge generation and transfer may vary as a result of heterogeneity of physical/chemical properties of material surface. Even for the different samples of nominally the same material, the triboelectric behavior may be quite different due to surface impurity[12]. Secondly, charge propensity depends heavily on the contact history in which the contact pressure, area, time and frequency are usually unknown and difficult to quantify. Thirdly, the collision event of powder particles is usually of very short duration so that there is insufficient time for the charge transfer process to attain equilibrium.

Methods of electrostatic charge measurement are referred to as two kinds: static and dynamic. The typical static measurement of particle charge is the Faraday Cage, also called Faraday Pail or Faraday Cup. When charged particles pass through a Faraday Cage, an induced charge will be developed. Particle charge and induced charge will be equal and opposite according to Gauss' theorem. By connecting the Faraday Cage to an electrometer, the amount of charge can be detected. The main drawback of this method is that only net charge of a population of particles can be measured without indicating the portions of powders of different polarities. Nonetheless, Faraday cup is still commonly used for quantifying electrostatic interactions in pharmaceutical solid systems[13, 14] and processes such as spray drying[5] due to its quick and easy operation. Other static techniques include vertical cascade array Faraday pail sensors to measure bipolar charge in polydisperse powders[15] and electrical low-pressure impaction to characterize electrostatic charge of pharmaceutical aerosols[16].

In contrast to the static measurement, the dynamic approaches measure the electrical mobility of particles instead of the absolute charges. One method is to measure the dynamic movement of charged particles in a high electric field and relate the velocity of the particles to their

electrostatic charge. The typical instruments used are different types of electric mobility analyzers, including recently developed electrostatic spectrometer[17]. Similarly, in the application of the electrostatic charge separator[18] and the Bipolar Charge Measurement System (BCMS)[19], the external electric field is applied between two electrode plates and the particles are separated and collected on the two electrode plates based on their polarities. The charge-to-mass ratios for both positively and negatively charged powder fractions are measured accordingly. Another approach is to measure the phase-lag and the amplitude ratio of the oscillation of the particle with respect to an AC electric drive at a certain frequency. The device developed based on this principle is called Electronic Single Particle Aerodynamic Relaxation Time (E-SPART) analyzer, which allows the real-time analysis of size and charge distribution of airborn particles on a single-particle basis[1]. The main disadvantages of these methods are the long sampling time, the high electric field required and the particle size constraints.

Although a number of devices have been developed for the electrostatic charge measurement, no single device or system has been well accepted to be widely used, nor can any of them characterize the detailed charge distribution on individual particles. In our study charging properties of both bulk powders and individual particles were investigated by multiple techniques.

3.2.1 Charge measurement on bulk powders

In our experiments, lactose powders first were sieved into four different size groups. The narrowed particle size distribution helped improve the reproducibility of the measurement and reduce the data variance. Each group was loaded into a rotating stainless steel blender. Every two to five minutes a small amount of sample powders were taken out from the paused blender using a grounded spatula. The electrostatic charges of sample powders were measured by the Faraday cup technique (Model 210-HS system, Trek Inc., USA) and the mass was weighed (Model AX-105, Mettler Toledo, Switzerland). The charge to mass ratio of lactose powders was calculated subsequently. Likewise the charging property of MCC powders was measured in the same way. The Q/m ratio variations with blending time of both powders were shown in Figure 3-1 and Figure 3-2.

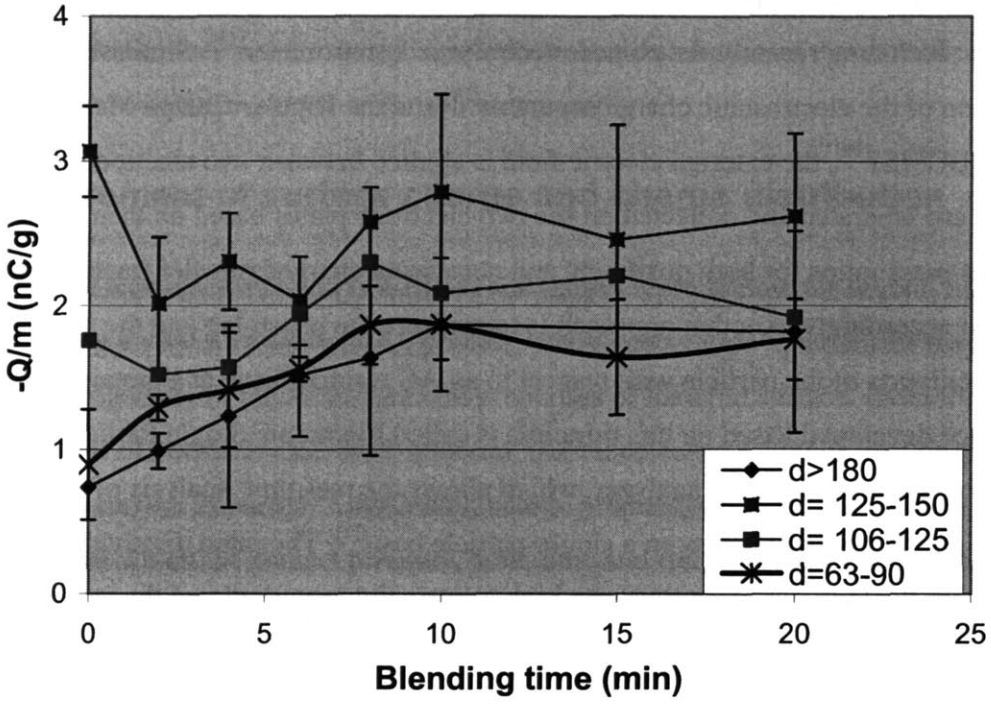

Figure 3-1 Electrostatic charge build-up with the blending time for lactose particles

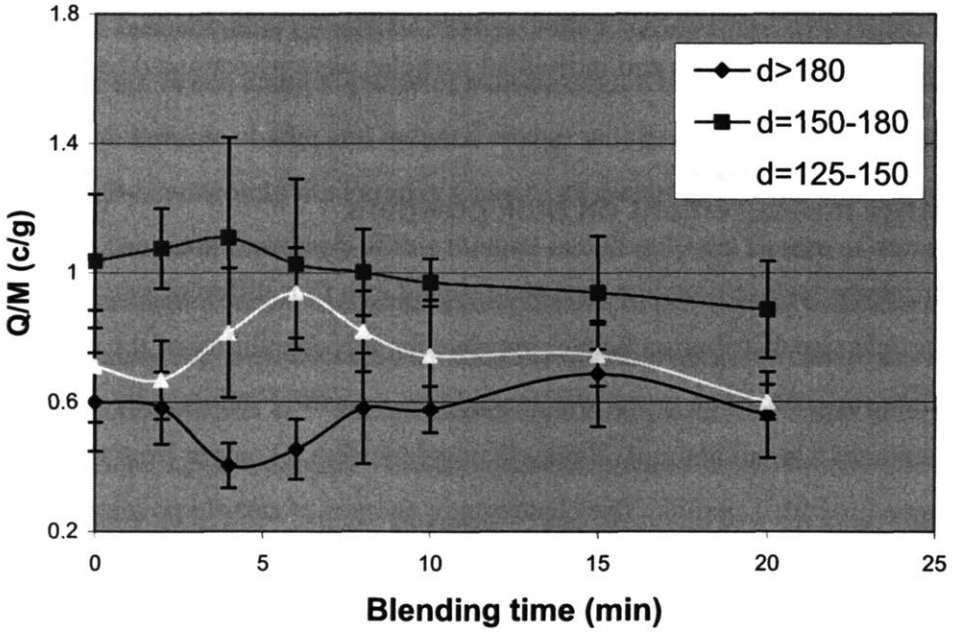

Figure 3-2 Electrostatic charge build-up with the blending time for MCC particles

It is seen that the charge-to-mass ratio of the powder samples increased with the blending time and then attained a saturated value or decayed to some extent after a certain period of time,

suggesting that electrostatic charge generation, accumulation and dissipation take place simultaneously during the blending process. It also was found that the Q/m ratio of particles increases with the particle size when the particle size is relatively small. However when the particle size is beyond 180 μm, the Q/m ratio went down to the level as low as observed for the particle group of the smallest size. A similar trend was observed in Rowley's work[13]. A possible reason for this phenomenon is that, when particle size is very small, particles tend to adhere on the equipment surface, while when particle size is relatively large, the absolute number of particles in the unit mass is fewer than particle groups of smaller size. In both cases, the chances of particle contact and collision is reduced, which results in a lower Q/m value. Another interesting phenomenon observed in the experiments is that the lactose particles tend to carry negative charges varying from -0.6 nC/g to -3 nC/g, while the MCC particles tend to gain lower positive charges of 0.4-1.4 nC/g. A full explanation for this difference cannot be given unless an in-depth investigation on charging mechanism is carried out in further studies.

In a word, the triboelectrification of powders in process is a complex problem which is affected by material properties, contact surface properties and many other factors. As a consequence, charge measurement of bulk powders often shows a poor reproducibility if without a tight control of the material and the environmental conditions. For this reason, it is not surprising to see that some conclusions on electrostatic charging are inconsistent or even contradictory to previous studies.

3.2.2 Charge measurement on single particles

As mentioned earlier, the Q/m ratio measured with Faraday cup only reflects the net charges of a powder population. To quantify electrostatic interactions between individual particles, it is desirable to understand electrostatic charging behavior of a single particle. Mapping electrostatic charge distribution on a single particle gives us some insightful information.

In the experiments, surface potential imaging was carried out on a single lactose particle using electric force microscopy (EFM). The EFM used in the experiments was an atomic force microscopy (Dimension 3100, Veeco Instrument, USA) equipped with the Extender Electronics Module. During the measurement, a voltage of 6 Volts was applied to a

conductive magnetic coated probe (MESP, Veeco Probes, USA), and the particle to be measured was fixed on a grounded sample plate using a conductive tape. The charged tip first scanned the particle surface under the Tapping mode and topographical data was obtained from this first pass. The tip then ascends to lift scan height and a second scan performed while maintaining a constant separation between the tip and local surface topography. Since the oscillating force on the cantilever depends on the product of the ac drive voltage and the dc voltage difference between the tip and the sample, the Extender Electronics Module uses this fact to adjust the dc voltage on the tip till the oscillation amplitude becomes zero. The local surface potential of the particle is thus determined in this way.

Figure 3-3 shows the height image and the surface potential image of a lactose particle obtained from the EFM measurement. Since the surface potential varies with the magnitude of surface charges, the surface potential image demonstrated the surface charge distribution intuitively. Unfortunately, because the system was not calibrated on a sample at a known voltage, the absolute surface potential or surface charge values cannot be calculated from the measurement. Interestingly, the higher potential level was observed to coincide primarily with protruded topographical features, which implied that the surface charge distribution may be affected by the surface topography predominantly. This correlation between surface potential image and the height image was also addressed in Machowski's work[20]. As pointed out in Yurteri's work[1], When two particles with surface asperities contact with each other, the generated electrostatic charges tend to concentrate on the peaks of asperities, causing a nonuniform surface charge distribution. The EFM images confirmed the heterogeneity of surface charge distribution and its correlation with the surface morphological heterogeneity.

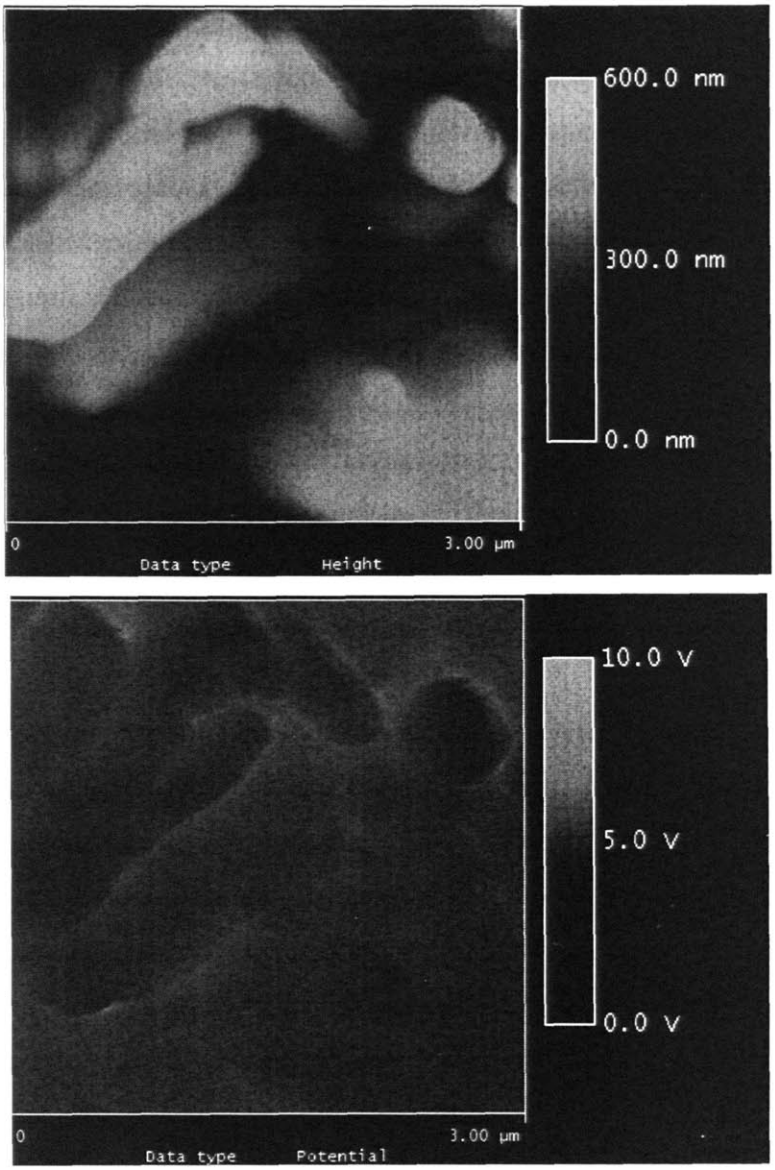

Figure 3-3 The height image (top) and the surface potential image (bottom) of lactose particle obtained from the EFM

3.3 Measurement of inter-particle electrostatic force

In addition to the charge measurements, application of AFM for the quantification of the electrostatic force between individual particles became popular in recent years. As early as in 1990, Hao and his colleagues[21] measured the electrostatic force between a tip and a graphite surface in an AFM, with an applied voltage on the AFM tip. Similarly in Mizes' work[22], a transparent electrode was placed above the AFM cantilever and an electric field was applied

across a particle. The adhesion force change as a function of the electric field strength was examined. However, the voltage applied on the tip may create artifacts in the surface charge distribution and make measured electrostatic force excessively large. Alternatively, electrostatic force interaction was identified from noncontact force gradient data by measuring the amplitude of an oscillating cantilever as a function of driving frequency[23]. The method is not widely used because of the complexity of converting amplitude vs. frequency data to the more intuitive force vs. distance data.

In our work, the AFM force measurement was carried out between two single particles as described in Section 1.3. No external electrical field or voltages were applied during the measurement. The relative humidity inside the AFM chamber was kept low by dry nitrogen gas to avoid charge dissipation. Since van der Waals force is always present in particle interactions, it is impossible to quantify the magnitude of electrostatic force directly from the force curve. However, the presence of surface charges, if high enough, will affect the shape of the force curve significantly. A typical AFM force curve for particles carrying charges is shown in Figure 3-4. When the tip-sample distance is beyond a few nanometers, the effect of van der Waals force becomes negligible. The change of cohesion force as a function of the tip-sample distance in the longer range is attributed mainly to electrostatic force between the particles. By using appropriate models to fit the force curve, the magnitude of electrostatic charge and electrostatic force can be determined. The modeling work of inter-particle electrostatic force is presented in the next section.

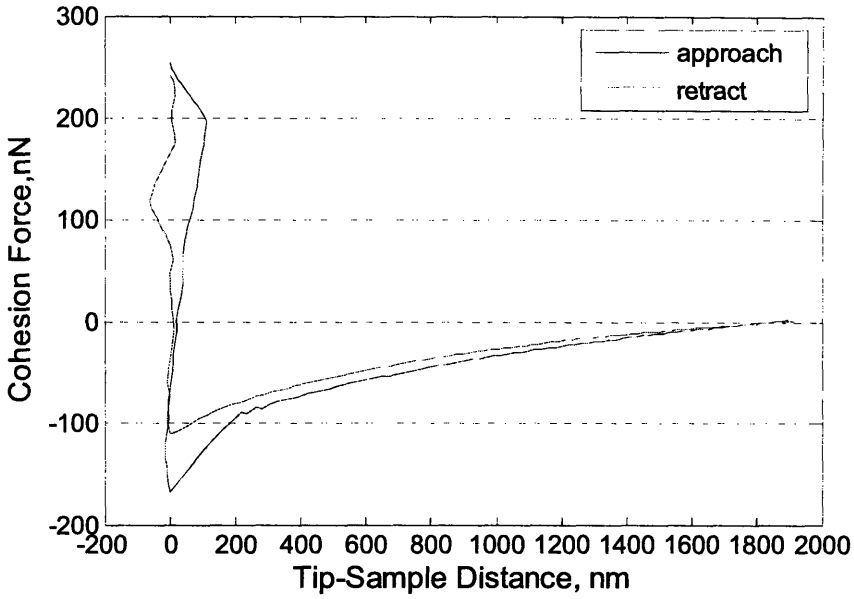

Figure 3-4 AFM Force curve of a lactose particle carrying surface charges brought into contact with another single lactose particle adhered on the silicon nitride cantilever

3.4 Modeling of inter-particle electrostatic force

3.4.1 Introduction

Coulomb's law is the established fundamental law for electrostatic interactions. Therefore, if we know or predict the amount of charge generated on a particle, we can determine the electrostatic force working on the particle, and vice versa. With this knowledge at hand, we may conduct a better control on electrostatic force. As described in Section 1.2 and 1.3, electrostatic force between single particles is not separable from the van der Waals force in the AFM force measurement. Besides, no absolute value of surface charges but the average net charges of assembles of particles and relative surface charge distribution can be obtained via the experimental approaches. Under such circumstances, the aid of appropriate mathematical models turned out to be an effective way to explore the relationship between electrostatic force and particle properties such as particle size, surface charges, dielectric constant of the particle material and the distance between the two contacting particles.

Up to now, a lot of models have been developed to describe electrostatic interactions. Some used numerical and computational approaches such as boundary element method solving the

linearized Poisson-Boltzmann equation[24], finite element method[25, 26], and Laplace's equation representing the potential distribution[27]. Most of them are very complicated algorithms and only applicable to contact of an insulating particle to a conducting substrate rather than two dielectric particles in contact. In this case, a more widely used approach called the method of image charge was applied in our modeling work for its simplicity.

The method of image charge is a basic problem-solving tool in electrostatics. In terms of a problem of one or more point charges in the presence of boundary surfaces, the required boundary conditions can be simulated by some imaginary image charge suitably placed external to the region of interest. By solving the potential equations with given geometry, the magnitude of image charge can be determined. The derivation and the application of this method is described in many classic textbooks[28, 29] in detail and is not addressed here.

The electrostatic force between a spherical alumina particle and a flat alumina substrate was studied with the image charge method by Zhou and his coworkers[30]. Although the proposed model is based on conducting metal materials instead of dielectric ones, one thing of interest to our study is the point charge approximation in his work, i.e. the charge distribution on the particles was approximated by a point charge in the vicinity of the contact surface and a mean point charge in the center of the particle, and the total force was represented as the sum of the image forces introduced by these two point charges.

In Burnham's work, electrostatic force was called patch charge force to reflect the non-uniform distribution of electrostatic charges. The AFM tip and the graphite surface were modeled as an insulating sphere and an infinite flat substrate. Based on image charge method and Coulomb's law, the electrostatic force was expressed as[31]:

$$4\pi\varepsilon_3\varepsilon_0|F_{es}| = -\frac{Q_t^2}{4(D+A)^2}\left(\frac{\varepsilon_2-\varepsilon_3}{\varepsilon_2+\varepsilon_3}\right)+\frac{BQ_tQ_s}{Z(2D+A+B)^2}\left(\frac{\varepsilon_1-\varepsilon_3}{\varepsilon_1+\varepsilon_3}\frac{\varepsilon_2-\varepsilon_3}{\varepsilon_2+\varepsilon_3}\right)$$
$$+\frac{2Q_tQ_s}{Z^2}\left(1+\frac{1}{\varepsilon_1+\varepsilon_3}+\frac{2}{\varepsilon_2+\varepsilon_3}\right)-\frac{2BQ_s^2}{Z^3}\left(\frac{\varepsilon_1-\varepsilon_3}{\varepsilon_1+\varepsilon_3}\right) \quad (3.4\text{-}1)$$

where D is the distance between tip and sample, Q_t and Q_s are the charges on the tip and the sample, ε_1,ε_2 and ε_3 are the relative dielectric constants of tip, sample and medium,

respectively. Z, A and B are the fitting parameters representing the distances of fields. As seen from equation (3.4-1), the first term in the equation, which is due to the interaction of Q_t and its image, always is attractive. As D is decreased, the first term increased in magnitude faster than the second term, and the net force becomes attractive.

A few years later, Guerret-Piecourt et al[32] simplified the aforementioned model for two similar materials with same dielectric constant in the form of:

$$4\pi\varepsilon_0 F = -\frac{Q_t^2}{4(D+A)^2}\left(\frac{\varepsilon-1}{\varepsilon+1}\right)+\frac{RQ_tQ_s}{Z(2D+A+R)^2}\left(\frac{\varepsilon-1}{\varepsilon+1}\right)^2 \qquad (3.4\text{-}2)$$

Although developed for the case of a sphere contacting with an infinite flat plate, the models enlightened us to extend the application of the method of image charges to model electrostatic force between two dielectric spheres. The details are described in the next section.

3.4.2 Modeling of electrostatic force between two dielectric particles

When the method of image charge was applied to model the electrostatic force between two interacting charged dielectric particles, several assumptions were made to simplify the problem: Firstly, the particles were regarded as ideal smooth spheres because the length scale of nanometer surface asperities is much smaller than the range of particle distance to be considered; secondly, it is assumed that the all the charges are distributed only in the contact area instead of the whole particle surface. Thus the charges on the particle were represented as a point charge; thirdly, multiple inductions between the spheres were neglected because image charge is usually much lower than the corresponding original charge.

In the case of a point charge q a distance d away from a dielectric surface, the field of the point charge q will polarize the dielectric and there will therefore be a surface image charge q_t on the dielectric which affects the field outside. Meanwhile the field within the dielectric is represented by a second image system, here denoted as a point charge q'. To avoid an infinite electric field at the boundary, the potential must be the same on either side of the boundary, which states the first boundary condition. To assure that the normal component of the field be continuous at the boundary, the gradient of the potential on the normal direction must be the same on either side of the boundary, which sets for the second boundary condition. By solving

the potential equation based on the two boundary conditions, the positions and the magnitudes of the image charges q_t and q' can be determined.

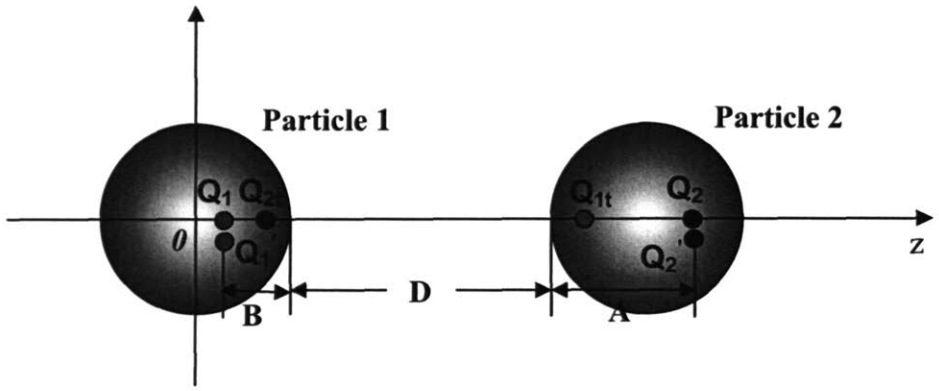

Figure 3-5 Schematic of point charge method between two dielectric spheres

As illustrated in Figure 3-5, particle 1 carries a point charge Q_1 a distance A within the particle surface, particle 2 carries a point charge Q_2 a distance B within the surface. The distance between the two particles is D. Analytical solutions for the image charge induced by a point charge near to a dielectric sphere has been derived in previous work[31, 33, 34] and used directly in our model. The positions and the magnitudes of the image charge Q_{1t}, Q_{2t} and the induced charge Q_1', Q_2' were obtained as:

$$Q_{1t} = -\frac{R_2}{R_2 + D + B} Q_1 \cdot \frac{\varepsilon_2 - \varepsilon_3}{\varepsilon_2 + \varepsilon_3}, \text{ at position } R_1 + R_2 + D - \frac{R_2^{\,2}}{B + D + R_2};$$

$$Q_1' = \frac{2Q_1}{\varepsilon_2 + \varepsilon_3}, \text{ at position } R_1 - B;$$

$$Q_{2t} = -\frac{R_1}{R_1 + D + A} Q_2 \cdot \frac{\varepsilon_1 - \varepsilon_3}{\varepsilon_1 + \varepsilon_3}, \text{ at position } \frac{R_1^{\,2}}{R_1 + D + A};$$

$$Q_2' = \frac{2Q_2}{\varepsilon_1 + \varepsilon_3}, \text{ at position } R_1 + D + A$$

Where ε_1,ε_2 and ε_3 are the dielectric constant of particle 1, particle 2 and the medium, respectively; R_1 and R_2 are the radius of particle 1 and 2, respectively.

When the two particles are of the same material and placed in air, as in our case, $\varepsilon_1=\varepsilon_2=\varepsilon=3.68$ for lactose particles and $\varepsilon_3=1$. Also the particle radius $R_1=R_2=R=100$ μm. The Coulomb forces arisen from the charge pairs Q_1-Q_2, Q_1-Q_{1t}, Q_1-Q_1', Q_2-Q_{2t}, Q_2-Q_2' can be

obtained based on the Coulomb's law. The electrostatic force between the two particles is the sum of all the Coulomb forces contributed by the charges and their fields, expressed as:

$$F = K_e \left[\begin{array}{l} -\dfrac{CQ_1^2 R(R+D+B)}{(2R+D+B)^2(D+B)^2} + \dfrac{2Q_1Q_2}{(D+A+B)^2} + \dfrac{4Q_1Q_2/(\varepsilon+1)}{(D+A+B)^2} \\ -\dfrac{CQ_2^2 R(R+D+A)}{(2R+D+A)^2(D+A)^2} \\ +\dfrac{C^2R^2Q_1Q_2}{(2R+D)(R+D+A)(R+D+B)-R^2(2R+2D+A+B)} \end{array} \right] \quad (3.4\text{-}3)$$

where K_e=1/(4$\pi\varepsilon_0$)=9×10^{12} N·m^2/C^2, C=(ε-1)/(ε+1), Q_1, Q_2, A and B are the four unknown parameters representing the magnitude and the position of the charges on the two particles.

From the AFM force measurements we captured cohesion force data as a function of the tip-sample distance. Since van der Waals force is a short-distance force relative to the electrostatic force, it is negligible when the tip-sample distance is much larger than 0.4 nm. Therefore, the cohesion force beyond that range can be regarded as mainly contributed from long-distance electrostatic force. In other words, the electrostatic part of the cohesion force can be determined from the noncontact part of the force-distance plot. A MATLAB code was developed to fit the attractive force data in the pre-contact region of the approach force curve with the electrostatic force model proposed above, and the unknown parameters was determined from the fitting results.

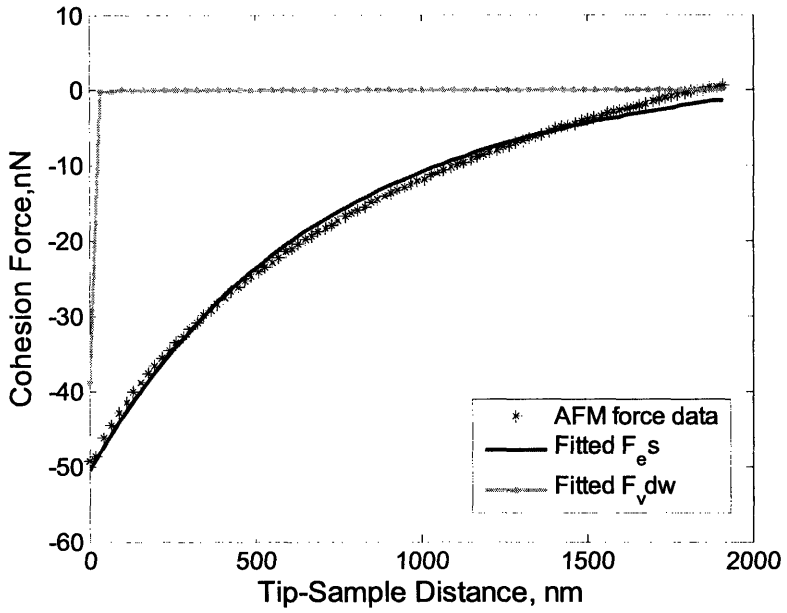

Figure 3-6 AFM approach force curve fitted by the electrostatic force model

As shown in Figure 3-6, the best fitting parameters were found when the calculated electrostatic force curve (solid line in red) agreed well with the force curve measured with the AFM (dot line in blue). The average asperity height is around 100~200 nm, much shorter than the tip-sample distance of 500~1500 nm. The van der Waals force (solid line in green) in this range was negligibly low compared to the total cohesion force. The values of fitted parameters were: Q_1=2.05×10^{-9} nC, Q_2=6.06×10^{-6} nC, A=1500 nm and B=1000 nm.

3.4.3 Results and discussion of the electrostatic force modeling

It was found from the values of A and B that both charges were located very close to the surface area where the two particles come into contact. Similar results were confirmed in Zhou's work, which stated that the magnitude of the electrostatic interaction force depends strongly on the local charge distribution in the vicinity of the contact area. In terms of the values of Q_1 and Q_2, Q_1 is three order-of-magnitudes smaller than Q_2, which can be explained by the particular way the experiment was conducted. Particle 1 is the particle adhered on the tip of the cantilever. It appeared to have much lower surface charges than particle 2 because its electrostatic charges dissipated to a great extent during the long storage time of the

prepared cantilever prior to the experiments, whereas particle 2 was the sample particle freshly picked up right before the experiment and insulated from the sample plate using a non-conductive tape so that a certain amount of electrostatic charges were still retained on the particle and did not dissipate easily during the force measurement.

The remaining question is whether the fitted charge value is physically meaningful. First of all, we checked it with the upper limit of surface charge allowed for a single particle. There are fundamental limits on the maximum amount of charge that can be acquired by a particle of a given size. For charged solid particles, the maximum charge is reached when the self-generated field at the surface of a particle meets the value required for spontaneous emission of electrons from a surface. When this limit is exceeded, the crowding of electrons on the surface of the particle causes electron to be ejected from the particle by the force of mutual repulsion. For spherical particles, this limit is[38]

$$Q_{\max} = \frac{d_p^2 E_L}{4K_e} \tag{3.4-4}$$

where E_L is the surface field strength required for spontaneous emission of electrons, d_p is the diameter of the particle and $K_e=1/(4\pi\varepsilon_0)=9\times10^{12}$ N·m^2/C^2.

For negatively charged particles, E_L is 9.0×10^8 V/m. For positively charged particles, E_L is as large as 2.1×10^{10} V/m because emitting a positive ion is a more difficult process and requires a greater surface field strength. Obviously the charge limit is proportional to the surface area of the particle, as expected. A simple calculation on a particle of 100 μm in diameter indicates that the maximum charge value is 2.5×10^{-4} nC if it is negatively charged and 5.8×10^{-3} nC if it is positively charged. The fitted charge values as expected are much lower than this limit.

Second, the fitted value was compared to the charge value measured with the Faraday cup in our previous experiments. The charge-to-mass ratio of lactose particles was in the range of 0.7~3 nC/g. Given the bulk density of lactose powders is 0.678 g/cm^3, and assume the tested lactose particles have uniform particle diameter of 100 μm, the electrostatic charge on a single particle is estimated to be $0.25\text{-}1.06\times10^{-6}$ nC, which is lower than the fitted value but in the

same magnitude. On the other hand, the surface charge density calculated based on the fitted charge value is about 1.9×10^{-1} C/m^2. There was no report of the experimentally measured charge density data of lactose particles for verification. Nevertheless, the reported charge density of different materials were in the order of magnitude of $10^{-4} \sim 10^{-2}$ C/m^2 [31, 32, 35, 36], comparable to our results.

Since the fitted surface charge value is reasonable, the model was further utilized to fit the experimental data collected from the AFM force volume measurement. For one pair of particles, with the AFM force volume mode, a total of 256 approach force curves and 256 retract force curves were captured for 16×16 spots over the scanning area of 5×5 μm^2 in one measurement. The same fitting process was implemented on all the 256 approach force curves and a set of fitting parameter values were obtained. The charges on the scanning surface of particle 1 were found to be in the range of $5.31\sim7.69\times10^{-6}$ nC, while the charge range for particle 2 was $1.04\sim2.13\times10^{-9}$ nC. The charge distribution over the scanning area appeared to be close to the logarithm normal distribution, as shown in Figure 3-7. Coincidently, it was found in previous work[37] that the cohesion force distribution over a scanning area also followed a logarithm normal distribution. Comparing the cohesion force distribution and the surface charge distribution on the same scan area, as seen in Figure 3-8, we found a correspondence between the surface charge and the cohesion force, i.e. the spot with higher surface charges overlapped with the spot with higher cohesion forces to some extent. This implied that existence of surface charges have impact on the particle cohesion interactions.

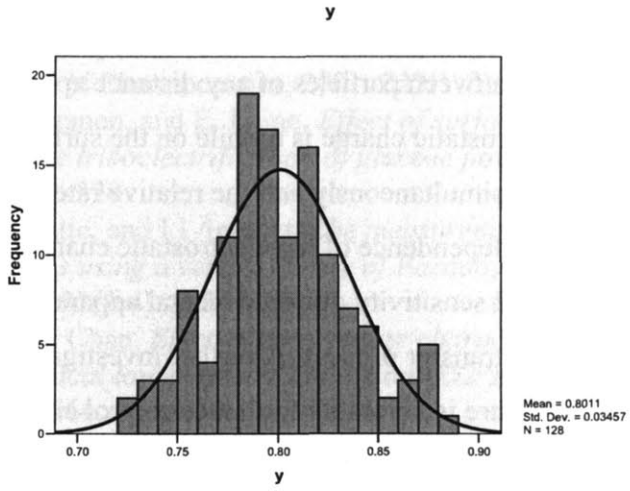

Figure 3-7 Electrostatic charge distribution over the scan area of particle surface

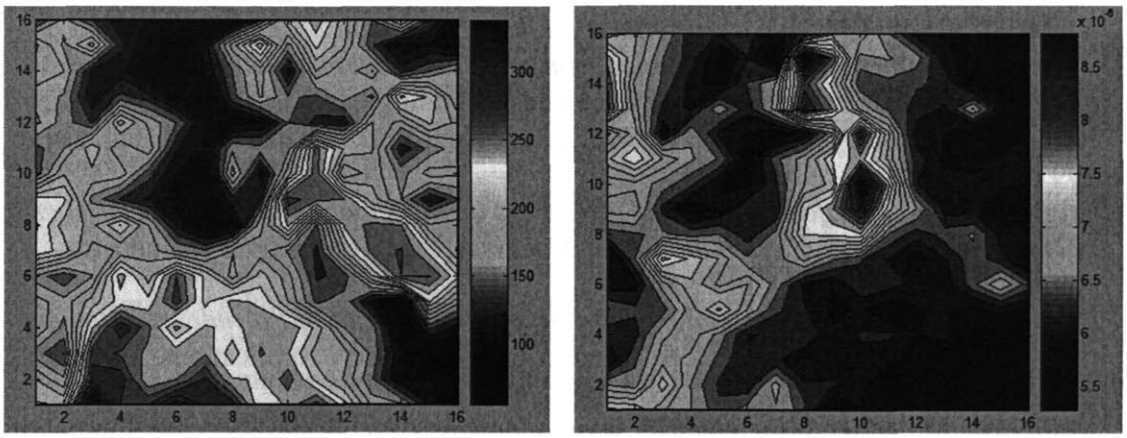

Figure 3-8 Surface map of cohesion force distribution (left) and charge distribution (right)

3.5 Discussions

Electrostatic charge and electrostatic force on pharmaceutical powder particles were studied by experimental approaches and theoretical modeling. The magnitude of surface charge on a single particle was quantified to be in the order of 10^{-6} nC, comparable to the result from Faraday cup measurements. The surface charge distribution was mapped from both the EFM surface potential measurement and the modeling results. It showed that surface charge distribution was affected by the surface morphological heterogeneity and on the other hand, affected the cohesion force distribution on the particle surface.

With the quantification of electrostatic charges on single particles and the model, the electrostatic attractive forces between particles of any distance apart can be estimated. However, in practice the electrostatic charge is mobile on the surface. Charge generation, transfer and dissipation occur simultaneously and the relative rates of these processes fluctuate over time. The time dependence of the electrostatic charges was not taken account of in our model due to the limited sensitivity of experimental apparatus to detect the uncertainty and variability of the electron transfer process. A further investigation of the dynamics of electrostatic charges in the future is favorable for better control and prediction of the electrostatic charging behavior of processed powders.

3.6 References

1. Yurteri, C.U., et al., *Electrostatic effects on dispersion, transport, and deposition of fine pharmaceutical powders: Development of an experimental method for quantitative analysis.* Particulate Science and Technology, 2002. **20**(1): p. 59-79.
2. Rumpf, H., *Particle technology.* 1990, London; New York: Chapman and Hall. xiv, 199 p.
3. Trigwell, S., et al., *Effects of surface properties on the tribocharging characteristics of polymer powder as applied to industrial processes.* Ieee Transactions on Industry Applications, 2003. **39**(1): p. 79-86.
4. Cartwright, P., et al., *Electrostatic Charging Characteristics of Polyethylene Powder during Pneumatic Conveying.* Ieee Transactions on Industry Applications, 1985. **21**(2): p. 541-546.
5. Murtomaa, M., et al., *Static electrification of powders during spray drying.* Journal of Electrostatics, 2004. **62**(1): p. 63-72.
6. Murtomaa, M., et al., *Effect of amorphicity on the triboelectrification of lactose powder.* Journal of Electrostatics, 2002. **56**(1): p. 103-110.
7. Bailey, A.G., *Electrostatic Phenomena During Powder Handling.* Powder Technology, 1984. **37**(JAN-): p. 71-85.
8. *DIELECTRIC CONSTANTS OF VARIOUS MATERIALS.* from the Delta Controls Corporation company website: http://www.deltacnt.com/99-00032.pdf.
9. Herman (EDT) Vromans and A. Muñoz-Ruiz, *Data Acquisition and Measurement Techniques.* 1997: CRC Press, p.132.
10. Zou, Q., H.E. Ruda, and B.G. Yacobi, *Improved dielectric properties of lead zirconate titanate thin films deposited on metal foils with LaNiO3 buffer layers.* Applied Physics Letters, 2001. **78**(9): p. 1282-1284.
11. Rowley, G. and L.A. Mackin, *The effect of moisture sorption on electrostatic charging of selected pharmaceutical excipient powders.* Powder Technology, 2003. **135**: p. 50-58.

12. Lowell, J. and A.R. Akande, *Contact Electrification - Why Is It Variable.* Journal of Physics D-Applied Physics, 1988. **21**(1): p. 125-137.
13. Rowley, G., *Quantifying electrostatic interactions in pharmaceutical solid systems.* International Journal of Pharmaceutics, 2001. **227**(1-2): p. 47-55.
14. Murtomaa, M., K. Ojanen, and E. Laine, *Effect of surface coverage of a glass pipe by small particles on the triboelectrification of glucose powder.* Journal of Electrostatics, 2002. **54**(3-4): p. 311-320.
15. Zhao, H., G.S.P. Castle, and I.I. Inculet, *The measurement of bipolar charge in polydisperse powders using a vertical array of Faraday pail sensors.* Journal of Electrostatics, 2002. **55**(3-4): p. 261-278.
16. Glover, W. and H.K. Chan, *Electrostatic charge characterization of pharmaceutical aerosols using electrical low-pressure impaction (ELPI).* Journal of Aerosol Science, 2004. **35**(6): p. 755-764.
17. R.C.Brown, *Tutorial review: simultaneous measurement of particle size and particle charge.* Journal of Aerosol Science, 1997. **28**(8): p. 1373-1391.
18. Mountain, J.R., et al., *Triboelectric charging of polymer powders in fluidization and transport processes.* Ieee Transactions on Industry Applications, 2001. **37**(3): p. 778-784.
19. Balachandran, W., et al., *Bipolar charge measurement of pharmaceutical powders.* Powder Technology, 2003. **135**: p. 156-163.
20. W.Machowski, P.B.a.W.B. *Study of ELectrostatic Properties of Dielectric Surfaces and Powders Using Scanning Probe Microscopy.* in *Industry Applications Conference, 1999. Thirty-Fourth IAS Annual Meeting. Conference Record of the 1999 IEEE.* 1999. Phoenix, AZ.
21. Hao, H.W., A.M. Baro, and J.J. Saenz, *Electrostatic and Contact Forces in Force Microscopy.* Journal of Vacuum Science & Technology B, 1991. **9**(2): p. 1323-1328.
22. Mizes, H., et al., *Small particle adhesion: measurement and control.* Colloids and Surfaces a-Physicochemical and Engineering Aspects, 2000. **165**(1-3): p. 11-23.
23. Gady, B., et al., *Identification of electrostatic and van der Waals interaction forces between a micrometer-size sphere and a flat substrate.* Physical Review B, 1996. **53**(12): p. 8065-8070.
24. Sun, N. and J.Y. Walz, *A model for calculating electrostatic interactions between colloidal particles of arbitrary surface topology.* Journal of Colloid and Interface Science, 2001. **234**(1): p. 90-105.
25. Tang, T., C.Y. Hui, and A. Jagota, *Adhesive contact driven by electrostatic forces.* Journal of Applied Physics, 2006. **99**(5): p. -.
26. Feng, J.Q., *Electrostatic interaction between two charged dielectric spheres in contact.* Physical Review E, 2000. **62**(2): p. 2891-2897.
27. Matsuyama, T., H. Yamamoto, and M. Washizu, *Potential distribution around a partially charged dielectric particle located near a conducting plane.* Journal of Electrostatics, 1995. **36**(2): p. 195-204.
28. Jackson, J.D., *Classical Electrodynamics (Third Edition).* 1999: John Wiley & Sons, INC., p.57-61, p.154-159.
29. B.I.Bleaney, B.B., *Electricity and Magnetism (Second Edition).* 1968: Oxford University Press, p.48-57.

30. Zhou, H.B., M. Gotzinger, and W. Peukert, *The influence of particle charge and roughness on particle-substrate adhesion.* Powder Technology, 2003. **135**: p. 82-91.
31. Burnham, N.A., R.J. Colton, and H.M. Pollock, *Work-Function Anisotropies as an Origin of Long-Range Surface Forces.* Physical Review Letters, 1992. **69**(1): p. 144-147.
32. Guerret-Piecourt, C., et al., *Adhesion forces due to nano-triboelectrification between similar materials.* European Physical Journal-Applied Physics, 2004. **28**(1): p. 65-72.
33. Lindell, I.V., *Electrostatic Image Theory for the Dielectric Sphere.* Radio Science, 1992. **27**(1): p. 1-8.
34. Lindell, I.V., J.C.E. Sten, and K.I. Nikoskinen, *Electrostatic Image Method for the Interaction of 2 Dielectric Spheres.* Radio Science, 1993. **28**(3): p. 319-329.
35. Matsuyama, T. and H. Yamamoto, *Charge relaxation process dominates contact charging of a particle in atmospheric conditions.* Journal of Physics D-Applied Physics, 1995. **28**(12): p. 2418-2423.
36. Masaaki Otsuka, T.M., and Hideo Yamamoto. *Measurement of Force Curve Due to Electrostatic Charge on a Particle with Atomic Force Microscope.* in *The Fitth World Congress on Particle Technology*. 2006. Orlando, FL.
37. Domike, R., *Pharmaceutical Powders in Experiment and Simulation*, in *Department of Chemical Engineering*. 2003, Massachusetts Institute of Technology.
38. Hinds, William C., *Aerosol Technology : Properties, Behavior, and Measurement of Airborne Particles*, New York: Willey, 1999

4 Capillary Force

4.1 Introduction

The primary adhesion forces for a dry particle on a dry substrate consist of van der Waals and electrostatic forces. In a humid environment, an additional force plays an important role in particle adhesions. Because of condensation of water vapor, a liquid bridge forms between contact interfaces. The forces that arise due to the liquid bridge may be both capillary and viscous in nature, i.e. static and dynamic, respectively[1]. The viscous force can be significant when liquid viscosity is high or particles are approaching each other at high relative velocities[2]. In our study only the static capillary force is investigated.

Capillary force, also known as meniscus force, has been studied extensively for decades. In terms of single particle behavior with moisture present, atomic force microscopy has been used to investigate the effect of relative humidity (RH) on the adhesion properties of metal, silica and pharmaceutical powder surfaces[3-7]. For bulk powders, the degree of adhesion as a function of relative humidity was evaluated by the centrifuge detachment technique[8-10]. Observations generally indicated an increase in the adhesion with increased relative humidity. However, there are conflicting reports in the literature suggesting that adhesion, which was interactive system-dependent, can increase, decrease or pass through a maximum as the relative humidity increases[11, 12].

The magnitude of capillary force can be changed by altering the amount of water present, the surface chemistry, or the surface roughness. It was shown that elevated relative humidity can progressively modified surface topology[13] and cause an increase in the number of contacting points[14], thus leading to a higher adhesion force. In terms of surface chemistry, the adhesion force was observed to increase uniformly with relative humidity for hydrophilic surfaces while exhibited no significant RH dependence for the hydrophobic surfaces[15]. The effect of surface roughness on capillary force was much more complicated. It was stated in Chapter 2 that there is a significant decrease in van der Waals force for surfaces with increased surface roughness. Likewise, capillary adhesion was substantially lower in the presence of nanoscale

roughness[15]. In addition, the water meniscus geometry was strongly affected by local surface curvature[16] and capillary bonding can increase or decrease with roughness at specific conditions[17].

The formation and stabilization of the liquid bridge between two surfaces only occurs when the relative humidity is above a critical value. If the humidity is below the critical value, the moisture will be present in the form of adsorbed water vapor layer on the surface. The value of the critical relative humidity is dependent on the capability of physical adsorption of gas molecules on the surface as well as the surface roughness. A particle with higher BET constant and/or rougher surfaces tended to have higher critical relative humidity[18]. The critical relative humidity was reported to vary from 50% to 80% for varied particulate systems[19].

In our work, in order to better understand the contribution of the capillary force to the total particle cohesion, the hygroscopicity of powder particles were analyzed, the cohesion force as a function of the relative humidity was measured for individual pharmaceutical particles, and a mathematical model was developed to predict the magnitude of the capillary force. The details are described in Section 4.2-4.4, respectively.

4.2 Hygroscopicity characterization of excipient powders

Hygroscopicity is the capacity of a substance to attract water molecules from the surrounding environment through either absorption or adsorption. It is an important powder property influencing particle cohesion interactions with moisture present. In our experiments the hygroscopic properties of both lactose and microcrystalline cellulose (MCC) powders were analyzed by the Dynamic vapor sorption instrument (Surface Measurement Systems, UK). The sample powders were suspended from an ultra-microbalance inside a chamber. The mixed saturated and dry carrier nitrogen gas flows over the sample with precise mass flow control and real time monitoring of water vapor concentration. Once the sorption/desorption of water vapor molecules gets to equilibrium, the weight change of the powders with respect to the relative humidity variation inside the chamber was recorded automatically. Figure 4-1 shows the dynamic vapor sorption profile of both lactose and MCC powders.

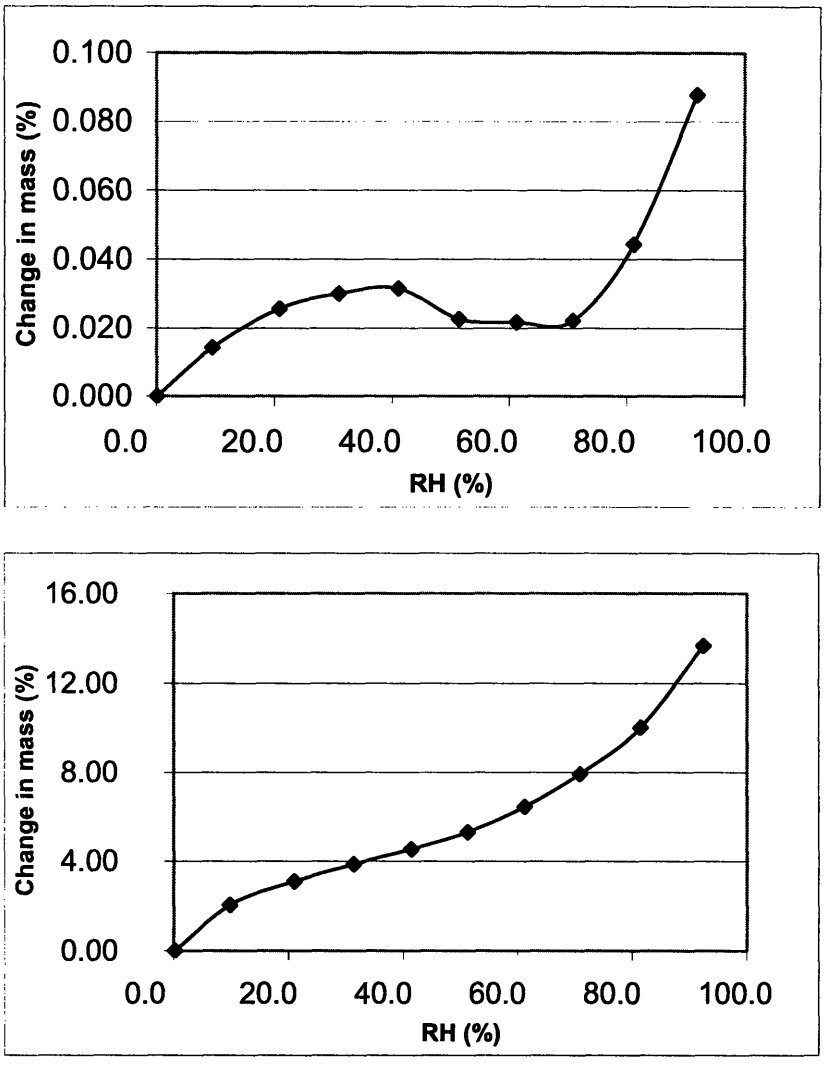

Figure 4-1 Dynamic vapor sorption curve: (a) lactose DCL11; (b) MCC particles

By comparing the dynamic vapor sorption profile of lactose particles and MCC particles, it was found that, in the same RH range, the change in the MCC sample weight is as high as 14% while the weight of lactose samples changed only up to 0.08%, suggesting that MCC is much more hygroscopic than lactose. Therefore, MCC particles are capable of absorbing more water molecules on the surface than lactose at the same RH conditions.

4.3 Measurement of inter-particle capillary force

4.3.1 Experimental

The cohesion forces between individual particles at varied relative humidity were measured by AFM. The procedures for the tip and sample preparation were the same as described in Section 2.2. Both the tips and the sample particles were stored in a desiccator where the RH was kept at 5% with P_2O_5 as desiccant before the AFM experiments. During the measurements the AFM was placed in an environmental hood. The hood was connected with two streams of nitrogen gas, one of which is dry nitrogen and the other going through a water tank and thus carrying a certain amount of water vapor. The RH inside the hood can be varied from 0% to 75% by adjusting the ratios of dry and wet N_2 flowing into the hood. Every time the relative humidity was adjusted to a new value, the tip and the sample particle were held without touching each other inside the hood for two hours to attain the water vapor adsorption equilibrium as much as possible. Then the cohesion force between the two particles was measured by the AFM force volume mode. The temperature and the relative humidity inside the hood were recorded in real time from a digital hygrometer (Traceable®, model 35519-041, Control Company, USA) inserted into the hood.

4.3.2 Results

The cohesion force variation with relative humidity for different lactose particles were plotted in Figure 4-2. Interestingly, in spite of being the same material, the variation of the cohesion force with the increase of the RH showed different trends for different pairs of particles. The majority of the measured particles appeared to have a slow increase in their cohesion forces in the low to medium relative humidity range and attain the maximum cohesion forces at the relative humidity higher than 45%, as seen in Figure 4-2(a). It implied that the critical relative humidity for lactose powders is in the range of 45-60%, where the complete liquid bridge was formed between particle surfaces and the capillary force became dominant over the van der Waals force. Compared to the cohesion force at the lowest RH, which was expected to be van der Waals force predominantly, the increase in the cohesion force due to the presence of capillary force was 17~60 nN, accounting for 20~50% of the total cohesion force. In contrast, a few particles had no obvious change in the cohesion force till the relative humidity was

higher than 60%, when the cohesion force showed a steep increase, shown in Figure 4-2(b). For a few other particles, the peak cohesion forces were unusually observed at the relative humidity lower than 40% (see Figure 4-2(c)), plausibly due to the surface contamination or unsuccessful moisture elimination before the measurement.

(a)

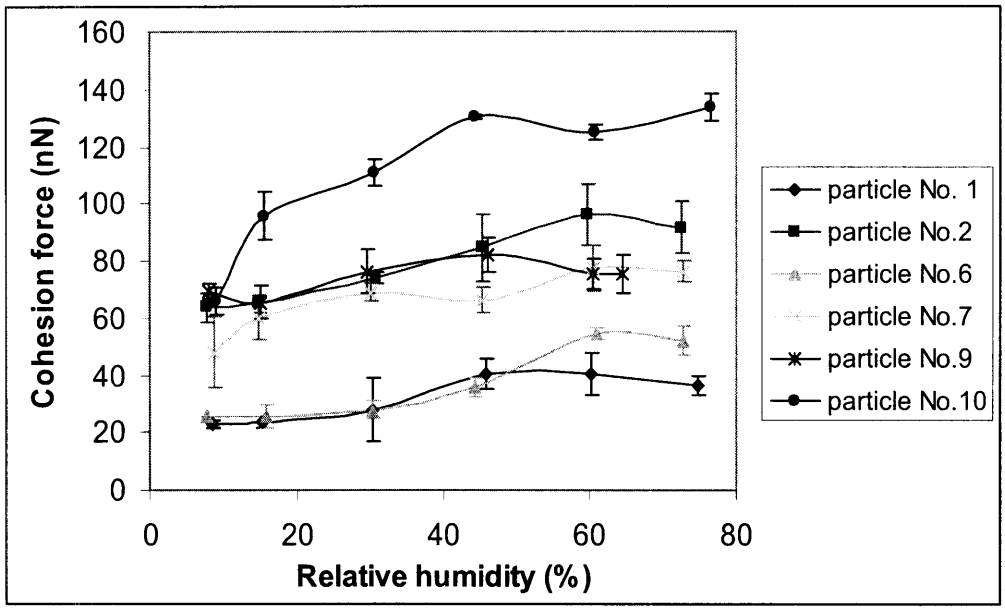

(b)

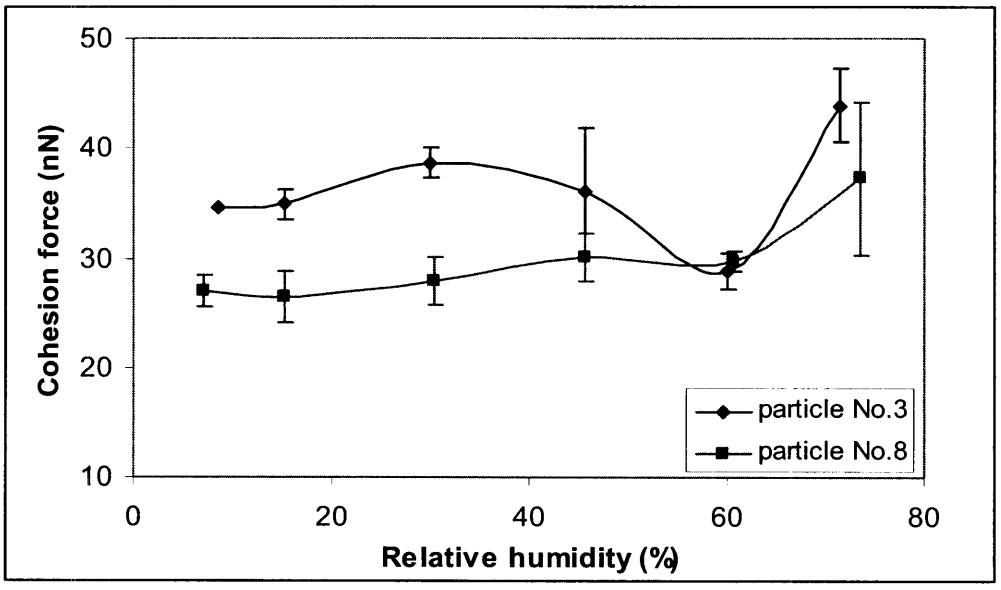

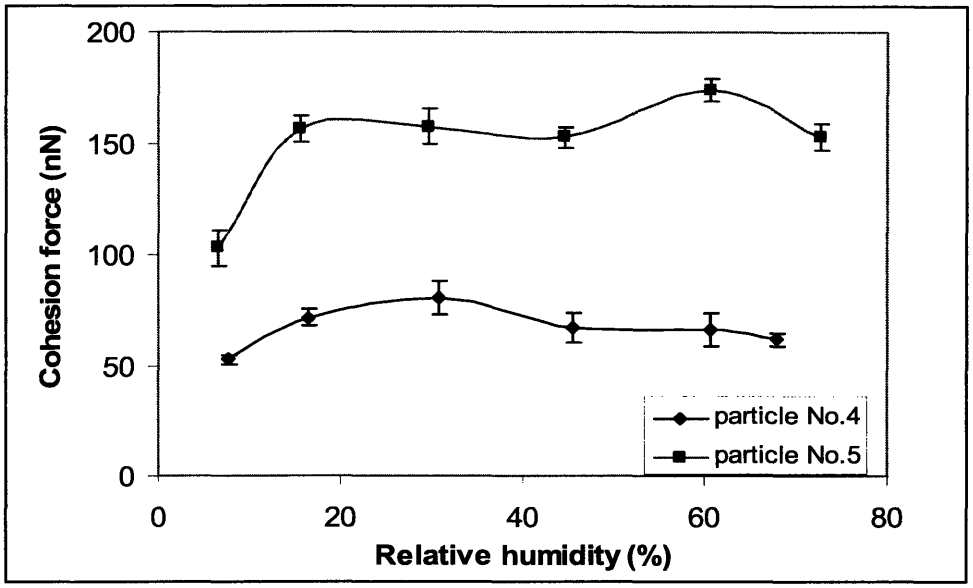

(c)

Figure 4-2 Cohesion force variation with the relative humidity for different lactose particles

The same experiments were conducted for microcrystalline cellulose (MCC) particles. The results are shown in Figure 4-3. Because of the high hygroscopicity of MCC, the cohesion force can increase significantly up to 50-100 nN at a low to medium relative humidity range, i.e., the critical RH value of MCC particles is lower than for lactose particles . Similarly as lactose curves, the trends of the cohesion force variation with relative humidity were not consistent for different MCC particles.

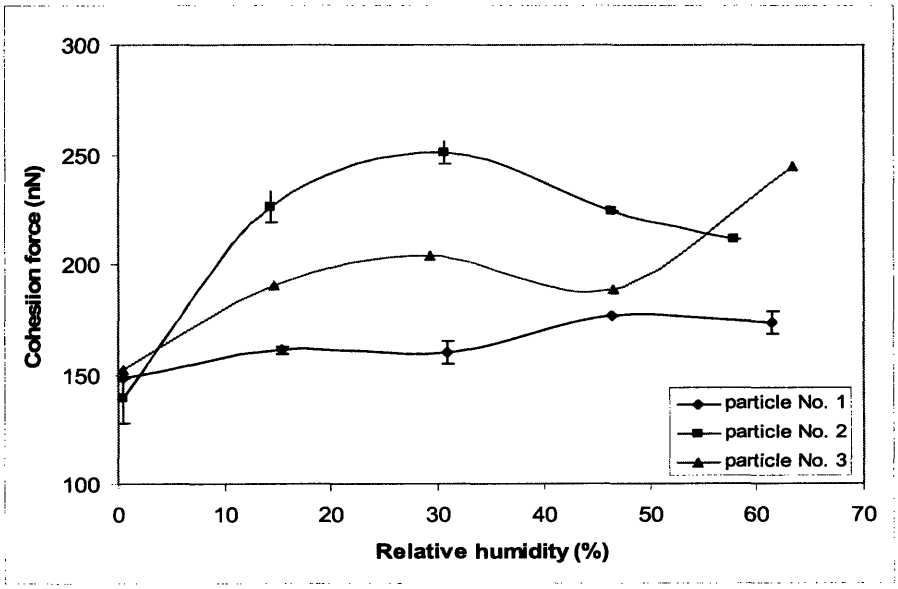

Figure 4-3 Cohesion force variation with the relative humidity for different MCC particles

4.3.3 Discussions

In general, it is shown from our experimental results that both lactose and MCC had an increase in particle cohesion force with the elevation of relative humidity and attained the maximum cohesion force at a critical relative humidity level. However, the rate of force increase and the critical RH value were different among individual particles even for the same material. Excluding the effect of surface chemistry, the observed inconsistency is most likely attributed to the nanoscale heterogeneity of surface contact geometry. Due to the existence of surface asperities, the surface curvature and the shape of the liquid meniscus at the contact region may vary significantly from one particle to another. As proposed by Hooton and his coworkers[20], there are three scenarios of surface contact geometry, as shown in Figure 4-4. For a single asperity contact, there is a clearly defined peak in the humidity profile, whereas for multiple asperities contact, the peak could be less sharp if the gaps between the asperities are not filled with moisture. If the asperities have smaller dimensions relative to the surface, the meniscus is filled within the contact region and the cohesion force increases monotonically without peak effect. Based on this argument, the humidity profiles for the majority of particles in our experiments were most likely captured at multiple asperities contact geometry as described in the second scenario.

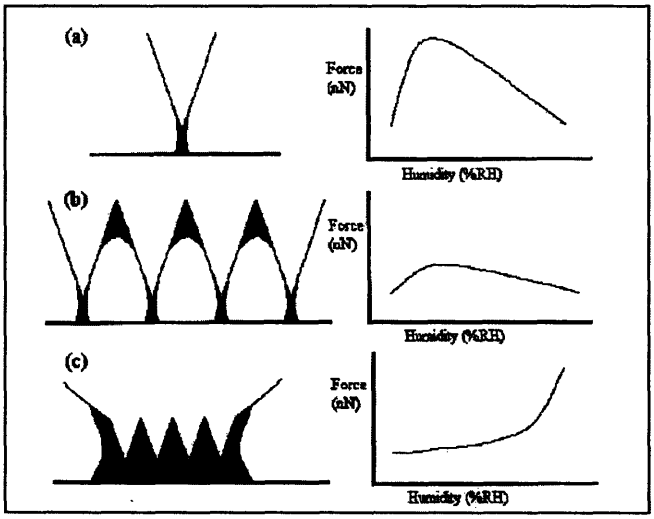

Figure 4-4 The cohesion behaviors corresponding to three scenarios of surface contact geometry[20]

Things may get even more complicated when the dynamics of liquid meniscus formation is taken account of in interpreting the diversity of the humidity profiles. With the increase of the

RH, the volume of the liquid bridge will increase accordingly. For smooth particles the shape of the liquid bridge can be well defined at different stages of the growth, as observed in previous work[21]. However, for particles with rough surfaces, the contact geometry may vary associated with the liquid bridge formation. As shown in Figure 4-5, when the liquid bridge first appears at the low RH, the two particles with rough surfaces contact with each other in single asperities. Then multiple asperities may be involved into the contact region, and finally the nano-scale contact is replaced by the macro-scale contact in a larger area between two particles when the RH is sufficiently high. This transition has been discussed in Halsey's work[22].

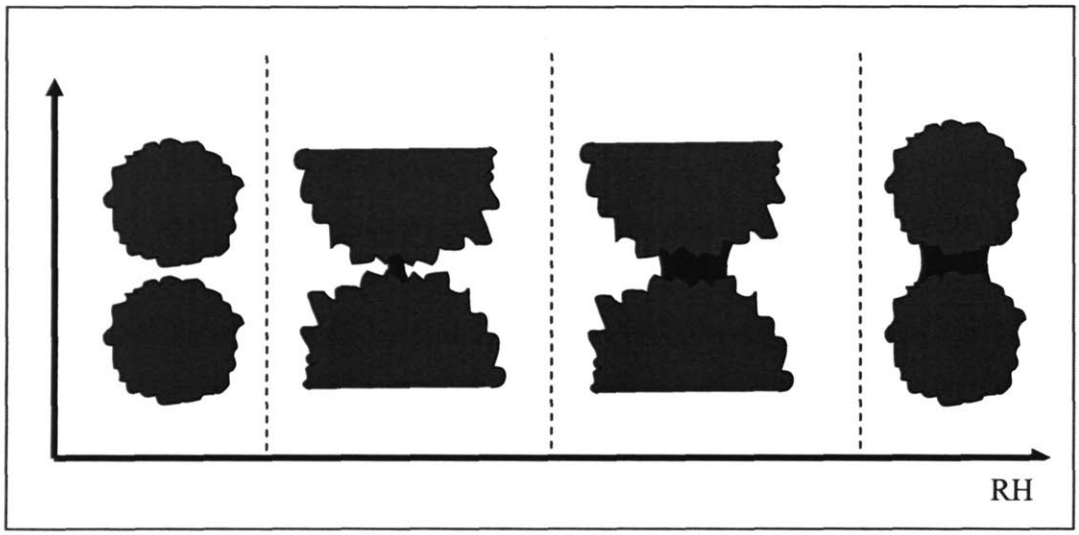

Figure 4-5 Illustration of liquid bridge growth with the elevated relative humidity

In addition to the experiments, modeling work has been implemented to quantitatively elucidate the dependence of capillary force on particle characteristics and environmental variables. The details are described in the next section.

4.4 Modeling of inter-particle capillary force

4.4.1 Theory of capillary force

The theory of capillary force has been well established. Generally the liquid meniscus between the surfaces is assumed to be thermodynamically stable with a well-defined curvature, as shown in the schematic of sphere-substrate contact in Figure 4-6.

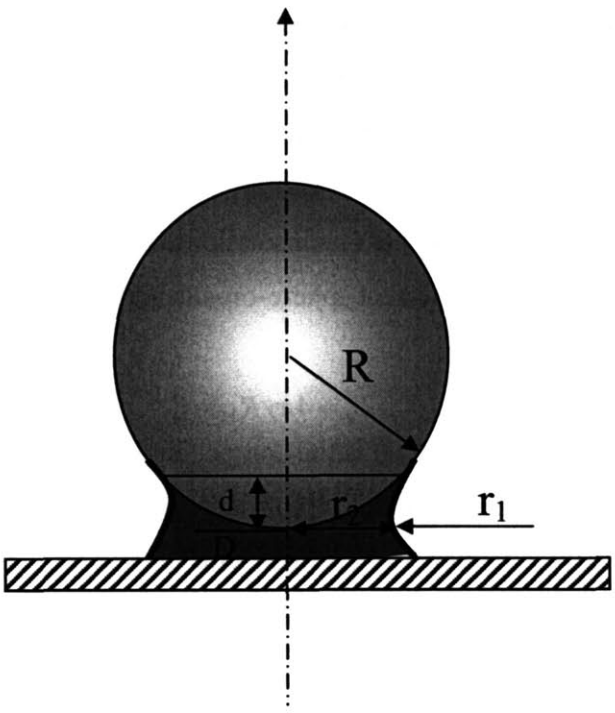

Figure 4-6 Schematic of sphere-substrate contact with liquid meniscus present

The capillary force, also known as meniscus force, has two principal components. The first force component arises from the Laplace pressure across the meniscus, expressed as:

$$F_P = \Delta P \cdot \pi r_2^2 \tag{4.4-1}$$

where r_2 is the radius of the liquid neck, ΔP is the pressure difference across the air-liquid interface and calculated as:

$$\Delta P = \gamma\left(\frac{1}{r_1} - \frac{1}{r_2}\right) \tag{4.4-2}$$

where γ is the surface tension of liquid, r_1 is the radius of curvature of the liquid surface. In liquid bridges this pressure is constant if the effect of gravity is negligible. If the pressure within the liquid bridge is less than the external pressure, the Laplace pressure is defined as positive. The capillary pressure adds to the adhesion. Otherwise the resultant effect is repulsive.

The second component arises from the vertical component of the surface tension acting along the meniscus, expressed as:

$$F_S = 2\pi r_2 \gamma \tag{4.4-3}$$

If liquid is present between the surfaces of two solid bodies, the forces arisen from the surface tension of the liquid always has an attractive effect on the surfaces of the bodies, and it is always small compared to the Laplace pressure contribution.

If assuming that the meniscus radius r_1 is much smaller than the contact radius of the meniscus r_2, the capillary force for perfect sphere-on-substrate geometry can be derived based on the Laplace-Kelvin theory as[15]:

$$F_c = 4\pi\gamma R\cos\theta \tag{4.4-4}$$

where R is the radius of the sphere, and θ is the contact angle of liquid on the surface. The RH dependence vanishes in the equation in this simplified case. A more accurate expression is derived from the total surface free energy changes with separation. The attractive force between the sphere and the surface with a separation distance D due to the presence of a liquid bridge is[23]:

$$F_c = \frac{4\pi\gamma R\cos\theta}{(1+\frac{D}{d})} \tag{4.4-5}$$

where D is the distance between the two surfaces and d the length of the meniscus immersed into the surface, as illustrated in Figure 4-6. For two spheres in contact, R is replaced by the reduced radius $\left(\frac{1}{R_1}+\frac{1}{R_2}\right)^{-1}$.

The thickness of condensed water vapor film is strongly related to the relative humidity. The equilibrium radius of the liquid meniscus, r_k, can be described by the Kelvin equation:

$$r_k = \frac{-V_M\gamma}{RT\ln(\psi)} \tag{4.4-6}$$

where V_M is the molar volume of the liquid, γ is the surface tension of the liquid, ψ is the relative humidity, R is the gas constant, T is the absolute temperature. The dependence of r_k on the relative humidity was illustrated in Figure 4-7.

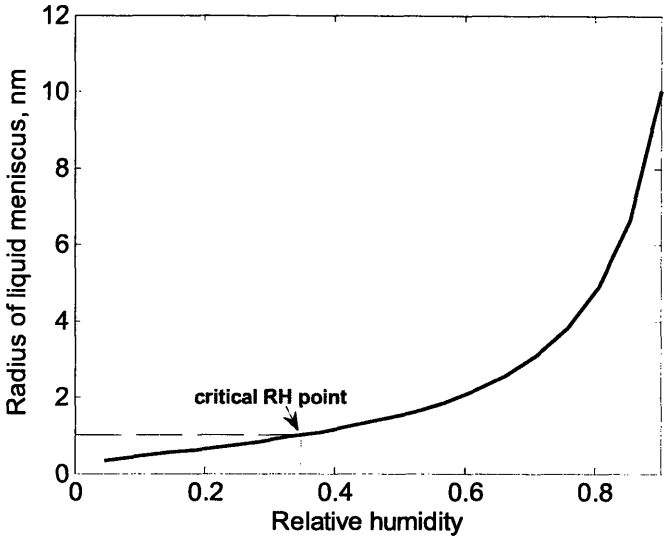

Figure 4-7 Radius of liquid meniscus as a function of relative humidity

It was proposed by Robinovich and his coworkers[24] that there is certain annulus volume or dimension, below which, the adsorbed molecules cannot be considered a macroscopic phase and consequently, no surface tension or capillary force would exist at a humidity less than a critical value. For ideally smooth solids, the critical radius of the meniscus is approximately 1 nm, and the corresponding RH derived from the Kelvin equation is about 35%. Obviously this value is lower than the critical RH value of 45-60% observed from our experiments, where the shape of the liquid meniscus may be altered due to the presence of surface asperities of rough particles.

4.4.2 Capillary force model for two interacting spheres with surface roughness

Based on the capillary theory, several models have been developed to describe the capillary force in situations such as the force between two wetted spheres[25] and the force between a dry sphere and a wet flat substrate[26]. However, the surface contact geometry of particles becomes complicated when the nano-scale surface roughness is taken account in the model. As discussed in a recent paper by Farshchi-Tabrizi et al[27], the variation in the asperity height and shape may change the meniscus force vs. humidity curve dramatically.

To describe the dependence of the capillary force on surface roughness, a model was suggested by Rabinovich et al[24, 28] for contact between an ideally smooth sphere and a substrate with nanoscale roughness. Based on Rabivinoch's model, we developed a modified model for the capillary force between two rough particles. To simplify the problem, only single asperity contact was considered in the model, and the asperity shape was assumed to be hemispherical. Figure 4-8 illustrates the contact between two hemispherical asperities with liquid meniscus present.

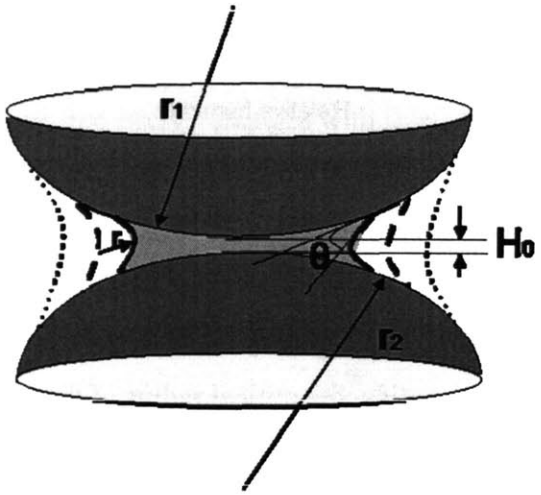

Figure 4-8 Schematic illustration of the model for capillary force between two asperities

Assuming that the volume of the liquid annulus is small relative to the particle size and the contact angle is small(<<1 rad), the expression of the capillary force is derived as:

$$F_c = 4\pi\gamma R_{eff}\cos\theta[1-\frac{H_0}{2r\cos\theta}] \tag{4.4-7}$$

where H_0 is the separation distance between the two hemispheres, when the two surfaces are in contact, the value of H_0 is usually taken as 0.4 nm; r is the radius of the meniscus that can be calculated by the Kelvin's equation; θ is the contact angle of the liquid to the surface, for two particles of different materials, $\cos\theta = \frac{\cos\theta_1 + \cos\theta_2}{2}$; R_{eff} is the reduced radius of the two asperities. Referring to Rabinovich's derivation[29], it can be correlated to the root-mean-square (rms) values measured from AFM:

$$R_{eff} = \frac{r_1 r_2}{r_1 + r_2} = \frac{1.485 rms_1 \cdot rms_2}{rms_1 + rms_2} \tag{4.4-8}$$

The capillary force is expressed as a function of surface tension, contact angle, surface roughness and relative humidity in our model.

Assuming that the cohesion force measured by the AFM at the RH close to 0% is totally due to contribution from the van der Waals force, and the increased cohesion force measured at the higher RH levels arises from the net capillary force, the capillary force data in the RH range of 0-80% for 10 individual lactose particles were measured and compared with the theoretical values calculated from the equation 1.4-7. In the calculation, the rms value of the particle was obtained from the AFM measurements; the contact angle of water on the lactose surface was cited[30] as 30° and the surface tension of water is known to be 0.0728 N/m (at 20°C). The comparison results were shown in Figure 4-9.

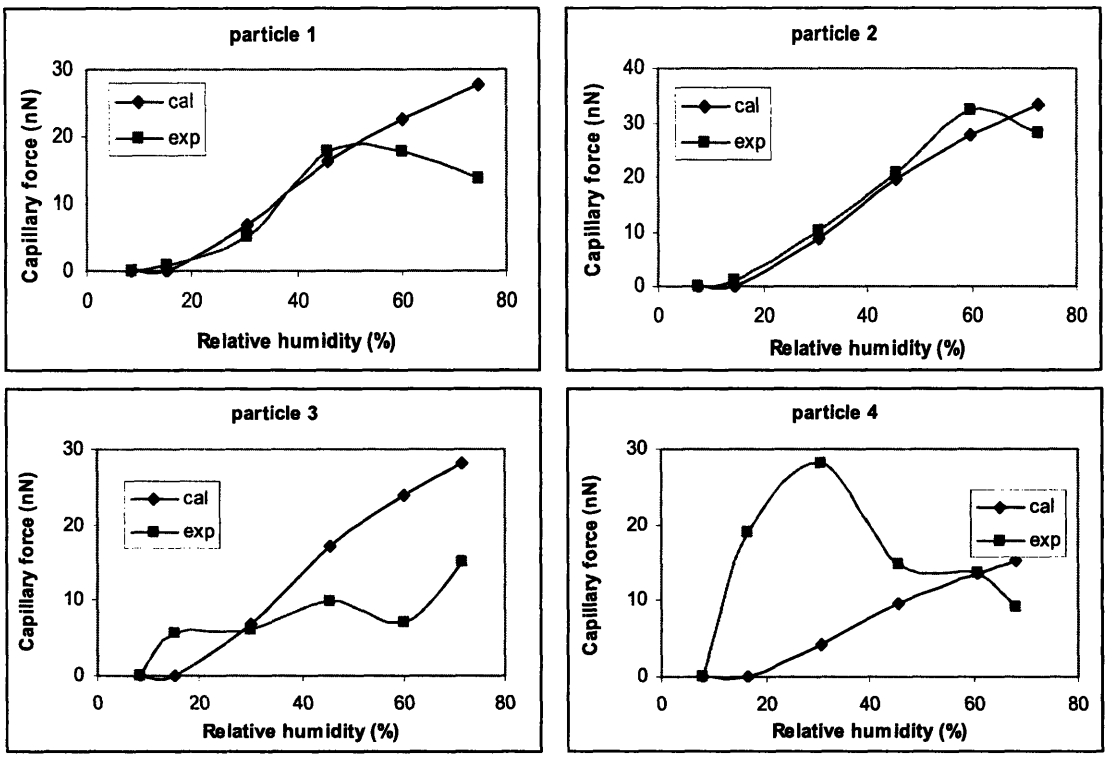

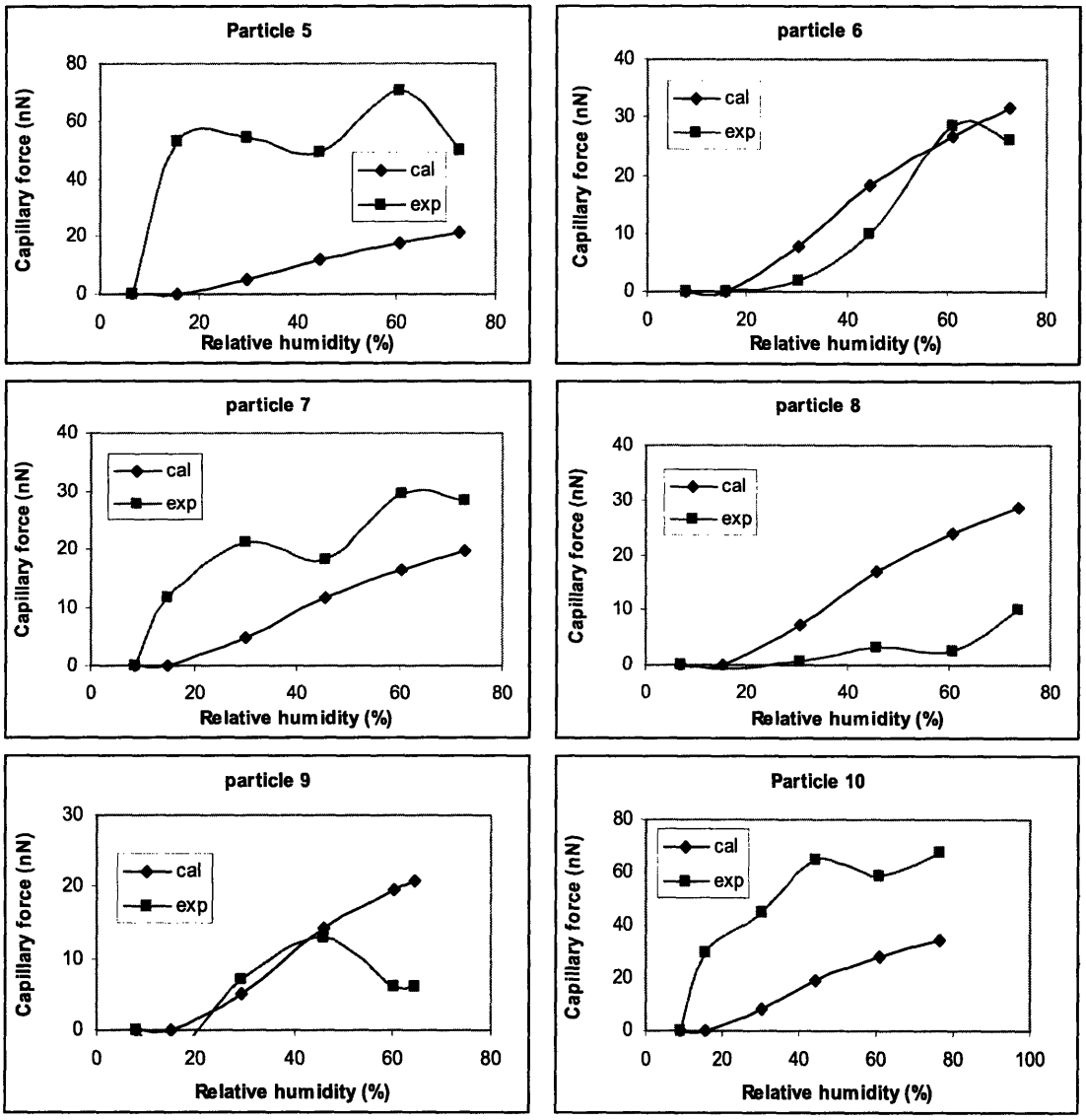

Figure 4-9 Comparison between the experimental and theoretical capillary forces of lactose particles

It is not surprising to see large discrepancies between the experimental and the calculated values. Because the surface contact geometry is oversimplified and the transition from the water vapor film to the liquid condensation is not considered in the model, the model failed to depict accurately the capillary force variation at a wide RH range. Nevertheless, the calculated capillary force has the same order of magnitude as the experimental value and tends to have a better fit at low to medium RH range. This model can be utilized to provide a rough estimation of the capillary force between two single particles with rough surfaces.

4.4.3 Sensitivity of capillary force to the surface contact geometry

As mentioned earlier, the capillary force is closely related to the surface contact geometry, which also affects the local curvature of the liquid bridge. In this section, the sensitivity of capillary force to the surface contact geometry was investigated theoretically based on different contact geometry models.

In the first scenario the hemispherical asperity shape at the point of contact was considered, as shown in Figure 4-10.

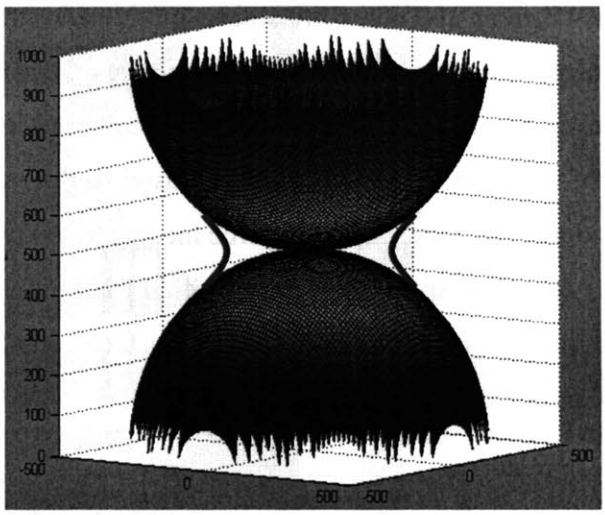

Figure 4-10 Surface contact geometry of hemispherical asperites

According to the equation (1.4-1)-(1.4-3), the capillary force at the liquid neck is given by:

$$F_c = 2\pi\gamma r_2 + \pi\gamma r_2^2\left(\frac{1}{r_1} - \frac{1}{r_2}\right) \tag{4.4-9}$$

Where γ is the surface tension of water; r_1 is the radius of curvature of the liquid surface; r_2 is the radius of the liquid neck.

Assuming that the liquid-vapor interface is circular and the effect of gravity on the liquid surface is negligible, the radii of the liquid surface curvature and the liquid neck between two identical solid spheres has been derived in Coughlin's work[31] based on strict geometrical relationship. The expressions of r_1 and r_2 are given by:

$$r_1 = \frac{3 + 4kr\cos\theta - \sqrt{9 + 8kr\cos\theta}}{4k(1 + kr\cos\theta)} \tag{4.4-10}$$

$$r_2 = \frac{r_1}{1 - kr_1} \tag{4.4-11}$$

where r is the radius of the hemispherical asperity, θ is the contact angle of water on the asperity surface, k equals to $2/r_k$, r_k is the liquid surface radius calculated by the Kelvin's equation.

Introducing the equations (4.4-9) and (4.4-10) into the equation (4.4-8), the formula for the capillary force between two spheres was expressed explicitly as a function of contact angle, surface tension, asperity radius and relative humidity. Based on the AFM image observation, the asperity radius r was taken as 100 nm, comparable to the surface roughness of lactose particles. With known contact angle and surface tension values, the dependence of the capillary force on the relative humidity is exhibited numerically in Figure 4-11. The calculated capillary force value was 30-40 nN and decreased slightly with the relative humidity. This coincided well with the capillary force measured at high RH in our experiments (See Figure 4-9). It is speculated that at a high RH level, the asperities are likely to be immersed into the liquid volume and therefore the surface contact geometry is close to the macro-scale sphere contact as demonstrated in Figure 4-5.

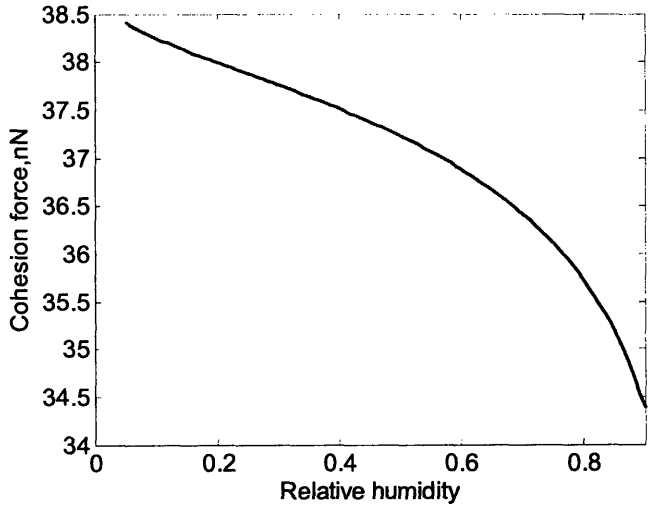

Figure 4-11 Capillary force vs. Relative humidity for spherical asperity contact

In the second case, inspired by Coughlin's model[31], the asperities were considered as solids with boundary function $y=px^m$. With different p and m value, the asperity shape varied, so did the corresponding capillary force profile. In the modeling the specific p and m value was

given to assure that the simulated asperity has a radius of 1 μm and a height of 200 nm, comparable to the actual asperity size observed in the AFM experiments. The mathematical derivation of the analytical expression of the capillary force at this specific contact geometry was referred to in Coughlin's work[31] and was incorporated in the MATLAB code developed in our lab. Four different asperity geometries were generated and the capillary force values calculated. The results are shown in Figure 4-12.

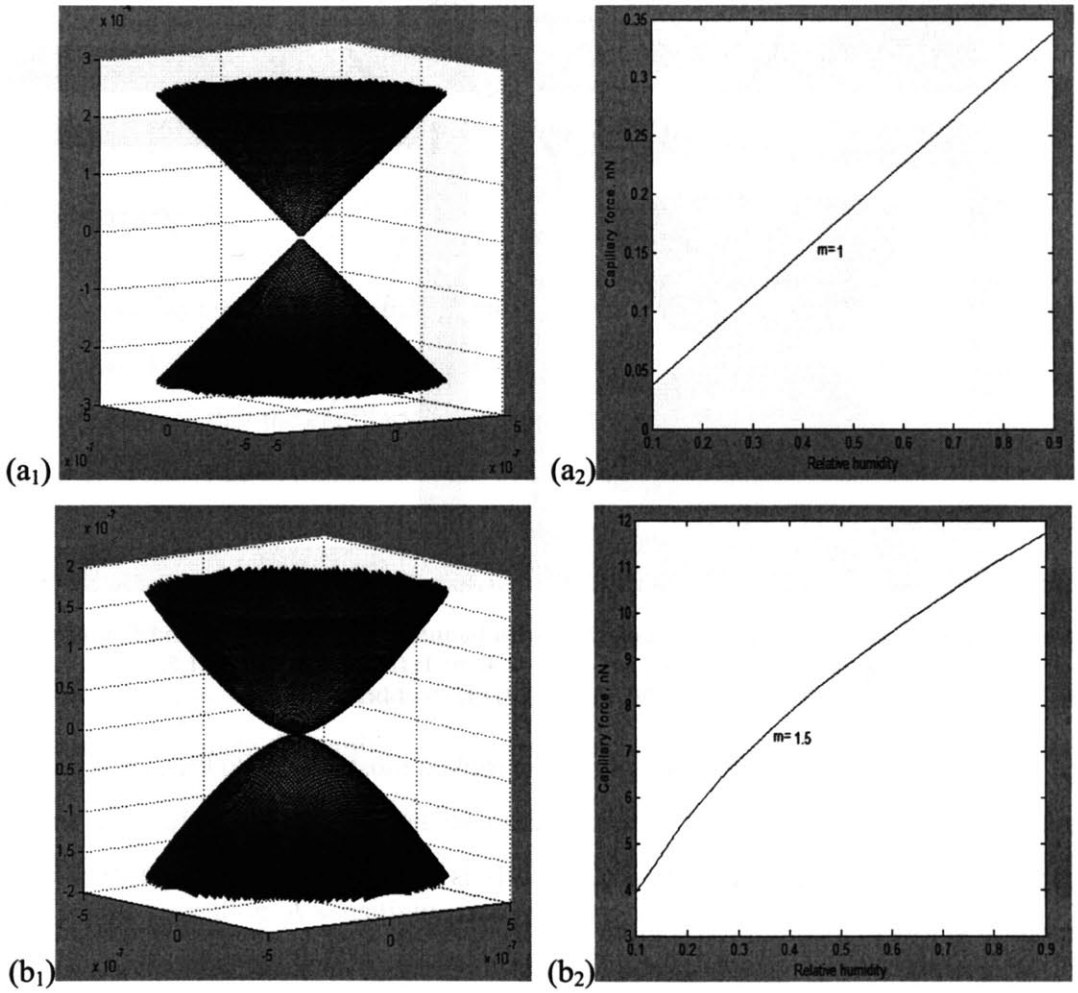

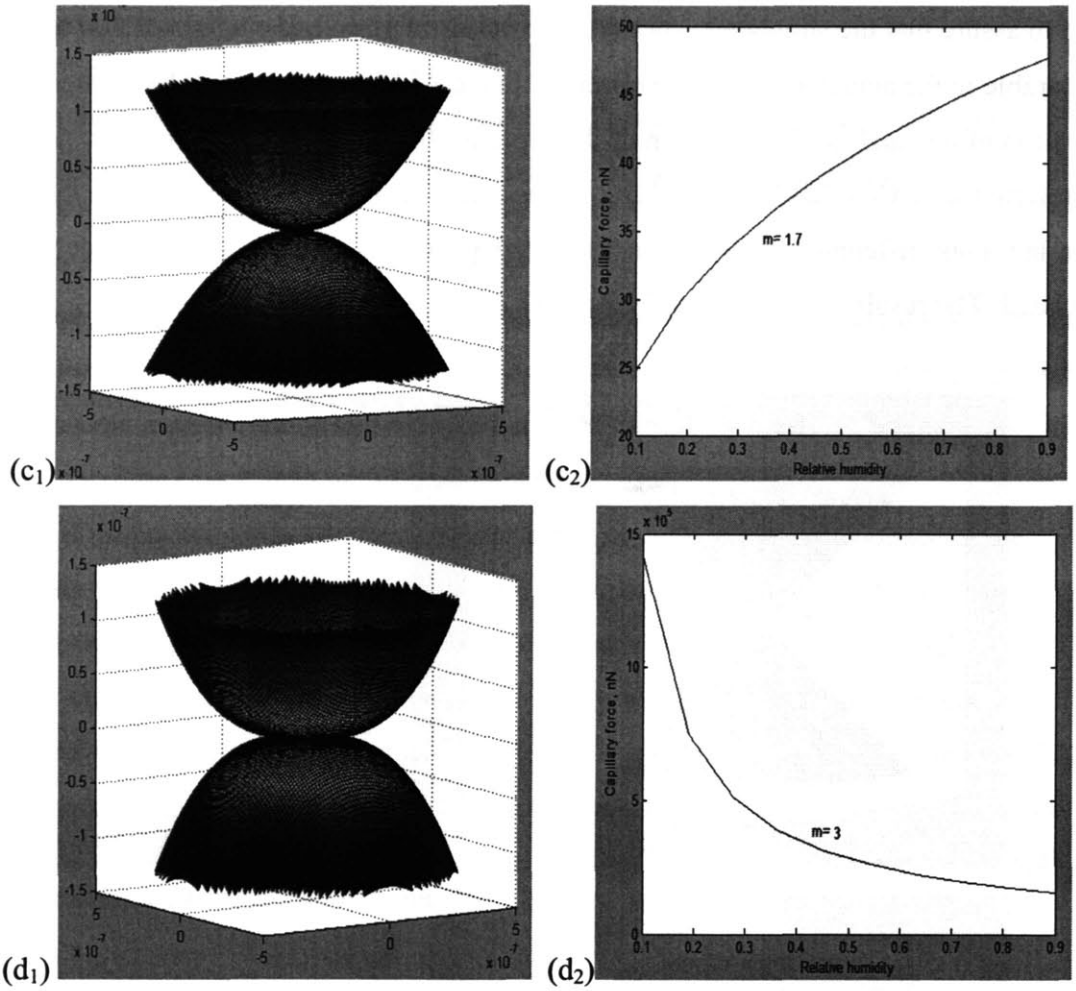

Figure 4-12 Surface contact geometry of asperities with boundary function $y=px^m$ and the corresponding capillary force profile: (a1-a2) p=0.4, m=1; (b1-b2) p=500, m=1.5; (c1-c2) p=8000, m=1.7; (d1-d2) p=14×10^{11}, m=3

When m value was 1.5 or 1.7, the asperity shape looked most similar to the actual case and the magnitude of the resulted cohesion force was close to the experimental value. The trend that the capillary force increases with relative humidity is consistent with the experimental observation at low to medium RH region.

When m value was changed to 3, the magnitude of r_1, i.e., the radius of curvature of the liquid surface, was reduced several order of magnitude due to the surface curvature change of the new asperity geometry. As seen in the equation (4.4-9), with the decrease of r_1, the value of F_c will be increased dramatically. Meanwhile, the decrease of r_1 makes the value of the second item in the equation substantially higher than the first one. In other words, the

contribution from the Laplace pressure difference to the capillary force is dominant over that from the surface tension. Since the pressure difference is reduced at higher RH levels, the magnitude of F_c is decreased with the elevation of RH, showing an opposite trend as opposed to the first three cases.

With the modification of the asperity curvature, both the magnitude and the trend of the capillary force changed dramatically. Combined with the result obtained in the first case, it indicated that the capillary force is very sensitive to the surface contact geometry when the particle surface roughness is taken into account.

4.5 Summary

Capillary force plays an important role in particle cohesion interactions with moisture present. It is a function of the contact angle, surface roughness and the relative humidity. The experiments showed that the capillary force for both lactose and MCC particles increases with the elevation of the relative humidity at the low to medium RH range and then decreases when the RH is higher than the critical point. The critical RH value is dependent on the hygrosopic properties of the material. MCC is more hygroscopic than lactose, thus it has a lower critical RH value than lactose. It also is found that different particles of the same material have distinct capillary force profiles. A single hemispherical asperity contact model was proposed to simulate the capillary force between two rough particles. The discrepancy between the calculated capillary force and the experimental data was attributed to the oversimplification of the surface contact geometry and inadequate knowledge of the dynamics of liquid bridge formation. A sensitivity analysis on several different asperity contact geometries showed that the heterogeneity of surface asperities has a great effect on the capillary force. Although the model fails to predict precisely the capillary force variation over the full RH range, it allowed a rough estimation of the magnitude of capillary force between rough particles. In order to improve the predictability of the model, a better way of surface contact geometry characterization and a thorough understanding of the uncertainties in the transition from the adsorbed water film to the liquid bridge formation is necessary in the further investigation.

4.6 References

1. B.H.Xu, A.B.Y., S.J.Chew and P.Zulli. *A study of the effect of liquid-induced forces on gas-solid flow by a combined continuum and discrete model.* in *Second Internatioal Conference on CFD in the Minerals and Process Industries*. 1999. CSIRO, Melbourn, Australia.
2. Adams, M.J.a.P., V., *The cohesive forces between particles with interstitial liquid.* Inst. Chem. Eng. Symp., 1985. **91**: p. 147-160.
3. Jones, R., et al., *Inter-particle forces in cohesive powders studied by AFM: effects of relative humidity, particle size and wall adhesion.* Powder Technology, 2003. **132**(2-3): p. 196-210.
4. Fuji, M., et al., *Effect of wettability on adhesion force between silica particles evaluated by atomic force microscopy measurement as a function of relative humidity.* Langmuir, 1999. **15**(13): p. 4584-4589.
5. Price, R., et al., *The influence of relative humidity on particulate interactions in carrier-based dry powder inhaler formulations.* International Journal of Pharmaceutics, 2002. **246**(1-2): p. 47-59.
6. Young, P.M., et al., *The influence of relative humidity on the cohesion properties of micronized drugs used in inhalation therapy.* Journal of Pharmaceutical Sciences, 2004. **93**(3): p. 753-761.
7. Young, P.M., et al., *Investigation into the effect of humidity on drug-drug interactions using the atomic force microscope.* Journal of Pharmaceutical Sciences, 2003. **92**(4): p. 815-822.
8. Podczeck, F., J.M. Newton, and M.B. James, *The influence of constant and changing relative humidity of the air on the autoadhesion force between pharmaceutical powder particles.* International Journal of Pharmaceutics, 1996. **145**(1-2): p. 221-229.
9. Podczeck, F., J.M. Newton, and M.B. James, *Variations in the adhesion force between a drug and carrier particles as a result of changes in the relative humidity of the air.* International Journal of Pharmaceutics, 1997. **149**(2): p. 151-160.
10. Podczeck, F., J.M. Newton, and M.B. James, *Influence of relative humidity of storage air on the adhesion and autoadhesion of micronized particles to particulate and compacted powder surfaces.* Journal of Colloid and Interface Science, 1997. **187**(2): p. 484-491.
11. Kulvanich, P. and P.J. Stewart, *Influence of Relative-Humidity on the Adhesive Properties of a Model Interactive System.* Journal of Pharmacy and Pharmacology, 1988. **40**(7): p. 453-458.
12. J.A.S.Cleaver and J.W.G.Tyrrell, *The influence of relative humidity on particle adhesion - a review of previous work and the anomalous behaviour of soda-lime glass.* KONA, 2004. **22**: p. 9-22.
13. Berard, V., et al., *Dry powder inhaler: influence of humidity on topology and adhesion studied by AFM.* International Journal of Pharmaceutics, 2002. **232**(1-2): p. 213-224.
14. Ando, Y., *The effect of relative humidity on friction and pull-off forces measured on submicron-size asperity arrays.* Wear, 2000. **238**(1): p. 12-19.

15. Jones, R., et al., *Adhesion forces between glass and silicon surfaces in air studied by AFM: Effects of relative humidity, particle size, roughness, and surface treatment.* Langmuir, 2002. **18**(21): p. 8045-8055.
16. Sirghi, L., et al., *Effect of sample topography on adhesive force in atomic force spectroscopy measurements in air.* Langmuir, 2000. **16**(20): p. 7796-7800.
17. Colbeck, S.C., *Capillary bonding of wet surfaces - The effects of contact angle and surface roughness.* Journal of Adhesion Science and Technology, 1997. **11**(3): p. 359-371.
18. Harnby, N., A.E. Hawkins, and I. Opalinski, *Measurement of the adhesional force between individual particles with moisture present.2. A novel measurement technique.* Chemical Engineering Research & Design, 1996. **74**(A6): p. 616-626.
19. Coelho, M.C. and N. Harnby, *Effect of Humidity on Form of Water-Retention in a Powder.* Powder Technology, 1978. **20**(2): p. 197-200.
20. Hooton, J.C., et al., *An atomic force microscopy study of the effect of nanoscale contact geometry and surface chemistry on the adhesion of pharmaceutical particles.* Pharmaceutical Research, 2004. **21**(6): p. 953-961.
21. Lampenscherf, S., W. Pompe, and D.S. Wilkinson, *Stress development due to capillary condensation in powder compacts: A two-dimensional model study.* Journal of the American Ceramic Society, 2000. **83**(6): p. 1333-1340.
22. Halsey, T.C. and A.J. Levine, *How sandcastles fall.* Physical Review Letters, 1998. **80**(14): p. 3141-3144.
23. Israelachvili, J.N., *Intermolecular and surface forces: with applications to colloidal and biological systems.* 1985, London; Orlando, [Fla]. Academic Press. xv, 296 p.
24. Rabinovich, Y.I., et al., *Capillary forces between surfaces with nanoscale roughness.* Advances in Colloid and Interface Science, 2002. **96**(1-3): p. 213-230.
25. T.Gillespie and W.J.Settineri, *The effect of capillary liquid on the force of adhesion between spherical solid particles.* journal of Colloid and Interface Science, 1967. **24**: p. 199-202.
26. Gao, C., *Theory of menisci and its applications.* Applied Physics Letters, 1997. **71**(13): p. 1801-1803.
27. Farshchi-Tabrizi, M., et al., *On the adhesion between fine particles and nanocontacts: An atomic force microscope study.* Langmuir, 2006. **22**(5): p. 2171-2184.
28. Ata, A., Y.I. Rabinovich, and R.K. Singh, *Role of surface roughness in capillary adhesion.* Journal of Adhesion Science and Technology, 2002. **16**(4): p. 337-346.
29. Rabinovich, Y.I., et al., *Adhesion between nanoscale rough surfaces - I. Role of asperity geometry.* Journal of Colloid and Interface Science, 2000. **232**(1): p. 10-16.
30. Suihko, E., et al., *Prediction of contact angle for pharmaceutical solids from their molecular structure.* Journal of Pharmaceutical Sciences, 2005. **94**(4): p. 745-758.
31. Coughlin, R.W., B. Elbirli, and L. Vergaraedwards, *Interparticle Force Conferred by Capillary-Condensed Liquid at Contact Points.1. Theoretical Considerations.* Journal of Colloid and Interface Science, 1982. **87**(1): p. 18-30.

5 Relative importance of inter-particle van der Waals force, capillary force and electrostatic force

5.1 Comparison of the magnitude of theoretical inter-particle force

Van der Waals force, capillary force and electrostatic forces are the three main force components contributing to inter-particle adhesion interactions. In the previous three chapters the magnitude of each force component was determined by experimental approaches, the relationship between each force component and the crucial particle properties was discussed, and the modeling prediction of each force component was developed. In addition, it is of interest to explore the relative importance of each force component so as to find out the most critical parameters to control the inter-particle adhesion interactions.

The magnitude of theoretical inter-particle forces as functions of particle diameter were compared in previous literatures[1, 2] and the results are shown in Figure 5-1. Solid lines indicate maximum force values obtained at perfect smooth contact while dashed lines indicate asperity-to-plane contact. Several points to note from the graph are:

(1) If perfect smooth contact is assumed, all three inter-particle forces exceed particle gravity for particles below about 500 μm in diameter; if asperity contact is assumed, inter-particle forces and particle gravity are comparable for particle sizes of order 100 μm.

(2) If perfect smooth contact is assumed, the capillary force is dominant over the van der Waals force and electrostatic force, and the electrostatic force is one to two order of magnitude lower than the other two force components; if asperity contact is assumed, the capillary force, van der Waals force and electrostatic force are comparable to each other;

(3) If perfect smooth contact is assumed, the capillary and van der Waals forces increase in proportion to particle diameter, and the electrostatic force increases in proportion to the square of particle diameter; if asperity contact is assumed, the capillary and van der Waals forces are independent of particle diameter.

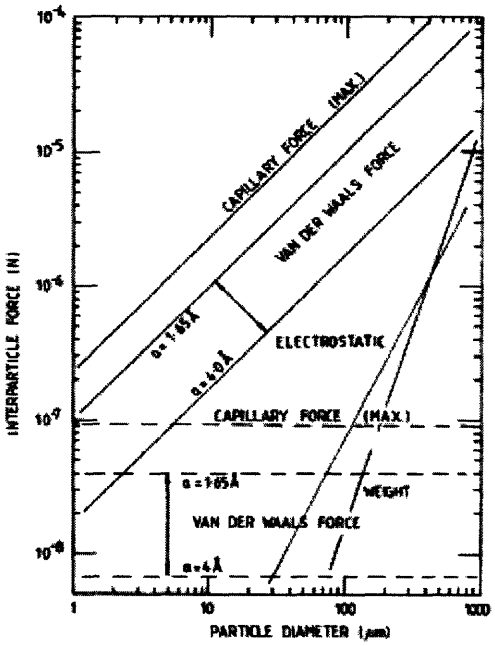

Figure 5-1 Comparison of the magnitude of theoretical inter-particle forces for single-point contact between equal spheres in air (dashed lines indicate asperity-to-plane contact) [2]

These results imply that inter-particle forces are affected to a great extent by surface contact geometry, and it turns out that the theoretical inter-particle forces with respect to the asperity contact are more appropriate to represent the real cases of inter-particle interactions. All these findings are consistent with our research results presented in the first few chapters.

In our force models, inter-particle forces were calculated at the scale of asperity size of order 100-1000 nm instead of particle size of order 100 μm. The theoretical force values are in the order of nanonewtons, in accordance with experimental results. For particles with nanoscale surface roughness, the calculated van der Waals force spreads in the range of 10-160 nN, comparable to the calculated capillary force of 20-80 nN. The theoretical electrostatic force depends heavily on the magnitude of surface charges. Since surface charges are transient and unstable, the electrostatic force is more difficult to be predicted than the van der Waals and capillary force. Theoretically it may vary from zero to as high as 10^4 nN.

Comparison between the magnitude of electrostatic force and that of van der Waals force of powder particles without adequate constraints is unable to yield definite conclusions. Both forces are shown to have the possible magnitudes under certain conditions to significantly

influence the behavior of fine powder particles. However the value of both forces for particles of the same size may vary in a range over one order of magnitude because of varied surface morphologies or surface charge distribution. Theoretically, because the electrostatic forces are proportional to the square of particle diameter for the same charge distribution, the van der Waals forces become relatively more significant as the particle size decreases[3].

5.2 Comparison of the magnitude of experimentally measured inter-particle forces

Since the inter-particle forces of measured pharmaceutical particles are mainly controlled by the microscopic fine structures on the particle surface, they are expected to be relatively insensitive to the particle size. Based on the experimental measurement results, for excipient particles (lactose and MCC) with particle sizes of order 100 μm and asperity sizes of order 100 nm, the van der Waals force varies from 40 nN to 120 nN, and the capillary force ranges from 30 nN to 90 nN. The electrostatic force is relatively smaller than the other two force components, varying from a few nN to as high as 60 nN.

The three inter-particle forces were separated from the total adhesion force by controlling the relative humidity condition during the measurement. The van der Waals force exists all the time during the particle-particle contact, whereas the capillary force only appears with the formation of liquid meniscus and the electrostatic force relied on the presence of surface charges. Therefore, the relative importance of inter-particle forces was discussed in terms of three types of environmental conditions.

At low relative humidity region (0-20% RH), the contribution of the capillary force to the total adhesion interaction is negligible. Van der Waals force becomes dominant. In rare cases when particles carry large amounts of surface charges, the contribution of electrostatic force also should be taken into account. The total adhesion force is constant over this region.

With the increase of relative humidity, moisture influences the intermolecular forces between solid particles in humid environment in at least three ways: (a) it may adsorb on the surface and influence the surface energy, (b) it may alter the surface conductivity and, consequently,

the electrostatic charging of particles; (c) it may condense in the capillary regions contiguous to the areas of contact. When the thickness of the water layer adsorbed on the particle surface grows with the relative humidity, the distance between two surfaces reduces, leading to an increased vdW force. However, on the other hand, with the formation of liquid bridge between the contact interfaces, the contact regions are no longer acting through air but rather through liquid. Since the Hamaker constant of a material in air is usually much lower than that in water[4], the magnitude of the van der Waals force for solids through water is generally significantly less than in air. Thus the contribution of the van der Waals force to the adhesion will decrease to a great extent. Meanwhile, because the dielectric constant of water is 80 times higher than air, the electrostatic charges decay much faster in humid environment than in dry air and the electrostatic force correspondingly decreases at medium-to-high relative humidity conditions. In contrast, the capillary force keeps increasing with the elevated relative humidity. The rate of increase is dependent on the hygroscopicity of the material and hydrophilicity of the contact surface.

When the relative humidity is above the critical point (>60%) and the surface contact area is completely filled with condensed water, the capillary force becomes dominant over the van der Waals and electrostatic forces. In this region, affected by the decreased pressure difference on the water-air interface, the capillary force will decrease slightly.

By and large, with the elevation of the relative humidity, the cohesion force will transit from the vdW force dominant regime to the mixed vdW-capillary regime, and then the capillary regime, as shown in Figure 5-2. The electrostatic force generally plays a less important role in particle adhesions than the van der Waals and capillary forces except for some highly charged particle systems. For example, a previous study[5] on the adhesion forces of toner and polymer particles to aluminum substrates concluded that electrostatic force are usually predominant for the moderately charged particles on a PTFE substrate at a low relative humidity while the van der Waals forces are predominant for the moderately charged particles on a metal substrate at a low relative humidity. The capillary force is most predominant at relative humidity higher than 70%.

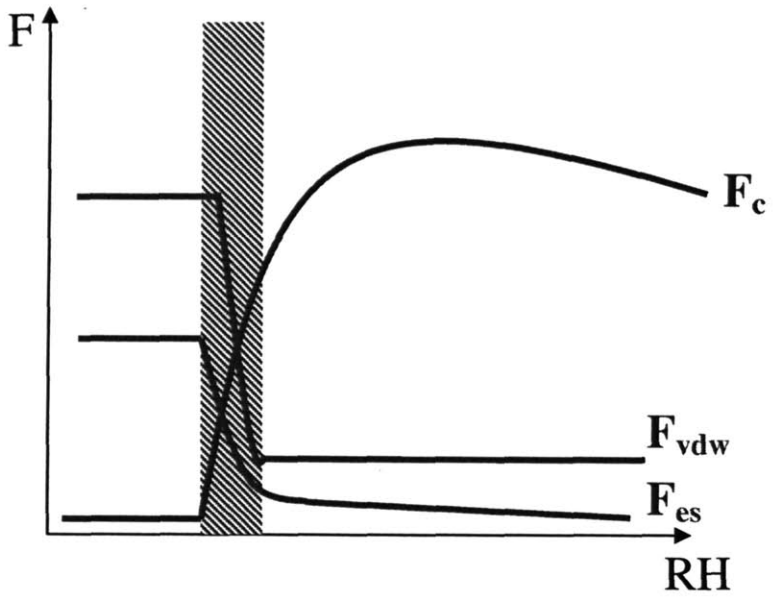

Figure 5-2 Sketch of relative important between van der Waals force, capillary force and electrostatic force at different relative humidity regions

In industrial practice, most operations are run at medium relative humidity condition. In this case, both vdW force and capillary force make important contributions to the inter-particle adhesion interactions. Take the cohesion force data between individual lactose particles measured at 45% RH as an example. If assuming the van der Waals force measured in dry air is constant when the relative humidity is lower than the critical RH level, the magnitude of capillary force at RH of 45% can be estimated from the difference between the total cohesion force and the vdW force. Table 5-1 lists the total adhesion force, the vdW force and the capillary force of five pairs of lactose particles measured by the AFM. The ratio of the vdW force to the capillary force indicated that the magnitudes of the two force components are comparable to each other at medium RH level.

Table 5-1 Comparison of the magnitude of the vdW and capillary forces at RH=45%

Particle No.	1	2	3	4	5
F_total (nN)	84	66	30	36	131
F_{vdw} (nN)	49	40	13	9	64
F_c (nN)	35	26	17	27	67
F_{vdw}/F_c	1.4	1.5	0.8	0.3	1.0

In a word, when evaluating the inter-particle adhesion forces, the relative importance of the three force components may be changed for varied particle systems and different environmental conditions. Generally speaking, the van der Waals force and the capillary force both play important roles in particle adhesion. In some cases such as highly charged system in low RH, the contribution of the electrostatic force also requires special consideration. In the next three chapters, the influences of the three most critical parameters affecting the three inter-particle force components on the powder blending performance will be discussed. It will be shown that the van der Waals force, the capillary force and the electrostatic force all have significant impact on bulk powder flow behavior.

5.3 References

1. K.Gotoh,H.Masuda and K.Higashitani, *Powder Technology Handbook(Second Edition, Revised and Expanded)*. 1997: Mercel Dekker Inc., p.140.
2. J.P.K.Seville,U.Tuzun and R.Clift, *Processing of Particulate Solids*. 1997: Blackie Academic & Professional, p.124.
3. J. Q. Feng,D. A. Hays, *Relative importance of electrostatic forces on powder particles.* Powder Technology, 2003. **135**: p. 65-75.
4. Y. I. Rabinovich, et al., *Capillary forces between surfaces with nanoscale roughness.* Advances in Colloid and Interface Science, 2002. **96**(1-3): p. 213-230.
5. M. Takeuchi, *Adhesion forces of charged particles.* Chemical Engineering Science, 2006. **61**(7): p. 2279-2289.

6 Effect of Surface roughness on powder blending process

6.1 Introduction

It has been pointed out in the first few chapters that surface roughness is one of the most crucial particle properties to affect inter-particle cohesion force at the micro-scale level, especially the van der Waals force. Intuitively, the surface roughness variation is expected to influence the powder flow behavior at the macro-scale level as well. Previous studies showed that by modifying the surface morphologies of individual drug particles, the inter-particle adhesive force can be decreased, leading to a lower angle of repose value or better powder flowability[1]. Similarly, in dry powder inhalation studies, it was found that surface treatment of lactose carrier particles can reduce the adhesion force of fine drug particle to the lactose particle surface and enhance the separation of drug particles due to its surface-smoothing effect[2, 3]. In this work, the surface morphologies of lactose particles were modified by a particle smoothing process with aqueous ethanol solution. The changes in surface roughness and the inter-particle adhesion forces before and after processing were identified by the atomic force microscopy (AFM) technique. The effect of surface modification of lactose particles on bulk powder blending performance was investigated as well.

6.2 Experimental

6.2.1 Surface treatment of lactose particles

In these experiments, an effort was made to prepare lactose particles of different surface morphologies by a process referred to as 'Particle smoothing' method[3]. Approximately 30g lactose particles (Pharmatose® DCL14, DMV Inc., Netherlands) was added into 200ml 70% v/v ethanol solutions in a beaker, and the mixture was stirred at the medium speed for 10 min and then filtered. The processed particles were washed with pure ethanol and dried in air. The same procedures were repeated to get more surface-modified lactose particles with a different processing time of 20 and 30 minutes, respectively.

6.2.2 Surface characterization of lactose particles

Crystallinity of original and processed lactose particles was analyzed by X-ray powder diffraction. The surface morphological modification was observed qualitatively by the Environmental Scanning Electron Microscopy (ESEM). In the meantime, the surface roughness of individual particles was measured by the Atomic force Microscopy (AFM) using a silicon nitride cantilever (spring constant ~0.4N/m) under the contact mode and represented by the root-mean-square (RMS) value.

6.2.3 Measurement of inter-particle adhesion force

For each of four different lactose particle samples, two lactose-adhered cantilevers were prepared. The spring constant of each cantilever was determined by the Molecular Force Probe (MFP) beforehand. With the AFM force volume mode, the cantilevers were used to measure the interactions with a total of 15 individual lactose particles and 15 individual anhydrous caffeine particles (CAS Number: 58-08-2, Sigma-Aldrich, St. Louis, MO). The inter-particle adhesion forces of lactose with lactose and of lactose with caffeine were evaluated.

6.2.4 On-line monitoring of blending kinetics of lactose-caffeine system

The blending experiments of lactose as excipient and caffeine as API were conducted in a lab-scale stainless steel V-type blender (see Figure 6-1). The rotation speed of 10 rpm, the fill volume of 60% and the API concentration of 5% were kept constant for all the blending experiments. The lactose and the caffeine powders used in the blending experiments were pre-sieved to a size range of 90-120 μm and 40-90 μm, respectively. The blending kinetics were monitored non-invasively by the light-induced fluorescence (LIF) technique. During the blending process, the LIF sensor (Honeywell Sensing and Control, Freeport, IL) was positioned near to the blender sending and receiving light signals through the transparent quartz window mount on the blender. Since caffeine and lactose have different fluorescence spectra, by selecting a set of appropriate optical filters (Omega Optical XF-01 filter, Brattleboro, VT) to control the excitation wavelengths incident on and the emission

wavelengths reflected back, the concentration variation of caffeine powders with blending time can be followed in real time.

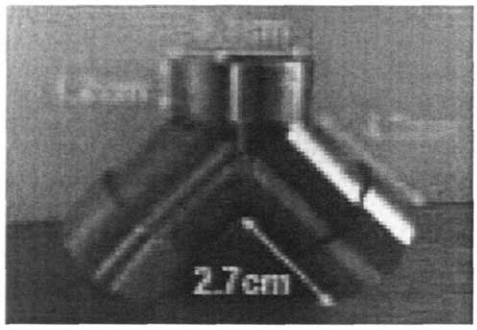

Figure 6-1 Configuration of lab-scale V-type blender

6.3 Results and discussions

6.3.1 Surface modification of lactose particles

To test if the 'particle smoothing' method with aqueous ethanol solution affects the surface chemistry or the crystallinity of lactose particles, samples from original lactose particles and lactose particles processed for 10 min, 20 min and 30 min were analyzed by the X-ray powder diffraction technique, respectively. The pattern of powder diffraction peaks can be used to quickly identify materials, and changes in peak width or position can be used to determine crystal size, purity, and texture. As shown in Figure 6-2, the unprocessed and processed lactose particles appeared to have similar diffraction spectrum, indicating that no phase change or ethanol residual on the particle surface was found due to the particle smoothing process.

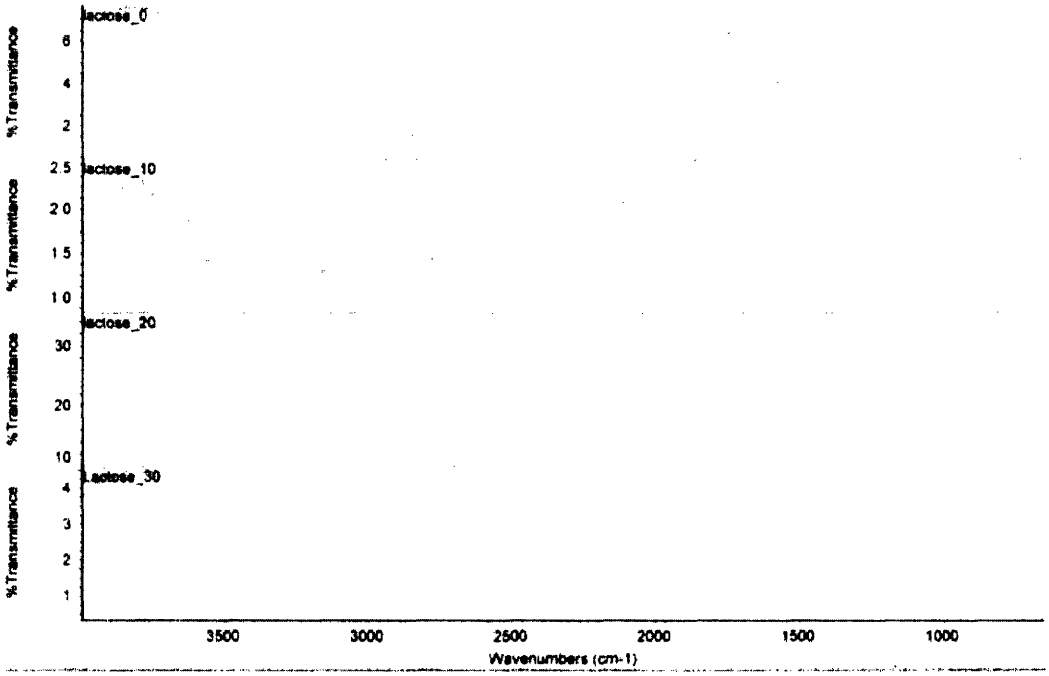

Figure 6-2 X-ray powder diffraction spectrum of lactose particles (from top to bottom: unprocessed, processed for 10 min, processed for 20 min and processed for 30 min)

The difference in the surface roughness between original and processed lactose particles was examined by AFM. The RMS distributions of 15 unprocessed and processed lactose particles were plotted in Figure 6-3. The mean RMS value for processed lactose particles was reduced to 80 nm compared to 93nm for original lactose particles. In addition, among the processed lactose particles, about one quarter of the sample particles have reduced RMS values to 50 nm and below, while for the unprocessed lactose particles the minimum RMS value is higher than 50 nm. However, due to the limited sample size and the nature of surface heterogeneity of particle itself, the RMS value shows a wide distribution for both the original and the processed particles. Statistically there is no significant difference in surface roughness for the four types of lactose particles. Nonetheless, the surface morphological modification can be observed directly by the Environmental Scanning Electron Microscopy (ESEM). As shown in Figure 6-4, the shapes of processed lactose particles were kept about the same as original particles, while their surface asperities were obviously smoothed out more or less with dissapperance of protuberances or projections on the particle surfaces. This together with the AFM data confirmed the smoothing effect of surface treatment of lactose particles.

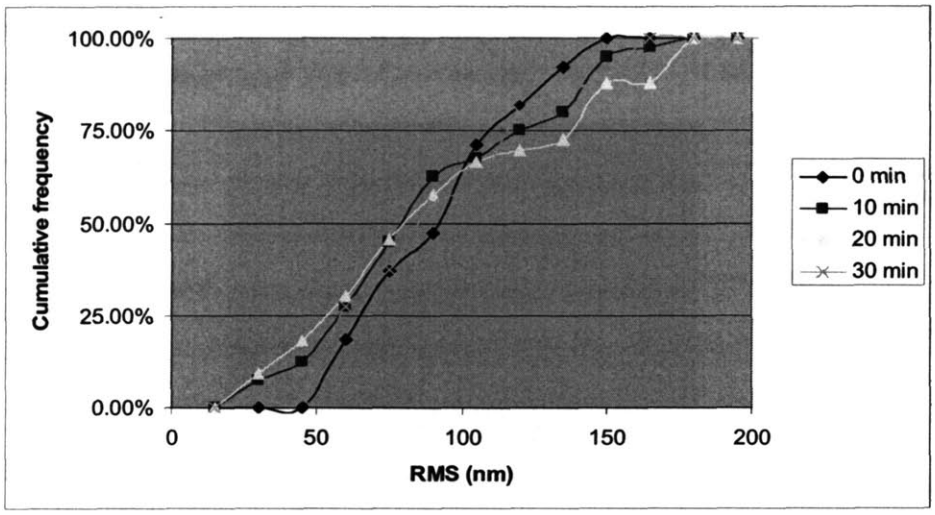

Figure 6-3 RMS frequency distribution of unprocessed and processed lactose particles

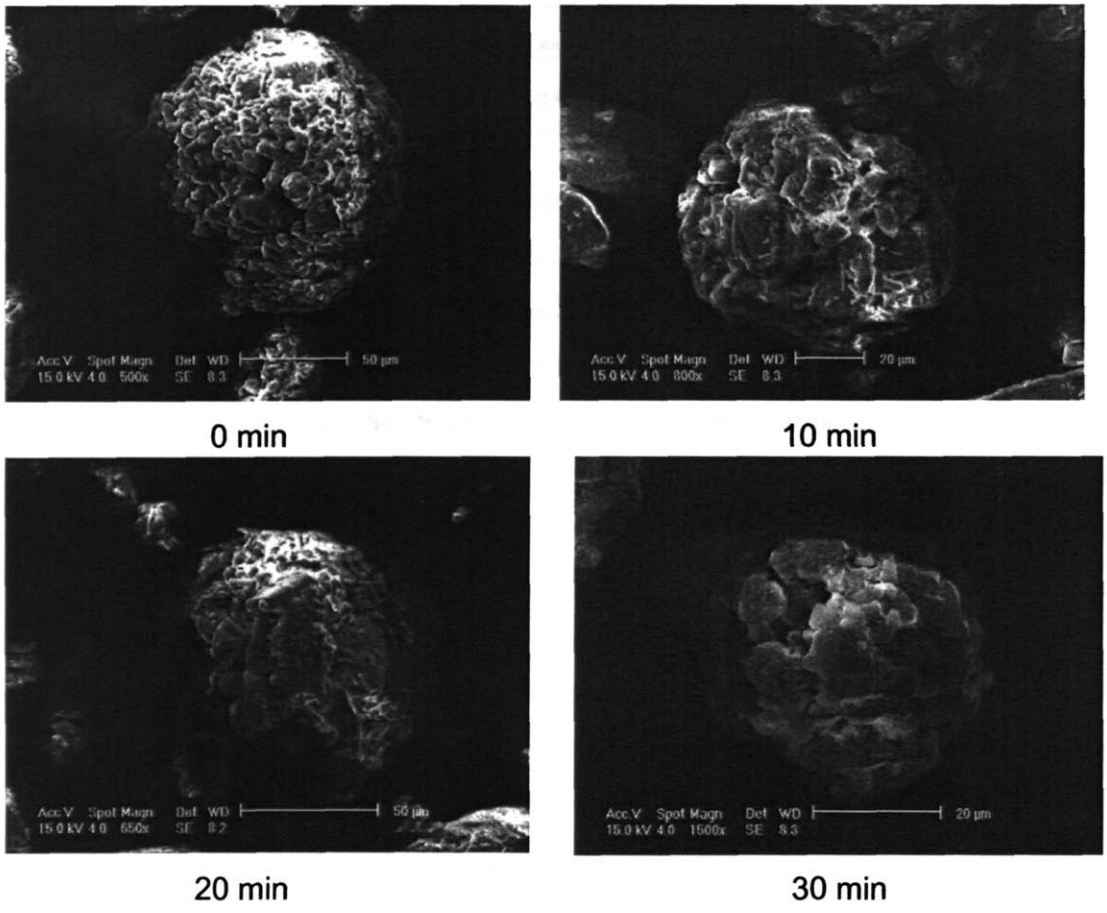

Figure 6-4 ESEM pictures of surface morphologies of lactose particles (top left: unprocessed lactose; top right: lactose processed for 10 minutes; bottom left: lactose processed for 20 minutes; bottom right: lactose processed for 30 minutes)

6.3.2 Evaluation of inter-particle adhesion force

The inter-particle adhesion forces of 15 pairs of lactose particles were measured by the AFM for each of the four types of lactose samples. As shown in Figure 6-5, the lactose-lactose cohesion forces of surface-smoothed lactose particles are 1.5~3 times higher than that of unprocessed lactose particles. Similarly, the lactose-caffeine adhesion forces were also enhanced for the surface-smoothed lactose particles. This result was consistent with the theoretical finding in the Chapter 2, which stated that inter-particle van der Waals force increases with the decrease of surface roughness. Generally particles with smoother surfaces tend to have higher surface area of contact, and correspondingly higher cohesion interactions than rougher particles.

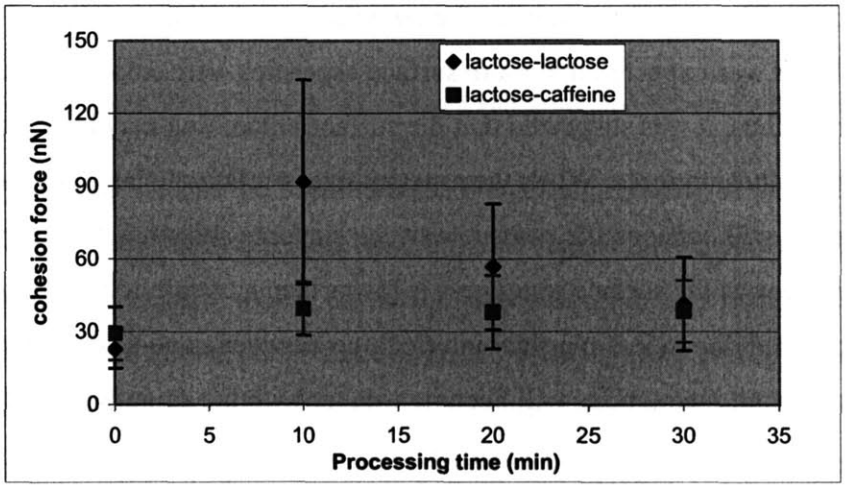

Figure 6-5 Cohesion/adhesion force for unprocessed and processed lactose particles

A statistical T-test was conducted on the inter-particle lactose-lactose and lactose-caffeine adhesion force data and the p values were listed in the Table 6-1 and Table 6-2. If the p value is smaller than 0.05, the two mean force values to be compared are considered to be significantly different. It can be seen that the inter-particle lactose-lactose cohesion force and the inter-particle lactose-caffeine adhesion force of the three groups of processed lactose particles are all significantly different than those of unprocessed lactose particles. While the force difference between groups of processed lactose particles are not so significant.

Table 6-1 *p* value of statistical T-test for lactose-lactose cohesion force data

p	0 min	10 min	20 min	30 min
	F=23±8 nN	F= 92±42 nN	F= 57±26 nN	F= 41±19 nN
0 min		0	0.001	0.003
10 min			0.021	0.001
20 min				0.106

Table 6-2 *p* value of statistical T-test for lactose-caffeine adhesion force data

p	0 min	10 min	20 min	30 min
	F=29±11nN	F= 39±11 nN	F= 38±15 nN	F= 38±13 nN
0 min		0.017	0.011	0.044
10 min			0.78	0.815
20 min				0.935

An interesting trend observed from Figure 6-5 is that for the processed lactose particles, apparently the average inter-particle adhesion force decreased with the processing time. While data shows no significant difference in surface roughness among three types of processed lactose particles, it was expected that more surface asperities were smoothed out at longer processing time. Thus, it was suspected that the surface smoothing may have a trade-off effect on inter-particle adhesion force. When the asperity size is relatively large, the decrease in surface roughness will enhance the contact between surfaces and strengthen particle interaction, whereas as the surface roughness is lower than a certain level, the surface contact area may be reduced due to less physical interlocking between nano-scale asperities. In that case particle adhesion interactions will become weaker with the smoothing of the surface, as observed in our experiments and in some literature[2, 3]. Further investigation is needed in the future to elucidate quantitatively the relationship between the surface roughness and the actual surface contact area.

6.3.3 Evaluation of blending performance of lactose-caffeine system

In the blending experiments caffeine is the fluorescent material to be monitored by the LIF sensor. Therefore, the LIF signal deviation corresponds to the caffeine concentration variation within the blender, and its time dependence reflects the blending kinetics of the monitored system. As shown in Figure 6-6, the LIF signal deviation data was converted to the relative standard deviation of caffeine concentration, which decays with blending time. It appeared that the blending curve of unprocessed lactose with caffeine had a lot more fluctuation and took longer time to the steady state than the processed lactose system. Here a blend is

considered to have reached homogeneity when a 90% drop in RSD is observed. As a result, the average time to get to the blend homogeneity for the system of original lactose and 10 min, 20 min, 30 min-processed lactose is 8.2min, 2.3min, 4.5min and 3min, respectively.

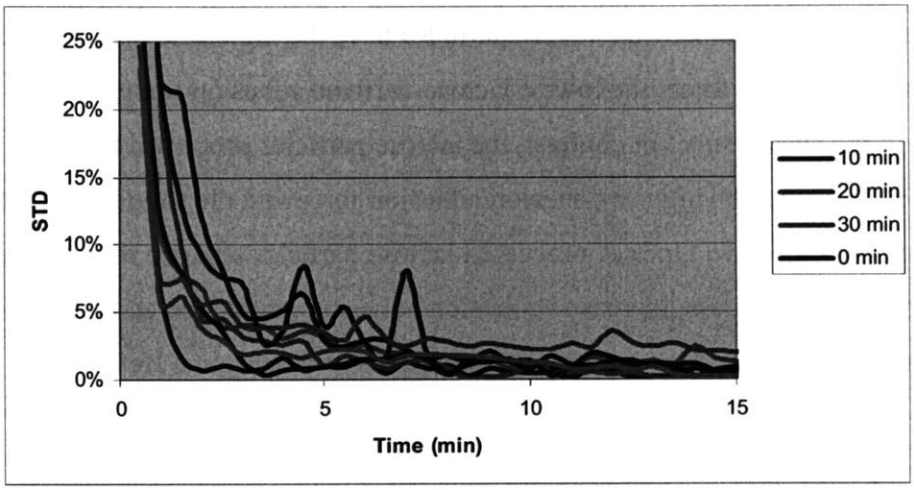

Figure 6-6 Blending kinetic curves of unprocessed and processed lactose mixed with caffeine

The statistical T-test shows that the times to reach blend homogeneity of the three processed lactose systems are significantly different ($p<0.05$) than that of the unprocessed lactose system (see Table 6-3). In other words, the surface-smoothed lactose system requires less time to reach steady state than unprocessed lactose system. There are two plausible reasons to explain the effect of surface modification on the blending kinetics: first, the increase of inter-particle adhesion force between excipient and API particles is advantageous for the formation of an ordered mixture, in which the two different ingredients are held together and stabilized by inter-particle interactions; second, surface modification may have an effect not only on inter-particle adhesion force, but also on inter-particle friction force and physical interlocking in powder flow movement. Smoother particles are expected to have less inter-particle friction force, which is probably in favor of powder flow. A further study on this topic in the future work will allow us to better understand the surface smoothing effect on bulk powder flow behavior.

Table 6-3 *p* value of statistical T-test for time of blend homogeneity of lactose-caffeine system

p	0 min	10 min	20 min	30 min
	T=8.2±1.2 min	T= 2.3±0.8 s	T= 4.5± 0.5 s	T= 3.0±1.0 s
0 min		0.003	0.019	0.006
10 min			0.02	0.581
20 min				0.015

6.4 Summary

Table 6-4 summarizes the surface roughness values, the cohesion/adhesion force values and the time to get to blending uniformity for both the unprocessed and the surface-smoothed lactose particles. The unprocessed lactose particles have the highest RMS value, the lowest lactose-lactose cohesion force, the lowest lactose-caffeine adhesion force, and the longest time to get to the steady state. In contrast, the lactose particles processed for 10 minutes have the lowest RMS value, the highest cohesion/adhesion force and the shortest time to get to the steady state. The other two types of processed lactose particles also are shown to have decreased surface roughness, increased cohesion/adhesion interaction and the reduced blending time to get to the blend uniformity compared to the original lactose.

Table 6-4 Surface roughness, cohesion/adhesion force and the time required to get to the blend uniformity for unprocessed and processed lactose particles

Process Time	0 min	10 min	20 min	30 min
Median RMS (nm)	93±28	78±41	79±49	80±37
L-L cohesion (nN)	23±8	92±42	57±26	41±19
L-C cohesion (nN)	29±11	39±11	38±15	38±13
Time to steady state (min)	8.2±1.2	2.3±0.8	4.5±0.5	3.0±1.0

The results suggested that the microscopic particle surface roughness has prominent influence on the particle interactions as well as the blending behavior of bulk powders. It also implies that choosing the excipient particles with smoother surfaces may enhance the cohesion/adhesion forces between particles and facilitate the blending performance by reducing the time required to get to the blend uniformity.

6.5 References

1. Y. Kato, et al., *Evaluation of the flowability of surface-modified preparations by the measurement of the inter-particle adhesive force.* Journal of Drug Delivery Science and Technology, 2005. **15**(3): p. 217-221.

2. P. M. Young, et al., *Characterization of a surface modified dry powder inhalation carrier prepared by "particle smoothing".* Journal of Pharmacy and Pharmacology, 2002. **54**(10): p. 1339-1344.
3. K. Iida, et al., *Preparation of dry powder inhalation by surface treatment of lactose carrier particles.* Chemical & Pharmaceutical Bulletin, 2003. **51**(1): p. 1-5.

7 Effect of electrostatic force on powder blending process

7.1 Introduction

In pharmaceutical systems, many particle materials are electrically insulating so that the electrostatic charges will unavoidably be generated and retained in the manufacturing process. The electrostatic charges of different polarities give rise to attractive or repulsive electrostatic forces between individual particles. As a result, electrostatic charging may cause the agglomeration or segregation of particles during powder dispersion, transport and other handling process. Its effect on powder blending homogeneity is of great interest in our study and manufacturing.

A lot of work has been done in investigating the effect of electrostatic charge on drug-carrier interactive system. In Staniforth's work it was found that optimization of the triboelectric charging conditions may improve the stability of an ordered powder mix. When the drug and excipient particles carried opposite charges, the mix was less prone to segregation[1]. Kulvanich and his coworkers found that the total adhesion interaction between drug and excipient particles decreased with the electrostatic charge decay during the storage[2]. Another study carried out by Murtomaa and Laine showed that the charging behavior of glucose may be changed drastically with the addition of lactose particles into the powder flow. Lactose tended to adhere to the contact surface more easily than glucose, resulting in the electrostatic separation and the variation of the powder concentration until a steady state of charging was reached. Further studies on glucose mixing with other pharmaceutical powders such as starch, dicalcium phosphate and magnesium stearate indicated that appropriate additives can be used to reduce the static electricity generated in the process[3, 4]. Rowley also observed the change in API concentration in dry powder inhalation (DPI) formulations after triboelectrification with steel and polyamide contact surfaces. The preformulation study on the charge propensity of API and excipient particles may provide valuable information in the design and manufacture of pharmaceutical delivery systems[5]. Electrostatic charge accumulation caused

by the interparticulate or particle/wall collision during the pharmaceutical manufacturing operations also may lead to the contact surface contamination of equipments by charged particles. The contaminating particles and different cleaning method have significant effects on the charging behavior of powders and thus introduce variations during the processing.[6]

In this study, three different types of blending experiments were conducted. The first is the conventional blending process without any control on electrostatic charges. Keeping all the operational conditions constant, the second blending process was carried out aligned with a charge neutralization apparatus. The third experiment was to mix excipient and API components carrying opposite charges well controlled by corona-charging approach. The blending homogeneity of each blending method was then analyzed to see how the electrostatic charging will affect the blend quality.

7.2 Experimental

7.2.1 Blending process with uncontrolled electrostatic charges

Lactose particles (Pharmatose DCL14, DMV International, Netherlands) were blended with 2 wt% anhydrous caffeine (CAS Number: 58-08-2, Sigma-Aldrich, St. Louis, MO) in a ϕ45mm×21mm circular stainless steel blender for 30 minutes with constant rotation speed of 10 rpm and fill volume of 40%. 10 samples were taken from different locations of the final blend using a grounded metal spatula. The sample weight is around 1-1.5g, comparable to the weight of a tablet dose. The net charge-to-mass ratio of each sample was determined by the charge-to-mass ratio test system (Model 210-HS, Trek Inc., NY, USA) together with a balance (Mettler Toledo, Switzerland). Subsequently the concentration of caffeine in each sample was analyzed by the UV spectroscopy. The same experiment was repeated three times and a total of thirty samples were collected and analyzed.

The same blending experiments were conducted for several other binary systems including lactose-5% caffeine system, lactose-10% caffeine system and MCC-5% caffeine system. In addition, another blending experiment was implemented on the lactose-5% caffeine system

where the pure lactose particles were blended for 1 hour in advance of the addition of caffeine. Each system has a sample size of 30.

7.2.2 Blending process with electrostatic charge neutralization

In this experimental setup, an air ionizer was connected with the middle of a stainless steel cylinder blender (ϕ40mm×70mm) by an inserted tube (ϕ15mm×30mm). Both ends of the blender were sealed with a fine stainless steel mesh screen whose nominal screen pore opening is 20 μm. Lactose and caffeine were pre-sieved to a size range of 90-120 μm and 40-90 μm, respectively. Therefore ionized air was blown into the blender and out through the screen during the blending process without causing the loss of powders. The blender configuration and the experiment set-up is shown as Figure 7-1 and Figure 7-2.

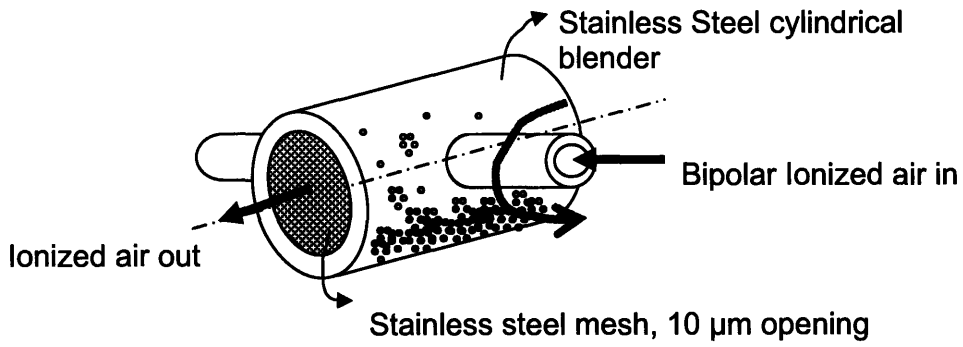

Figure 7-1 Schematic of rotating blender with ionized air flowing through

The fill volume, the rotation speed and the blending time were fixed at 50%, 10 rpm and 15 minutes, respectively. As the control experiment, blending of lactose with 2 wt% caffeine was first conducted without turning the ionizer on. Then 10 samples were taken from the final blend and the caffeine concentration of each sample was analyzed by the UV spectroscopy. The experiment was repeated three times and a total of thirty samples were analyzed in the end.

Following the control blending experiments, lactose was mixed with 2 wt% caffeine again with air ionizer on and all other operating conditions unchanged. The only difference is, to ensure the charges inside the blender were neutralized sufficiently, the original 15-min

blending process was segmented as three 5-min blending with 10-minute pause in between for an extended charge neutralization period. Likewise, the experiment was repeated three times and a total of 30 samples were analyzed by the UV spectroscopy in the end. The same experiments were conducted to lactose-5 wt% caffeine system and lactose-10 wt% caffeine system as well.

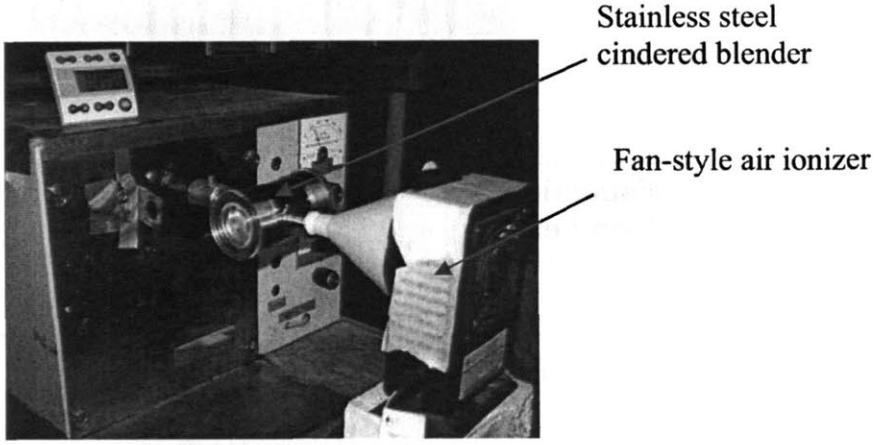

Figure 7-2 Experiment setup for the blending with charge neutralization

7.2.3 Blending process with controlled corona charging

As one of the most widely used charging mechanism in industrial practice, corona charging is applied in our study to charge pharmaceutical particles. The basic mechanism of corona charging is described as follows. In a strong electrical field with sufficiently high voltage, if there is enough charge concentrated in a small enough space, individual electrons can be torn off of air molecules. This process is called ionization, and if it is intense enough, results in the formation of a region known as a corona. The corona containing free electrons provides a pathway for current to flow from the charging electrode into the surrounding air. In a negative corona charging process, free electrons are repelled from the fringes of the corona and captured by an oxygen molecule to form a negative oxygen ion. In a positive corona, a nitrogen molecule which has given up an electron will become a positive nitrogen ion. It is these ions which do the actual charging of powder. Since the particles have a higher dielectric constant than the air around them, the field will be concentrated near the particles. So the ions with a net charge will be urged toward the particles and transfer charge to the particle until the particle reaches the maximum surface charge and begin to repel the incoming ions[7].

A self-designed corona charging apparatus was applied in this experiment to make excipient and API particles carry charges of opposite polarities before the blending. The experiment setup is shown in
Figure 7-3 and Figure 7-4.

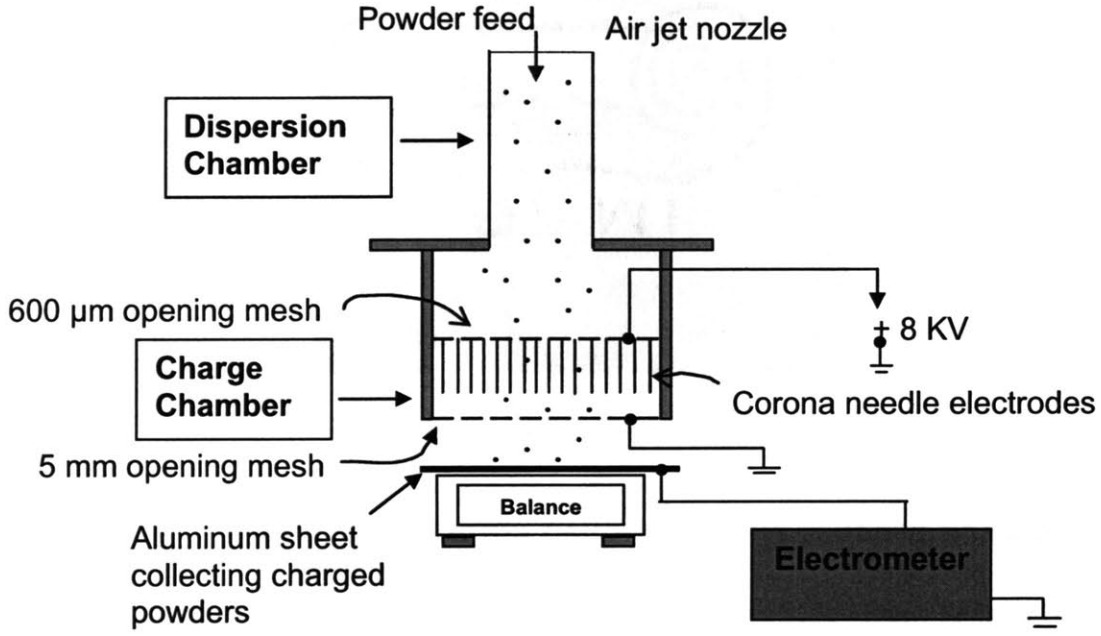

Figure 7-3 Schematic of corona charging apparatus

The key element of corona charging apparatus consists of a bunch of needle electrodes (Ø0.5mm×40mm) which were mount on a 600 μm opening stainless steel sieve and connected to a high voltage power supply. The polarity and the amount of the charges generated on the particles were controlled by the high voltage power supply. In our study a voltage of ±8.0 kV was used to provide the corona electrical field. Dry powders were fed from the top of the dispersion chamber by an aspirator. The dispersed powders went through the dispersion chamber, got charged in the charge chamber, and then fell through a grounded 5 mm opening stainless steel mesh 2 cm away from the charge chamber. Finally the charged particles were deposited on the top of an aluminum sheet at the very bottom. The sheet was placed on the top of an electronic balance (PE-3000, Mettler, Switzerland) and connected with

an electrometer (Model 6514, Keithey, USA) so that the weight and the electrostatic charges of the powders collected on the sheet can be measured in real time.

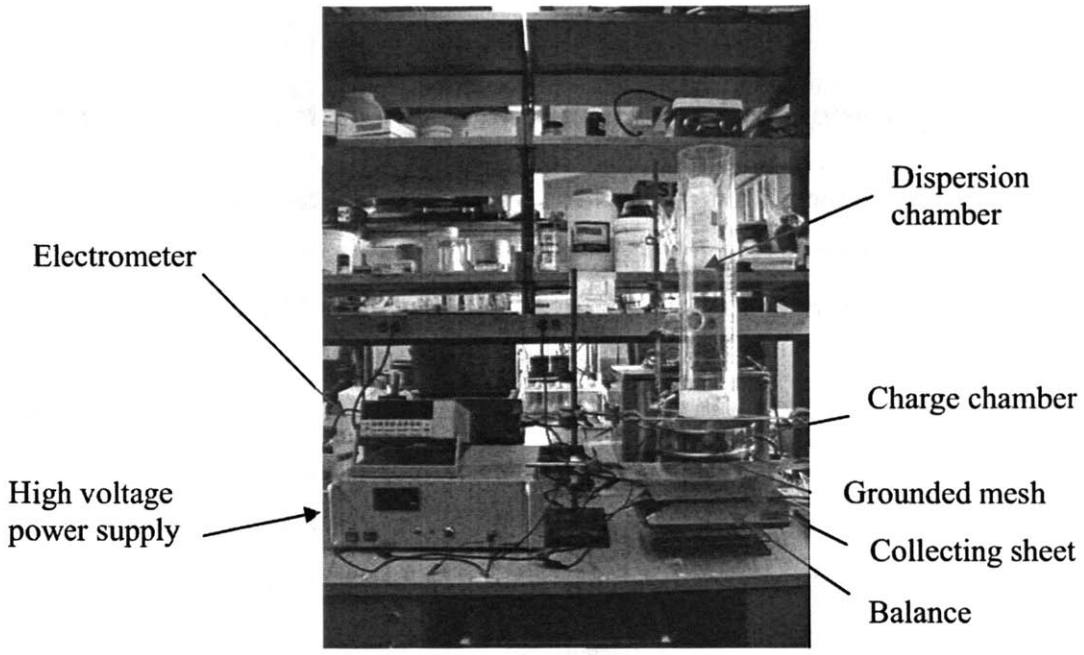

Figure 7-4 Experimental setup of corona charging

As the control experiment, lactose was blended with 2 wt% caffeine first without any charging procedures in a stainless steel blender (Ø40mm×70mm) for 15 minutes. The fill volume and the rotation speed were fixed at 50% and 10rpm, respectively. The same experiment was repeated three times. 15 samples were taken from the final blend for each run of the blending experiments. The caffeine concentration of each sample was tested by the UV spectrometry (λ=274nm, Model 8452A, Hewlett Packard, USA).

In the following experiment, lactose was positively charged in a +8 kV electrical field and caffeine negatively charged in a -8 kV electrical field. The two charged components were then mixed together with a caffeine concentration of 2 wt% at the same operation conditions as the control experiments. The experiment was repeated three times and the sample size was 15 for each run.

Similarly, the blending procedures were repeated for the lactose-2% caffeine system but with lactose negatively charged and caffeine positively charged. In addition, the electrostatic-

charged blending experiments were also implemented for two other binary systems, lactoe-5 wt% caffeine and MCC-2 wt% caffeine.

7.3 Results

7.3.1 Blending homogeneity with uncontrolled electrostatic charges

The concentration variation was defined as the error of the actual caffeine concentration of each sample relative to the target caffeine concentration. Lower concentration variation and narrower concentration variation distribution correspond to higher blending homogeneity.

For the blending system of lactose-2 wt% caffeine, lactose-5 wt% caffeine and lactose-10 wt% caffeine, the cumulative frequency distribution of the caffeine concentration variations of 30 samples was plotted with respect to different charge-to-mass ratio ranges in Figure 7-5(a-c), respectively. It appeared that most samples with lower charge-to-mass ratios tend to have lower concentration variation, implying that the electrostatic charging effect will affect the blending homogeneity adversely.

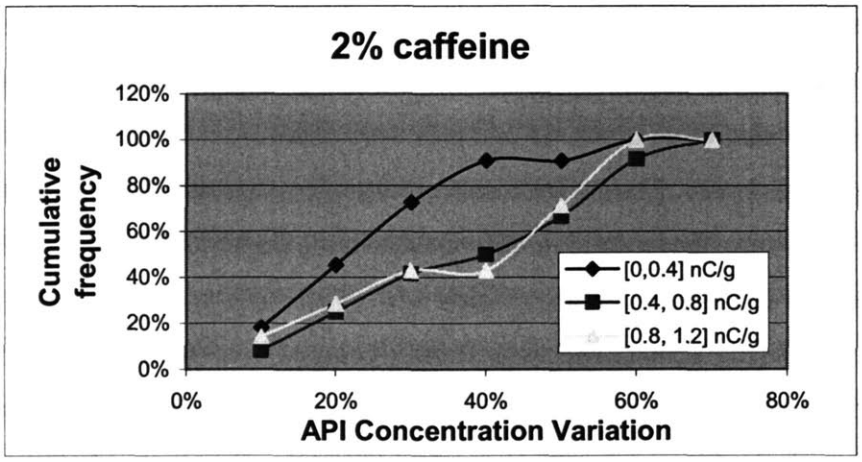

(a)

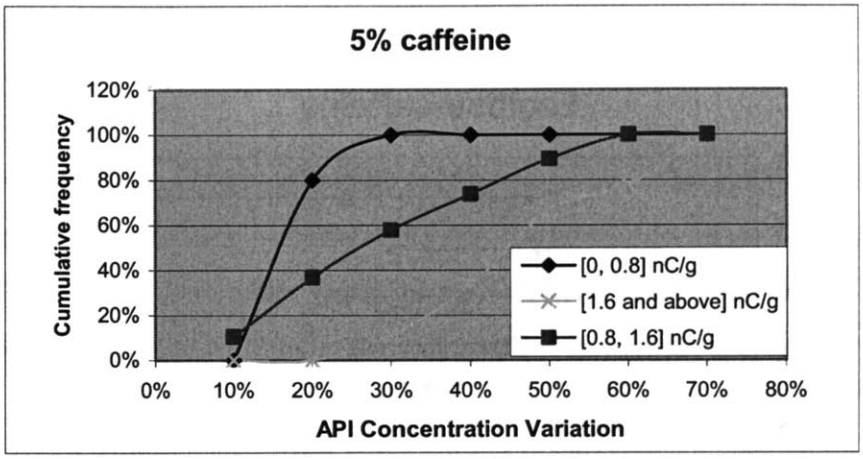

(b)

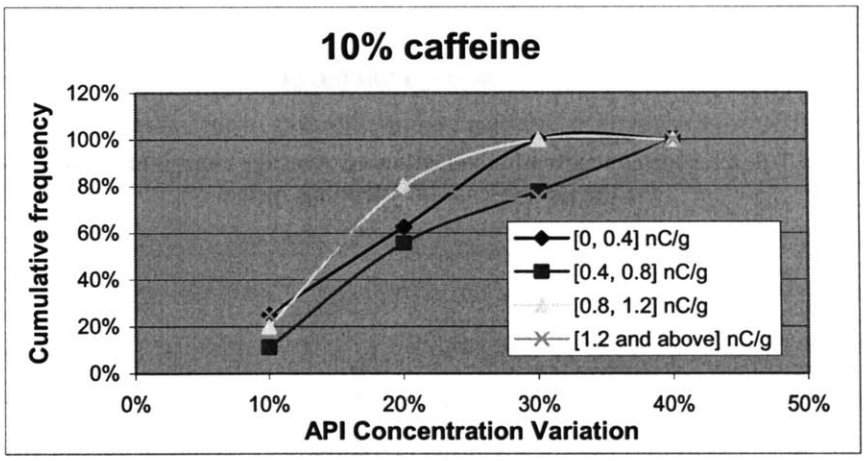

(c)

Figure 7-5 Concentration variation for lactose-caffeine blend with different charge-to-mass ratio (a) 2 wt% caffeine in blend; (b) 5 wt% caffeine in blend; (c) 10 wt% caffeine in blend

To observe more clearly the dependence of concentration variation on the charge-to-mass ratio, the concentration variation data of all the 90 samples obtained from 3 sets of lactose-caffeine blending experiments was sorted and segmented into different groups. The average concentration variation of each group against the corresponding average charge-to-mass ratio of this group was plotted in Figure 7-6. It can be seen that there is a positive correlation between average concentration variation and the average charge-to-mass ratio. The higher the average charge-to-mass ratio, the higher the average concentration variation is. Accurate measurement of electrostatic charges is a very challenging task. Not surprisingly, the charge-to-mass data collected in our experiments showed a large variance due to the limitation of the measuring instrument as well as the transient and irreproducible feature of electrostatic charging process itself.

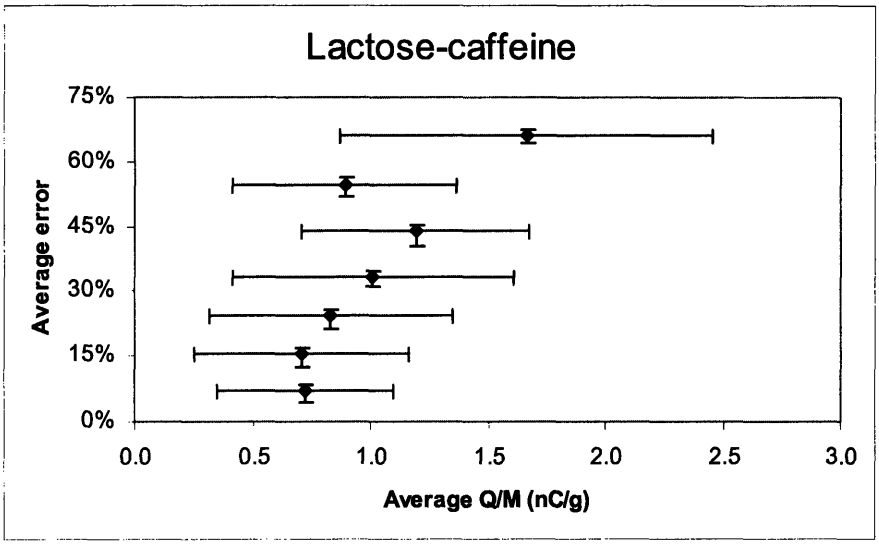

Figure 7-6 Average concentration variation vs. Average charge-to-mass ratio for the lactose-caffeine blending system

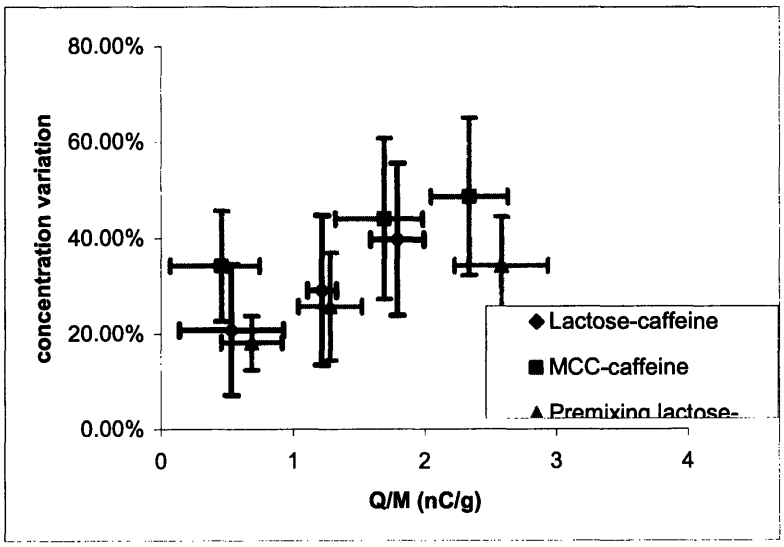

Figure 7-7 Concentration variation vs. Charge-to-mass ratio for three different blend system

The similar trend for the lactose-caffeine system was observed for the MCC-5 wt% caffeine system and premixed lactose-5 wt% caffeine system as well. With the increase of the average charge-to-mass ratio, the average concentration variation increases, as demonstrated in Figure 7-7. Under the same blending conditions, the MCC-caffeine system showed a higher

electrostatic charge distribution and also a higher concentration variation than the lactose-caffeine system.

It was observed in the experiments that the powders sticking on the stainless steel surface of the blender are mostly caffeine particles and their charge-to-mass ratios are much higher than those of samples inside the blender, partly because particles of smaller particle size (caffeine powder in our case) tend to be more easily charged than larger particles (lactose particles in our case). It was suspected that concentration variation within the final blend was partly caused by the loss of active ingredient to the wall of the blender. In the blending of premixed lactose with caffeine, lactose has been mixed in the blender for a certain period of time before the addition of caffeine. it was found that its blend homogeneity was improved slightly compared to the lactose-caffeine system despite its higher electrostatic charge distribution. A plausible explanation is that premixing of lactose inside the blender allowed lactose particles to be charged and adhered to the wall, thus more or less preventing caffeine powders added in the subsequent step from sticking to the wall. Unfortunately, no experiments have been carried out in this study to validate this hypothesis due to the limitation of the measuring approach. Further investigation is necessary in the future to better understand the electrostatic charging behaviors of different materials during the blending process.

7.3.2 Blending homogeneity with electrostatic charge neutralization

Figure 7-8(a-c) shows the comparison of the frequency distribution of API concentration variation between the blending with and without charge neutralization for lactose blending with 2 wt%, 5 wt% and 10 wt% caffeine.

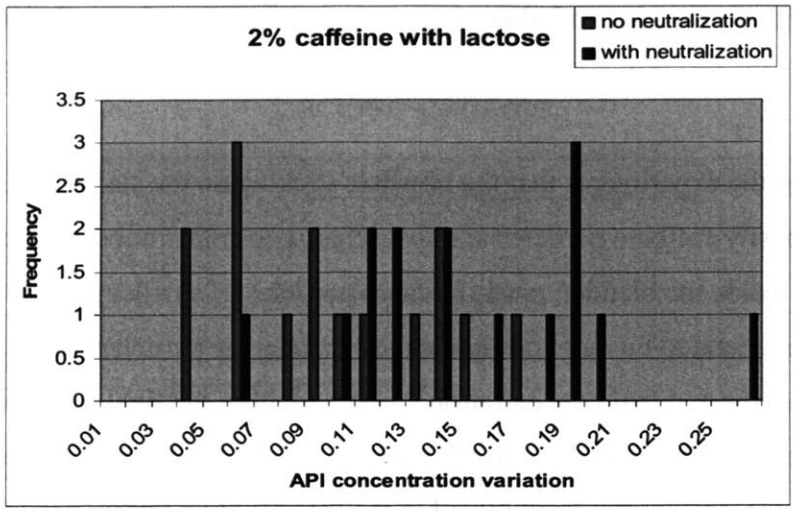

(a)

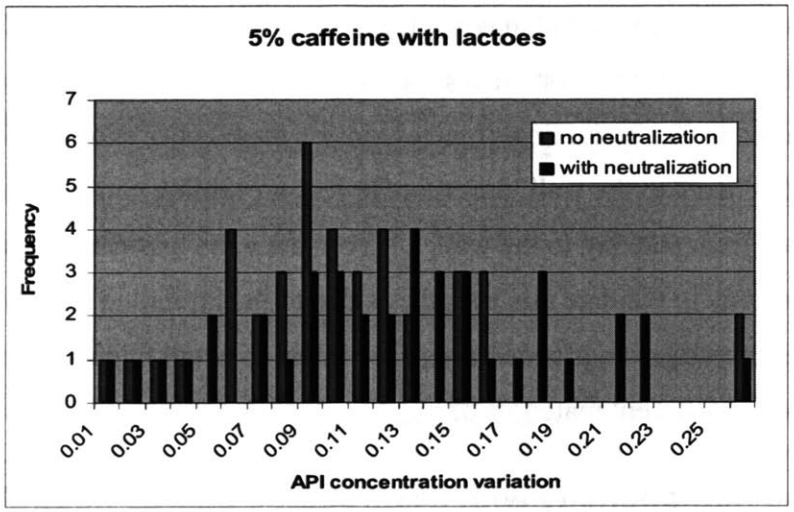

(b)

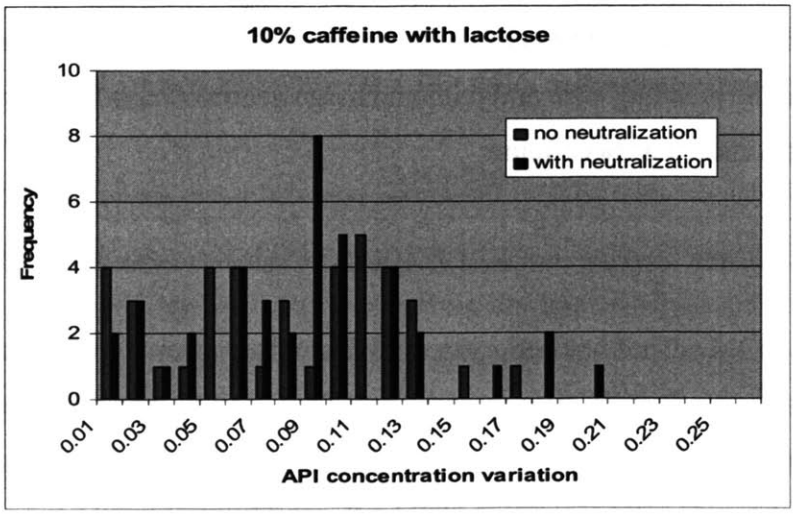

(c)

Figure 7-8 API concentration variation distribution of blending with and without charge neutralization: (a) 2% caffeine with lactose; (b) 5% caffeine with lactose; (c) 10% caffeine with lactose

For all the tested systems, data from blending with charge neutralization showed higher API concentration variation. To see more clearly the effect of charge neutralization on blend homogeneity, the cumulative frequency distributions of API concentration variations of all the 90 samples for both the control experiment and the blending with charge neutralization were plotted in Figure 7-9. Again, blending with charge neutralization has higher API concentration variation than blending without charge neutralization. In other words, to eliminate or minimize the charging effect during the blending process does not improve the blend homogeneity as expected. Instead, the blend homogeneity is reduced.

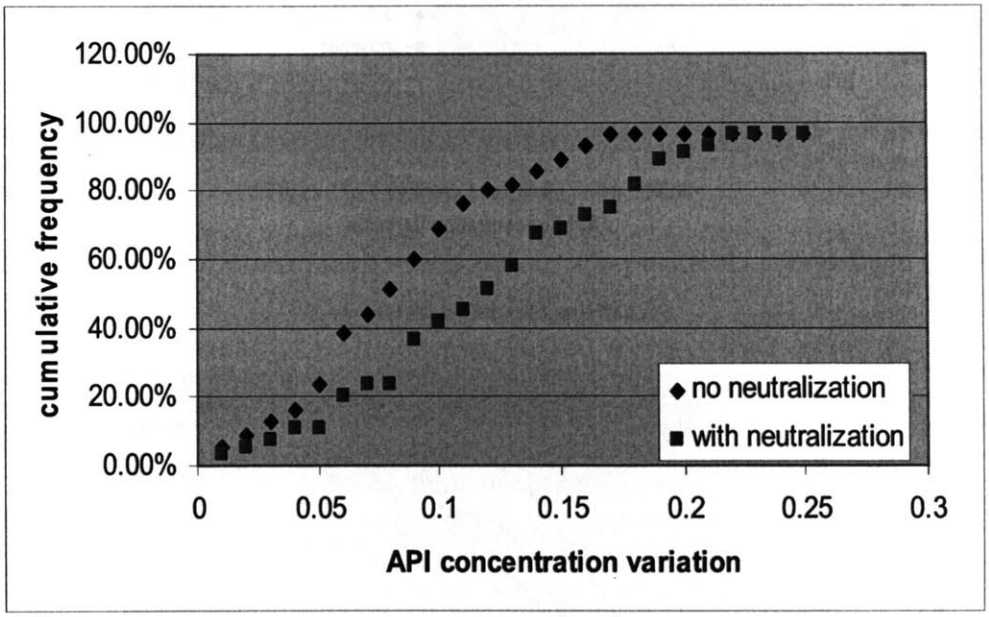

Figure 7-9 Comparison of blend homogeneity between blending with and without charge neutralization

7.3.3 Blending homogeneity with electrostatic corona charging

To investigate whether the controlled electrostatic charging has any effect on blend homogeneity, lactose and caffeine carrying opposite charges were mixed and compared to the control (non-corona charging) blending result. Two cases of corona charging were discussed, one of which was lactose carrying positive charges and caffeine carrying negative charges, the other was lactose negatively charged and caffeine positively charged. The cumulative frequency distributions of API concentration variation for the binary systems of lactose-2

wt% caffeine, lactose-5 wt% caffeine and MCC-2 wt% caffeine were shown in Figure 7-10(a-c).

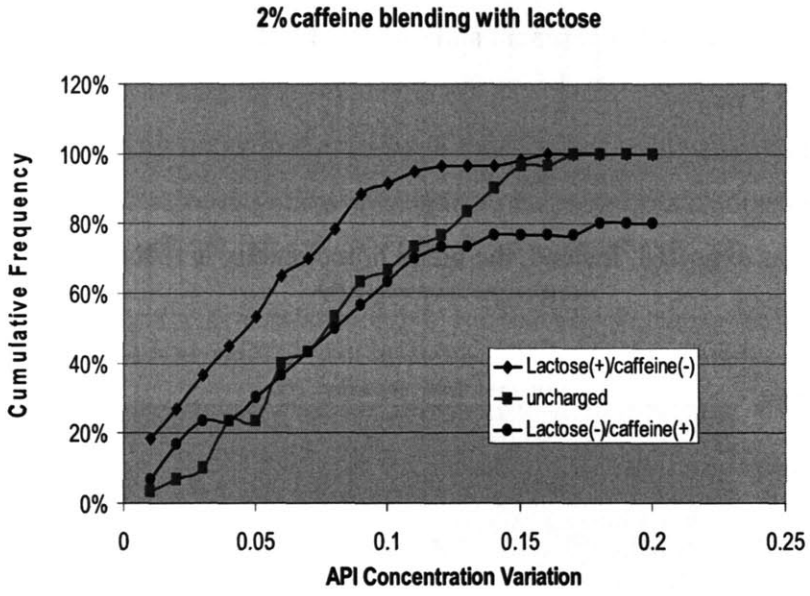

(a)

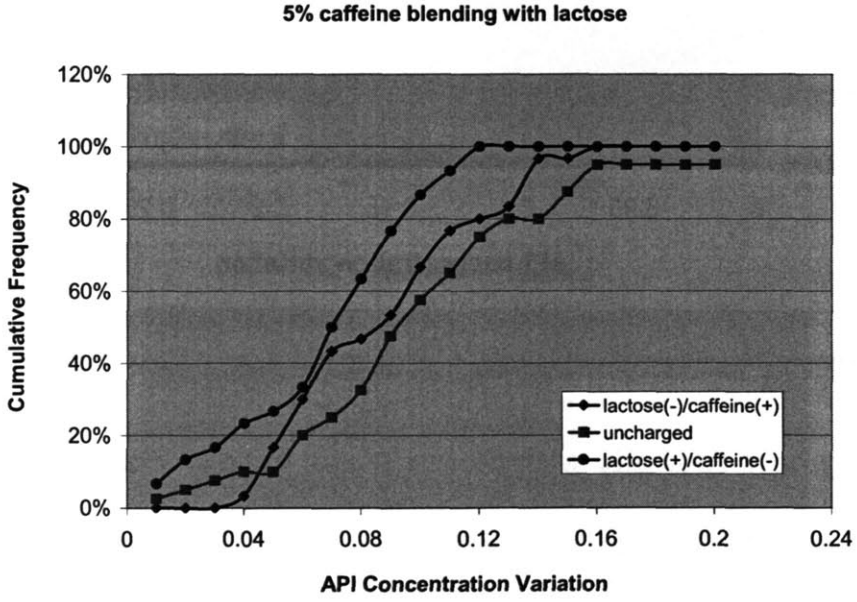

(b)

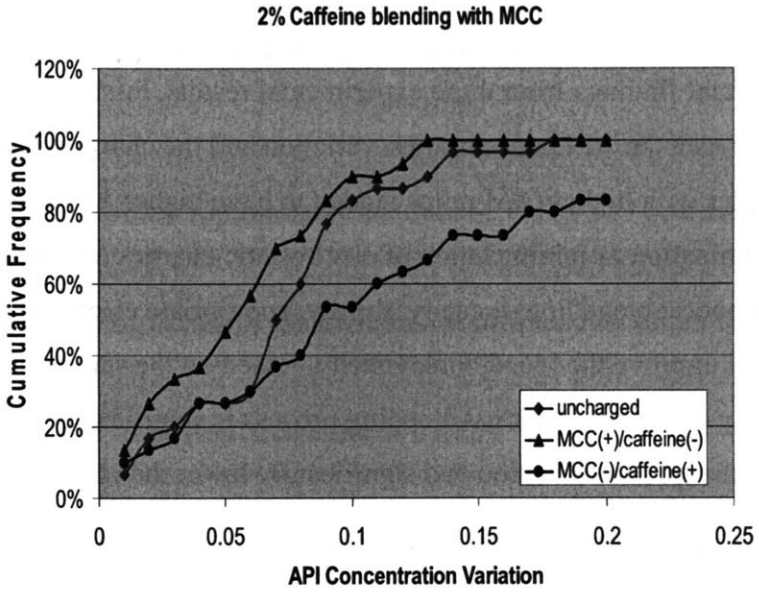

(c)

Figure 7-10 Comparison of API concentration variation between blending with and without charge control: (a) 2% caffeine blending with lactose; (b) 5% caffeine blending with lactose; (c) 2% caffeine blending with MCC

For the lactose-2 wt% caffeine system, when lactose was positively charged and caffeine negatively charged, the blending homogeneity was improved to a great extent compared to the non-corona charging system. As seen from the Figure 7-10(a), about 92% of the samples in the charged blending experiments have the API concentration variation lower than 10%. In contrast, only two thirds of the samples in the uncharged blending experiments achieved 10% or less API concentration variation. Similarly, the blend homogeneity of the lactose-5 wt% caffeine system and the MCC-2 wt% caffeine system were also improved to some extent as a result of the electrostatic corona charging process, as seen in Figure 7-10(b&c).

Interestingly, it was found that when the charge polarities of excipient and API particles were switched, with the same operating conditions, the blend homogeneity was only slightly improved (Figure 7-10b) or even reduced (Figure 7-10 a&c) compared to the non-charged blending process. The implication of this inconsistent charging effect will be discussed in the next section.

7.4 Discussions

There are three important findings from these experimental results. First, the data showed a strong correlation between the API concentration variation and the charge-to-mass ratio of blend samples. Samples with higher Q/M ratios tended to have higher API concentration variation; second, elimination or minimization of electrostatic charges during the blending process resulted in a poorer blend homogeneity; thirdly, appropriate electrostatic charging of excipient and API can improve the blend homogeneity. Based on the statistical analysis result, the blend homogeneity of the conventional blending process is significantly higher than that of the blending with charge neutralization and significantly lower than that of the blending with corona charging process.

The fact that the presence of electrostatic charges may cause particle agglomeration or segregation has been addressed in the literature[8-10]. Particle materials are different in work functions, particle size, surface morphology and surface chemistry. Thus the amount and polarity of electrostatic charges generated during the particle-particle and particle-wall collision vary from one particle to another. Even particles of the same material may carry both positive and negative charges at the same time. Moreover, as stated in Chapter 3, surface charge distribution on individual particles is not uniform either. Although lumps or agglomerates were not observed in our blending experiments, the heterogeneous distribution of electrostatic charges hinders equal chances of interaction between excipient and API particles. As a result, content uniformity within the blend is reduced.

On the other hand, electrostatic attractive force between excipient particles and API particles are desired because it is advantageous for the formation of ordered mixture. It was speculated that the adverse impact of charge neutralization on blend homogeneity is attributed to the reduced cohesion interaction between excipient and API particles. With a weaker electrostatic attractive force bonding particles together, the blend stability is decreased. Because the current measuring technique does not allow us to measure both the electrostatic charges and the inter-particle adhesion force in real time, it is difficult to gather reliable data to verify this

hypothesis. One supportive result was from Kulvanich's study, which showed that electrostatic charge decay led to reduced particle adhesions[2].

Although uncontrolled electrostatic charging has adverse effect on blend homogeneity, if charge polarity is controlled appropriately for excipient and API powders during the blending process, the blend homogeneity and stability can be enhanced because excipient and API powder particles carrying opposite electrostatic charges tend to attract each other due to the strong inter-particle electrostatic attraction forces and thus form more stable ordered mixture. The similar result was addressed in Staniforth's study[1].

As mentioned in the previous section, positively-charged excipient and negatively-charged API resulted in better blend quality. However, when the charge polarity of the two components were switched in the corona charging process, the blend quality became worse. One plausible explanation for this phenomenon is the interaction between the corona charging before the blending and the tribocharging during the blending. Because of the difference in work functions, excipient particles tend to carry positive charges and API particles negative charges during the particle-particle collision. When excipient was negatively charged and API was positively charged by corona electric field, the charging effect was likely to be compromised by the new opposite charges generated during the blending. Therefore the 'oriented' electrostatic attractive forces between excipient and API cannot be strengthened as anticipated. It implied to us that in order to take good advantage of electrostatic charging effect on blending process, further studies need to be done to better understand the complex charging mechanism, including the electrostatic properties of the raw materials, the mechanism of charge generation and dissipation, and all the variables and uncertainties in the electrostatic-charging process.

7.5 References

1. J. N. Staniforth and J. E. Rees, *Electrostatic Charge Interactions in Ordered Powder Mixes.* Journal of Pharmacy and Pharmacology, 1982. **34**(2): p. 69-76.
2. P. Kulvanich and P. J. Stewart, *Correlation between Total Adhesion and Charge Decay of a Model Interactive System During Storage.* International Journal of Pharmaceutics, 1987. **39**(1-2): p. 51-57.

3. M. Murtomaa and E. Laine, *Electrostatic measurements on lactose-glucose mixtures.* Journal of Electrostatics, 2000. **48**(2): p. 155-162.
4. M. Murtomaa, K. Ojanen, and E. Laine, *Effect of surface coverage of a glass pipe by small particles on the triboelectrification of glucose powder.* Journal of Electrostatics, 2002. **54**(3-4): p. 311-320.
5. G. Rowley, *Quantifying electrostatic interactions in pharmaceutical solid systems.* International Journal of Pharmaceutics, 2001. **227**(1-2): p. 47-55.
6. J. Eilbeck, et al., *Effect of contamination of pharmaceutical equipment on powder triboelectrification.* International Journal of Pharmaceutics, 2000. **195**(1-2): p. 7-11.
7. Nordson Corporation, *Corona Charging and Electrostatics for Pipe Coating.* 2004.
8. E. D. Lachiver, et al., *Insights into the role of electrostatic forces on the behavior of dry pharmaceutical particulate systems.* Pharmaceutical Research, 2006. **23**(5): p. 997-1007.
9. F.Muzzio and A. Alexander, *Scale up of Powder-Blending Operations.* Pharmaceutical Technology, 2005: p. s34-s41.
10. Herbert A. Lieberman and Leon Lachman, *Parmaceutical Dosage Forms: Tablets, v.2, p.26*: Marcel Dekker, Inc.

8 Effect of relative humidity on powder blending process

8.1 Introduction

Relative humidity is one of the most important parameters to determine inter-particle capillary force. The dependence of capillary force on relative humidity has been discussed in Chapter 4. Inter-particle adhesion interaction usually increases with elevated relative humidity. When capillary force becomes gradually dominant, bulk powder flow behavior will be affected as a result. In this study, blending at several different relative humidity levels was conducted to see how variation in relative humidity will affect powder blend homogeneity.

8.2 Experimental

8.2.1 Characterization of moisture sensitivity of particles

Defined as the degree to which the quality of a product is impacted even by minimal uptake of water vapor, moisture sensitivity reflects material physical or chemical property changes with varied relative humidity. In our experiments the moisture sensitivity of two excipient materials, lactose (Pharmatose DCL14, DMV International, Netherlands) and microcrystalline cellulose (Celphere CP102, Asahi Kasei Corporation, Tokyo, Japan), were characterized by the critical relative humidity (RH) point at which the surface morphology of particles was observed to change significantly due to moisture effect. ESEM equipment (FEI/Philips XL30 FEG ESEM, FEI Company, Hillsboro, Oregon) was used to take images of particles at different RH levels. To control Relative Humidity (RH) inside the ESEM chamber, a cold stage with a water source was used. After trace amount of the excipient materials were loaded into the ESEM chamber, the chamber was first pumped to ultrahigh vacuum before the electron gun was initiated. Once a high vacuum was achieved and electron gun turned on, the temperature of the cold stage in which the samples were placed was gradually lowered to 1 °C. By referencing the water phase diagram for the dew point at this temperature, the pressure

was slowly increased to introduce moisture inside the chamber. The RH was controlled by traversing the liquid-vapor line in the temperature-pressure phase diagram of water.

8.2.2 Blending with relative humidity control

Two binary blending systems were studied: lactose blending with 2 wt% caffeine and MCC blending with 2 wt% caffeine. Before blending, both excipient and API powders were stored in desiccators for at least 24 hours. The relative humidity inside each desiccator was controlled by desiccants or saturated salt solutions. The selection of types of desiccants or salt chemicals was referred to Perry's handbook [1]. In our study, for example, the desiccator with P_2O_5 had the RH of 5%; the desiccator with saturated $CaCl_2$ solution had the RH of 30%; and the desiccator with saturated NaCl solution had the RH of 60%.

All the blending experiments were carried out inside a closed chamber. The RH inside the chamber was controlled with the same desiccant or saturated salt solutions as used for storage of excipient and API powders. A lab-scale V-type stainless steel blender was used in the blending, as shown in Figure 6-1. The rotation speed, fill volume and blending time were fixed at 10 rpm, 50% and 15 minutes, respectively. After blending, 10 samples were taken from the final blend and the caffeine concentration of each sample was analyzed by UV spectroscopy. The same experiment was repeated three times and a total of 30 samples were collected corresponding to each of the three different RH levels. The exact RH value was monitored by the hygrometer (Traceable®, model 35519-041, Control Company, USA).

8.3 Results and discussion

8.3.1 Moisture sensitivity of lactose and MCC

The surface morphological change of lactose and MCC particles with relative humidity was observed under the ESEM. The appearances of lactose and MCC particles at different RH levels were shown in Figure 8-1 and Figure 8-2.

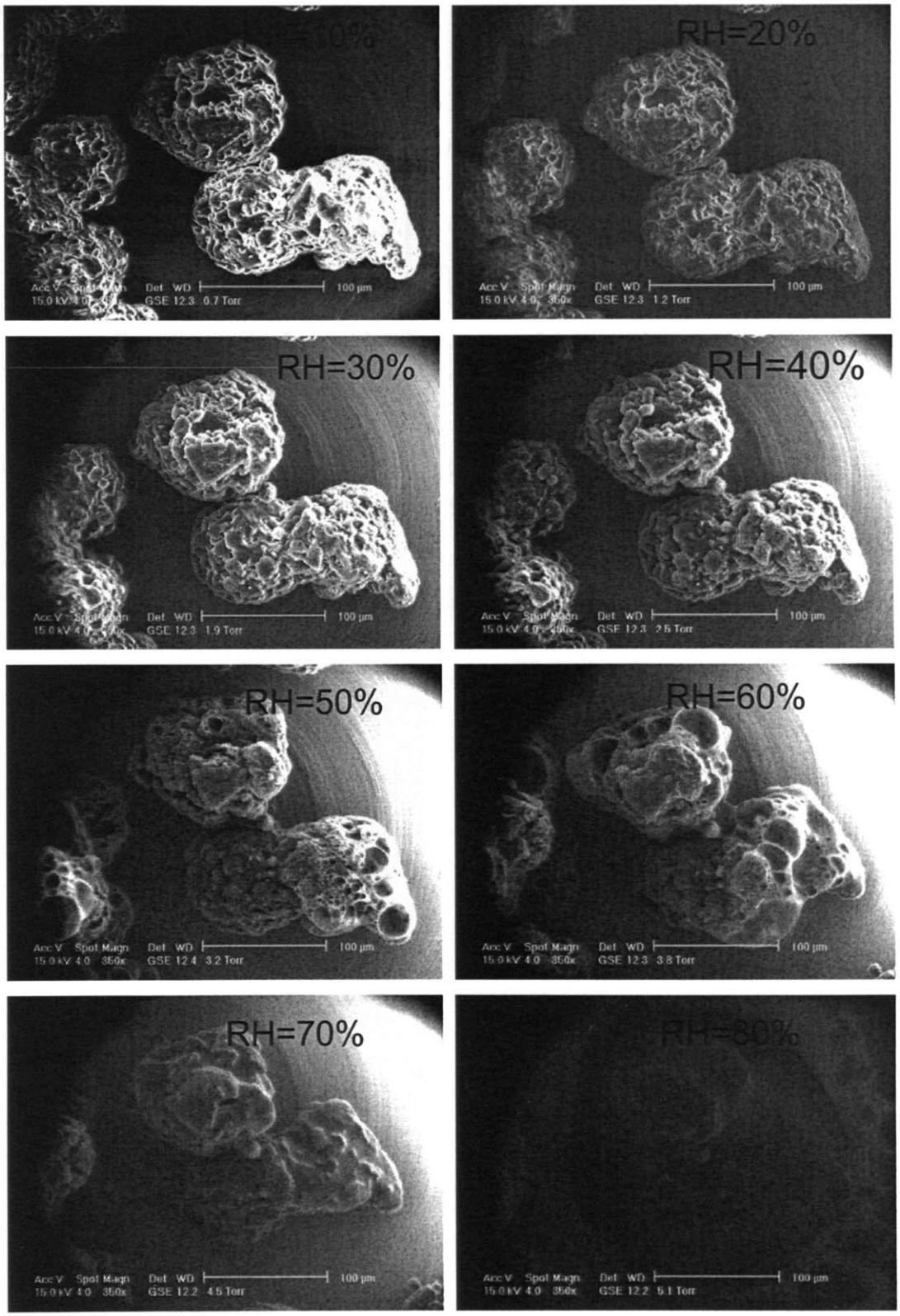

Figure 8-1 Surface morphologies of lactose at different relative humidity levels under ESEM

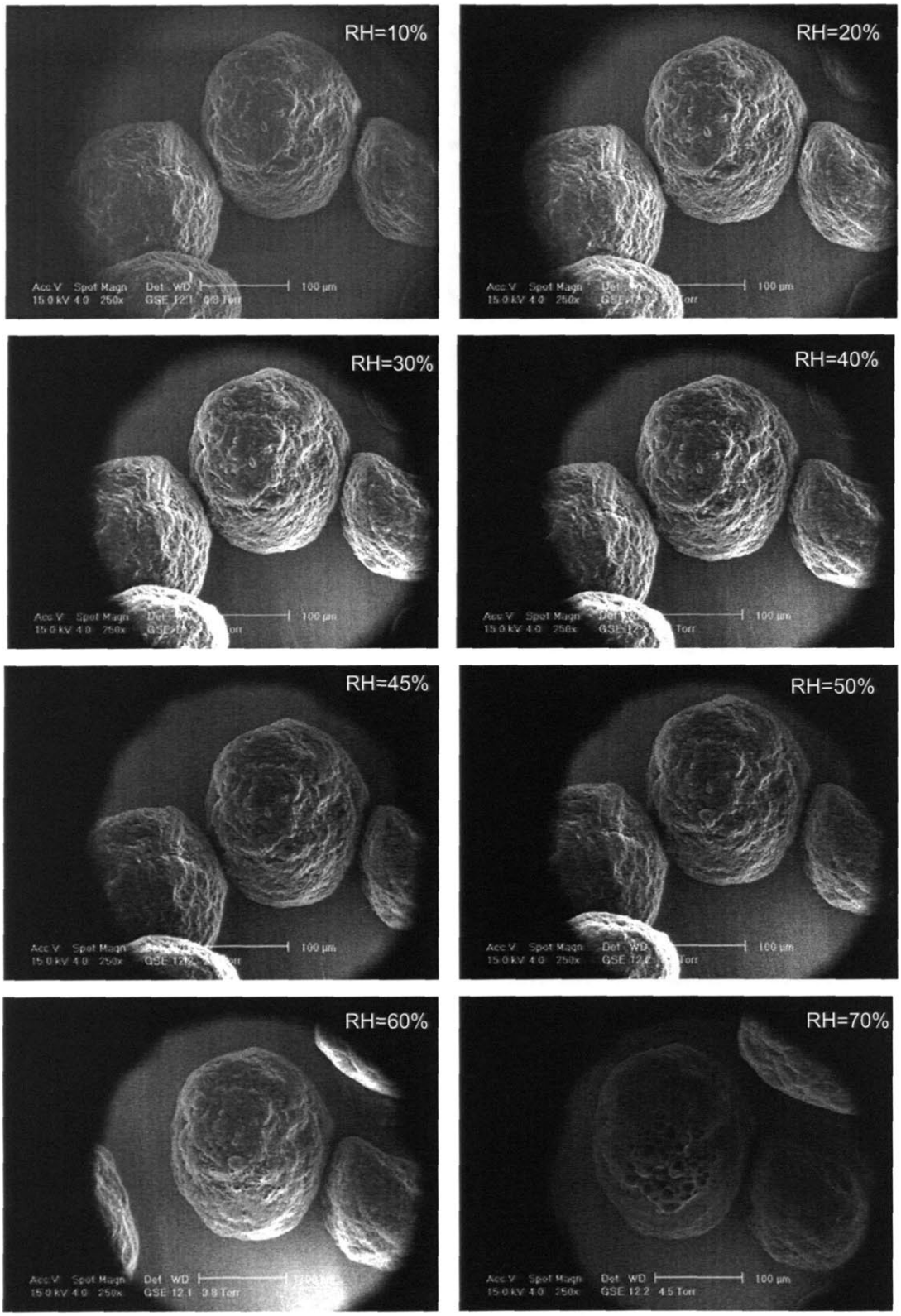

Figure 8-2 Surface morphologies of MCC at different relative humidity levels under ESEM

The relative humidity increased stepwise from 10% to 70-80% for both lactose and MCC sample particles. It can be seen clearly from the ESEM pictures that the surface morphologies of lactose particles became soft and partly melted when the RH was lower than 50%; while for MCC particles the surface morphologies had no significant changes until the RH level reaches 60-70%. This difference indicated that lactose is more moisture sensitive than MCC.

8.3.2 Blend homogeneity at different relative humidity level

For lactose-2 wt% caffeine system, the blending experiments were carried out at the RH of 5%, 30% and 57%, respectively, with all other operating conditions unchanged. The cumulative frequency distributions of caffeine concentration variation obtained at varied RH levels were shown in Figure 8-4(a). Each curve corresponded to a sample size of 30.

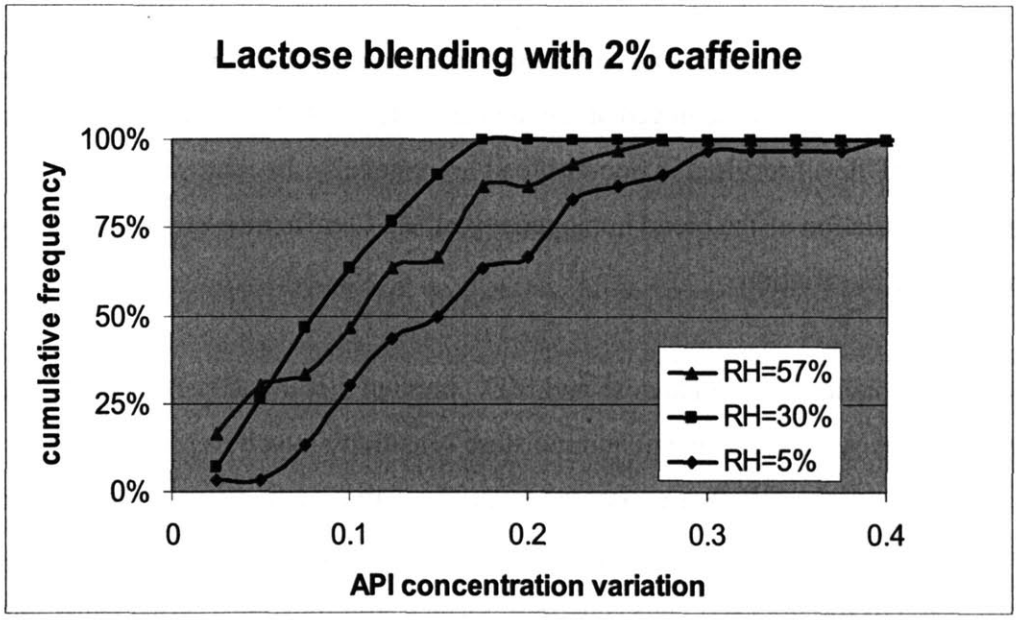

Figure 8-3 Effect of relative humidity on the blend homogeneity for lactose blending with 2 wt% caffeine

Similarly, for MCC-2 wt% caffeine system, the blending experiments were conducted at the RH of 11%, 35% and 65%, respectively. The cumulative frequency distributions of API concentration variation at each RH level were displayed in Figure 8-4.

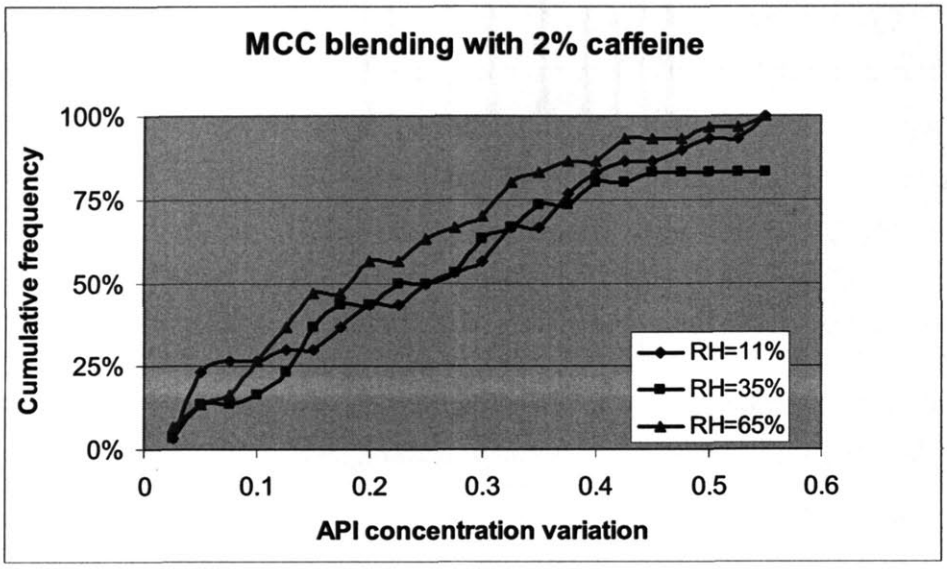

Figure 8-4 Effect of relative humidity on the blend homogeneity, (a) lactose blending with 2% caffeine; (b) MCC blending with 2% caffeine

It was found that the lowest API concentration variation or the best blend homogeneity for lactose-caffeine system was achieved at the medium RH level of 30%. Either decreasing or increasing the RH level resulted in poorer blend homogeneity. In contrast, the API concentration variation or the blend homogeneity of MCC-caffeine system did not change much with the RH variation.

The different behavior between lactose and MCC implied that the RH effect on the blend homogeneity was system dependent and moisture sensitivity may be a critical particle property. For materials of higher moisture sensitivity, variation in relative humidity tends to have more significant effect on blend quality. Too low RH gives rise to sustained electrostatic charging, whereas too high RH causes particle surface softening and consequently particle agglomeration. Both have negative effects on blend homogeneity. Tight control in optimized RH level during powder handling process is favored particularly for moisture sensitive materials to ensure consistency of desired product quality.

8.4 References

1. *Perry's Chemical Engineer's Handbook.* New York: McGraw-Hill, 1997.

9 Conclusion and Impact

9.1 Conclusion

A multi-scale analysis methodology was implemented to link the microscopic particle properties and interactions with the macroscopic powder blending performance. This research is motivated by the fact that most pharmaceutical blending practices depend heavily on trial and error and empirical approaches due to an inadequate understanding of blending mechanism of cohesive fine powder systems. Since dry powder blending is essentially the sum of mutual interactions between numerous solid particles, a profound investigation of particle adhesion interaction and its influence on blending results were accomplished experimentally and theoretically. The materials used in the study are anhydrous caffeine, lactose monohydrate and micro-crystalline cellulose.

First of all, the critical particle characteristics that affect inter-particle adhesion forces including van der Waals force, capillary force and electrostatic force were identified. Several important findings are:

- The magnitude of van der Waals force between particles with rough surfaces is determined by the nanoscale surface asperity size and density rather than the particle size. Particles with smoother surfaces tend to have higher van der Waals force. In addition, materials with higher Hamaker constant and higher elasticity generally have higher van der Waals force.
- The electrostatic force is a strong function of surface charges. Materials with different work functions or with different surface properties may carry surface charges of different polarities and amounts. Surface charge distribution shows a good correspondence to the surface topographic heterogeneity.
- The capillary force is sensitive to the relative humidity, the hygroscopicity of the particle material and the surface contact geometry. Generally the capillary force increases with the elevation of the relative humidity. The rate of increase depends on the hygroscopicity of the material. Particles with stronger moisture absorption capability have more significant increase in capillary force at high relative humidity

levels. Even for the same material, the dependence of the capillary force to the relative humidity of individual particles may be different from each other due to change in liquid meniscus curvature resulted from heterogeneous surface contact geometry.

Secondly, the relative importance of the van der Waals, capillary and electrostatic forces to the total inter-particle adhesion force was evaluated. It was found that the van der Waals force is the dominant adhesion force at low relative humidity; at medium relative humidity the magnitudes of the vdW and capillary force are comparable to each other and both make important contribution to the total particle adhesion. When the relative humidity is beyond 60%, the capillary force becomes dominant over other force components. Electrostatic force is usually several orders of magnitude lower than the vdW and capillary force except for highly charged system in low RH environment. Its importance becomes less at medium to high relative humidity.

Thirdly, three mathematical force models were established to quantitatively describe the relationship between each inter-particle adhesion force component and the particle properties. The van der Waals force model was validated by the experimental data measured by the atomic force microscopy, while the other two force model allowed us to estimate the magnitude of the capillary and electrostatic force between two single particles, despite some discrepancy introduced by the heterogeneity of surface asperity geometry and the variability of surface charges.

Lastly, the impact of critical particle properties and environmental factors on pharmaceutical blending homogeneity was discussed. The findings were summarized as follows:

- When the lactose particles processed by the surface-smoothing method were used as excipient, blend took shorter time to achieve homogeneity than the unprocessed lactose system which has rougher surfaces.
- In terms of electrostatic charging effect, the API concentration variation increases with the charge-to-mass ratio of final blend samples. The charge neutralization during the blending process had negative effect on blend homogeneity. In contrast,

when the positively charged excipient was mixed with negatively charged API powders, the blend homogeneity was greatly improved.

- The effect of relative humidity variation on the blend homogeneity is system-dependent. For excipients with higher moisture sensitivity such as lactose, best blend homogeneity was obtained at medium relative humidity; whereas for excipients with low moisture sensitivity such as MCC, blend homogeneity was not affected much by the change in relative humidity.

9.2 Impact

The primary contribution of this research is the achievement of a fundamental understanding of inter-particle adhesion interaction which plays a key role in blending process as well as in all other solids processing operations. By exploring the qualitative and quantitative relationship between particle interaction forces and intrinsic particle characteristics, we can have a better idea of process variance introduced by raw material properties and thus control the raw material specs to enhance product and process consistency. Meanwhile, we are capable of predicting particle cohesiveness of different formulations, which provides additional information for excipient selection in formulation design. Moreover, it builds a theoretical foundation for engineered particle design to achieve desired particle cohesiveness.

Another contribution of this research is the proposed force models for the van der Waals, capillary and electrostatic forces. Rather than previous force models based on ideal spherical particle system, these models are suitable for estimation of cohesion interaction forces of actual pharmaceutical particles with rough surfaces. Tedious AFM force measurement can be replaced by model prediction to generate adhesion force data as input parameter in simulating bulk powder flow behavior.

Last but not least, this research pointed us to opportunities of process improvement. We can take advantage of the mechanistic knowledge of particle interaction to optimize particle properties or operating conditions for a more efficient process or better blend quality. In other words, this research supports FDA PAT initiative for a better process understanding or 'Quality-by-design' instead of 'Quality-by-inspection'.

10 Future work

Research is all about asking the right questions and figuring out ways to find the answer. During the course of this work more questions arose, bringing us challenges as well as opportunities. This research is focused on a fundamental level to answer the questions how micro-scale particles interact with each other and how to optimize particle interaction for macro-scale process improvement. In this chapter, future work is suggested to meet the new challenges and opportunities we came across in this research. The completion of the suggested work will give us more confidence in predicting, controlling and designing current blending process and allow us to extend this knowledge to innovative pharmaceutical manufacturing practice.

10.1 Suggested work in particle characterization

- Particles used in this research were confined to a narrow size range so that the size effect was minimized. In future studies, systems with wider particle size distribution should be investigated with respect to sensitivity of blend homogeneity on particle size.
- This research was focused more on excipient particles which are close to spherical in shape. However, many API crystals have very irregular particle shapes, which make particle interaction more complicated. An in-depth study on the shape factor in particle interaction and powder flow will generalize this research to broader pharmaceutical systems.
- Crystallinity or polymorphism of particle materials is another particle characteristic of interest in pharmaceutical development. Its effect on particle interaction and powder flow behavior should be addressed in the future research.
- Surface energy is closely related to particle adhesion interactions. The characterization of surface energy can be realized easily by inverse gas chromatography (IGC) technique. It is suggested to explore the correlation between surface energy and particle adhesion in the future work so that the particle adhesion may be more conveniently represented by the surface energy of the material.

- Although electrostatic charging is a common phenomenon in pharmaceutical powder handling process, there are little data regarding the work functions of varied excipient and API materials. Besides, the transient and unrepeatable feature of electrostatic charges adds more difficulty to the measurement of surface charges of pharmaceutical particles. It is proposed to develop an on-line bipolar charge meter to monitor the electrostatic charge level during the blending process in the future work. That will allow us to have a better understanding of charging effect on particle interaction and blend quality.

10.2 Suggested work in inter-particle force measurement

- The contribution of chemical bond to particle adhesions is ignored in this research. As a matter of fact, in some special cases, when the existence of hydrophilic/hydrophobic or other functional groups on interacting surface causes significant change in surface energy, chemical bond effects deserve further investigation.
- AFM is the primary technique applied in this research for the measurement of inter-particle adhesion force. However, the data acquisition is quite time consuming and the sample size is limited. It is suggested that alternative macro-scale force measurement approaches such as centrifugal detachment method be utilized to collect force data more rapidly. Besides, the data represents bulk powder adhesion interactions. This information associated with micro-scale interaction force allows us to evaluate more accurately the cohesiveness of different powder systems.

10.3 Suggested work in force modeling

- The capillary force model proposed in this research only discussed the simplest case of single asperity-to-asperity contact geometry. In real cases, the shape and volume of liquid meniscus between the interfaces may be distorted badly by the heterogeneous surface asperities. It is proposed to develop more advanced algorithms in the future work to simulate more complicated cases of surface contact geometry so as to have a more precise prediction of the capillary force. In addition, the thermodynamics of

liquid meniscus formation is suggested to be studied in favor of capturing time-dependence of capillary force.

- The electrostatic force model proposed in this research relies on the curve fitting result to get surface charge data. As mentioned earlier, direct and real-time measurement of surface charge is favored in the future to make the electrostatic force model more applicable and predictable. In addition, a further investigation of charging mechanism is recommended to get to know the time-dependence of charge generation, transition and dissipation.
- Since the inter-particle adhesion force is one of the crucial input parameters in the Discrete Element Method (DEM) simulation which has been proved to be a powerful tool to simulate powder flow and small-scale blending performance. Efforts should be taken to incorporation the inter-particle force models into the DEM package so that the tedious AFM force data collection can be skipped and the simulation can be run directly with a given set of particle characteristic parameters.

10.4 Suggested work in innovation of blending process

- All the blending experiments conducted in this research are binary systems consisting of one type of excipient and one type of API. It is desirable to extend the study to multi-component systems. That requires more data on particle characteristics of different excipients and APIs. One possibility is to build a library of physical/chemical properties of commonly used pharmaceutical ingredients. The data can be exported directly to the later process simulation.
- All the blending experiments conducted in this research are at lab scale. It is suggested to scale up blending process in the future work to see whether optimization of particle characteristics and environmental conditions ends up with better blend quality for larger scale blending operations.
- A recent trend in the pharmaceutical industry is to transfer batch operations to continuous manufacturing. The knowledge gained through this research regarding raw material properties can be applied to facilitate the development of innovative continuous blending process in the future work.

- As concluded from this research, appropriate electrostatic charging can improve blend homogeneity. With similar mechanism, a new blending technique called the electrodynamic blending was developed by Professor Malay Mazumder. It is suggested to continue the collaboration with his group in this field in the future and seek opportunity to transfer the research results to pharmaceutical industrial practices.

11 Appendix: an example on the application of the material characterization in industrial practice

In industrial practice, API manufacturing goes through a variety of processes to achieve desired particle properties. Among them milling is commonly used to reduce the API particle size to the desired range. During this course the large particle was broken down to smaller ones at high shear forces. In our study, the AFM and ESEM techniques were applied to identify the change in the raw material properties from different processing approaches.

Three powder samples were sent to our lab from our sponsor pharmaceutical company Bristol-Myers Squibb. These three samples are of the same drug substance with same chemical structure. However they were processed in three different ways, namely wet-mill, jet-mill and re-slurry jet-mill. In the experiments they were labeled as 'Sample A', 'Sample B' and 'Sample C', respectively.

Firstly, the surface morphologies of the three sample particles were observed under ESEM. As shown in the pictures below, the three samples have the similar particle size but distinctive particle size and surface morphology. Sample A, made by wet-mill, has more regular particle shape and smoother surface. In contrast, sample B and C have more angular particle shape and rougher surfaces with a lot of protuberances and bumps.

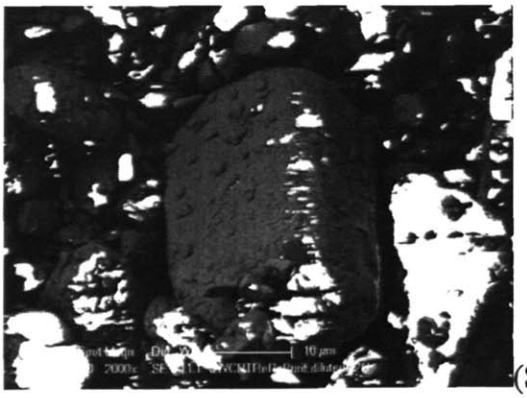
(Sample A)

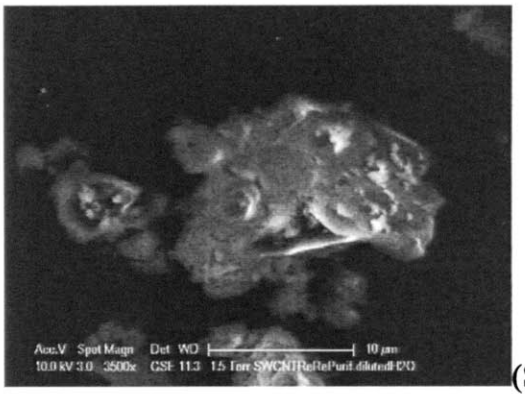
(Sample B)

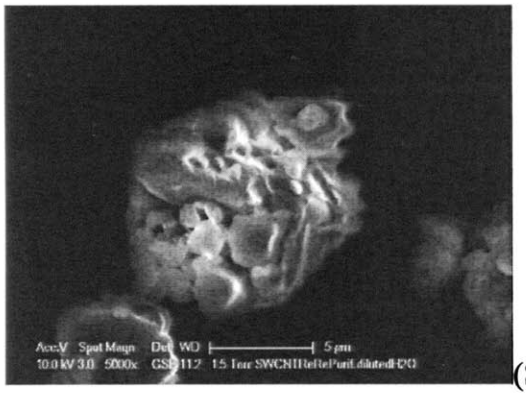
(Sample C)

Figure 11-1 ESEM pictures of three types of BMS sample particles

In the following AFM force measurements, the inter-particle cohesion forces of 15 pairs of particles were measured for each of the three samples. The procedures were the same as described in Chapter 2. The relative humidity was controlled at 49.5% for all the measurements. The cumulative frequency distribution of inter-particle cohesion force for all the three samples were illustrated in Figure 2. It was found that Sample A has a higher median cohesion force value and a wider cohesion force distribution than the other two jet-milled samples.

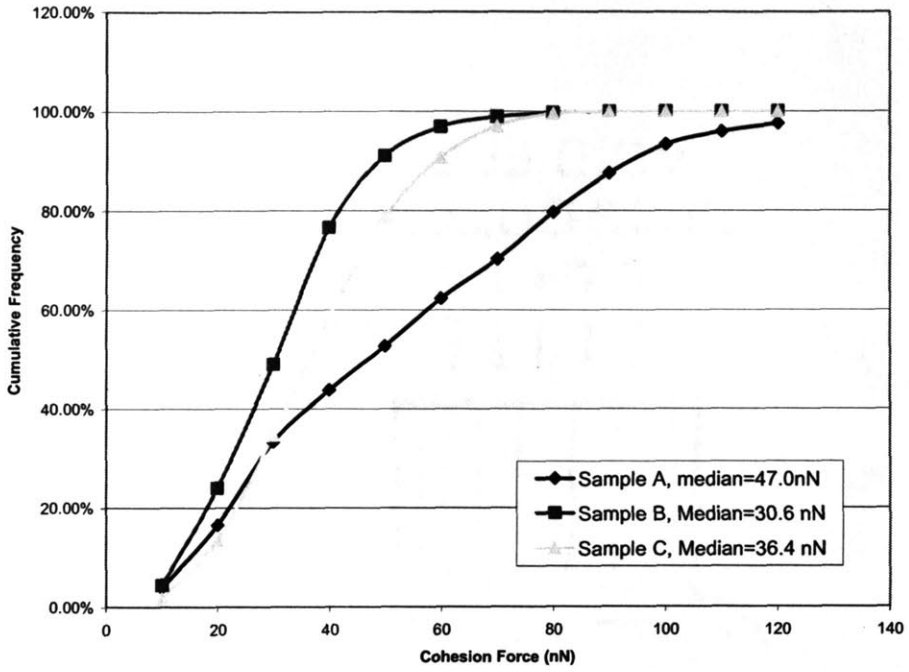

Figure 11-2 Cumulative frequency distribution of particle cohesion forces for BMS Sample A, B and C

The results show that different processing method may cause the particle morphological change, thus affecting the particle cohesion interaction and the surface energy of the material. These variations in raw material properties will later on introduce variance into the processes and lead to inconsistent product performance such as dissolution profile and bioavailability. Characterization of raw materials at a microscopic particle level is expected to provide us additional information in diagnosing and troubleshooting the problems in the manufacturing processes.